Tao Qian

218 Words

A Precise Measurement of Muon Lifetime at Brookhaven National Laboratory Muon Storage Ring

The lifetime of the positive and negative muon has been measured at Brookhaven National Laboratory in the same apparatus namely the g-2 storage ring. The experiments were performed in year 2000 and 2001 for positive and negative muons, respectively. Two major analyses have been conducted to measure the muon lifetime at rest: extracting the dilated lifetime from muon decay time spectrum, and obtaining the relativistic dilation factor from the cyclotron frequency and the muon momentum distribution.

A novel method called inverse ratio method was developed to fit the decay constant of the muon time spectrum. The obtained dilated lifetime is $\tau_{\mu^+} = 64\,408.4 \pm 2.3$ ns(stat) $\pm$ 5.2 ns(syst) and, $\tau_{\mu^-} = 64\,421.0 \pm 2.8$ ns(stat) $\pm$ 3.3 ns(syst). Three dominant systematic errors, namely muon loss, gain stability and pileup events, were included. The average momentum of the muons was obtained by analyzing the fast rotation structure of the muon bunch at time immediately after injection. A simulation model was developed to extract the momentum distribution.

By comparing τ_{μ^+} from this study with τ_0 measured at rest $(\tau_0 - \tau/\gamma)/\tau_0 = (12.4 \pm 9.3) \times 10^{-5}$, the Einstein time dilation factor agrees with experiment at 95% confidence range of (-6.2 to 31.0)$\times 10^{-5}$ for $\gamma = 29.314$ corresponding to a velocity of $\beta = 0.9994c$.

Assuming special relativity, the muon lifetime for positive muons and negative muons are $\tau_{\mu^+} = 2\,197.301 \pm 0.200$ ns (89 ppm), and $\tau_{\mu^-} = 2\,197.655 \pm 0.152$ ns (69 ppm). The comparison of positive and negative muon lifetime is a basic test of CPT invariance, $(\tau_0^- - \tau_0^+)/\tau_0^+ = (16 \pm 12) \times 10^{-5}$.

UNIVERSITY OF MINNESOTA

This is to certify that I have examined this bound copy of a doctoral thesis by

Tao Qian

and have found that it is complete and satisfactory in all respects and that any and all revisions required by the final examining committee have been made.

Professor Priscilla B. Cushman
(Faculty Adviser)

GRADUATE SCHOOL

A Precise Measurement of Muon Lifetime at Brookhaven National Laboratory Muon Storage Ring

A THESIS

SUBMITTED TO THE FACULTY OF THE GRADUATE SCHOOL

OF THE UNIVERSITY OF MINNESOTA

BY

Tao Qian

IN PARTIAL FULFILLMENT OF THE REQUIREMENTS

FOR THE DEGREE OF

DOCTOR OF PHILOSOPHY

August, 2006

A Precise Measurement of Muon Lifetime at Brookhaven National Laboratory Muon Storage Ring

by Tao Qian

Under the supervision of Professor Priscilla B. Cushman

ABSTRACT

The lifetime of the positive and negative muon has been measured at Brookhaven National Laboratory in the same apparatus namely the g-2 storage ring. The experiments were performed in year 2000 and 2001 for positive and negative muons, respectively. Two major analyses have been conducted to measure the muon lifetime at rest: extracting the dilated lifetime from muon decay time spectrum, and obtaining the relativistic dilation factor from the cyclotron frequency and the muon momentum distribution.

A novel method called inverse ratio method was developed to fit the decay constant of the muon time spectrum. The obtained dilated lifetime is $\tau_{\mu^+} = 64\,408.4 \pm 2.3$ ns(stat) $\pm$ 5.2 ns(syst) and, $\tau_{\mu^-} = 64\,421.0 \pm 2.8$ ns(stat) $\pm$ 3.3 ns(syst). Three dominant systematic errors, namely muon loss, gain stability and pileup events, were included. The average momentum of the muons was obtained by analyzing the fast rotation structure of the muon bunch at time immediately after injection. A simulation model was developed to extract the momentum distribution.

By comparing τ_{μ^+} from this study with τ_0 measured at rest $(\tau_0 - \tau/\gamma)/\tau_0 = (12.4 \pm 9.3) \times 10^{-5}$, the Einstein time dilation factor agrees with experiment at 95% confidence range of (-6.2 to 31.0)$\times 10^{-5}$ for $\gamma = 29.314$ corresponding to a velocity of $\beta = 0.9994c$.

Assuming special relativity, the muon lifetime for positive muons and negative muons are $\tau_{\mu^+} = 2\,197.301 \pm 0.200$ ns (89 ppm), and $\tau_{\mu^-} = 2\,197.655 \pm 0.152$ ns (69 ppm). The comparison of positive and negative muon lifetime is a basic test of CPT invariance, $(\tau_0^- - \tau_0^+)/\tau_0^+ = (16 \pm 12) \times 10^{-5}$.

Acknowledgements

First of all, I wish to thank my advisor, Professor Priscilla Cushman, for her support over the years and her insightful comments and suggestions during my research and thesis writing process.

In addition, I am quite grateful for the instruction and advice I have received from several exceptional U of M professors including Ben Bayman, William Zimmermann, Mikhail Voloshin, Ron Poling, Yuichi Kubota, and Jon Urheim.

I want to thank the many individuals who made my research work possible in the first place, including the members of the E821 Collaboration and BNL personnel who conceived, constructed, and conducted the experiment. Collaborators whom I wish to thank in particular for their helpful discussions are Jim Miller, Bill Morse, Dave Hertzog, Lee Roberts, Rob Carey, Yannis Semertzidis, Mario Deile, Vanya Logashenko, Cenap Ozben, Jon Paley, Ofer Rind, Ernst Sichtermann and especially Gerco Onderwater, Fred Gray and Chris Polly for their invaluable assistance. And I also would like to thank the computer help group at University of Illinois at Urbana-Champaign for their generous help.

The entire Minnesota-based group, including Ivan Kronkvist, Long Duong, Steve Giron, Ron McNabb, Ben Bousquet, and Petr Shagin, has been a pleasure to work with as well. I also want to thank Angela Reisetter.

Most importantly, I would like to thank my father Qian Pingnan, my mother Zhang Panzhen, and my sister Qian Lin, for their unconditional love and support they have provided. I thank my dear wife, Yang Fang, for her love and encouragement. Finally, I would

like to thank my lovely daughter, YaLan. Her sweet smiles give me the strength to finish the work.

Table of Contents

List of Tables

List of Figures

Chapter 1

Introduction of Muon Lifetime Measurement

1.1 Muon in the Standard Model

Our understanding of modern elementary particle physics is based on the Standard Model, which describes the fundamental interactions, the strong, the electromagnetic and weak interactions among the particles and fields. These interactions are described as a $SU(3)_C \times SU(2)_L \times U(1)_Y$ gauge theory. Among the fundamental particles, *muon* (μ) particle is one of the second generation leptons. The muon mass is $m_\mu = 105.6583692(94)$ MeV, which is derived from the ratio of the muon mass to the electron mass measured in a muonium ($\mu^+ e^-$ atom) with QED corrections [1].

The Standard Model has confronted various and extensive experimental tests since the formulation of the Model in 1960s. It has performed extremely well in explaining all measurements so far. The muon lepton played an important role in the development of the Standard Model since it was discovered in 1937 by Neddermeyer and Anderson in the cosmic rays [2]. The muon undergoes the pure weak decay processes, $\mu^+ \to e^+ + \nu_e + \bar{\nu}_\mu$, or $\mu^- \to e^- + \bar{\nu}_e + \nu_\mu$. These decay processes are described by a charged weak-current

interaction mediated by the $W^{\pm}$ gauge boson. The normal muon decay remains the only purely leptonic process of the weak interaction accessible to precise measurements with high statistics. The studies are free from the complications of the strong interaction and hadronic structure. For this reason, precise studies of normal muon decay provide information unambiguously interpreted.

As a renormalization theory, the Standard Model requires experimental inputs. The Fermi coupling constant G_F, which is determined directly from the experimental muon lifetime, is one of the three precisely measured inputs of the SM, along with the fine structure constant α and the Z boson mass m_Z. The current values are [3],

$$\begin{aligned} \alpha &= 1/(137.035\ 999\ 11\ \pm\ 0.000\ 000\ 46) \\ G_F &= 1.166\ 37 \pm 0.000\ 01\ \times\ 10^{-5}\ \mathrm{GeV}^{-2} \\ M_Z &= 91.187\ 6 \pm 0.002\ 1\ \mathrm{GeV} \end{aligned}$$

Before 1998, the mass of Z boson was known to be 91.187 ± 0.007 GeV with 77 ppm uncertainty. Now, it has been determined to 23 ppm relative uncertainty after an improvement by LEP and SLD Electroweak Working Group in 1999. (The Z boson mass keeps the similar value in 2005 [4].) Thus, the uncertainties of G_F and m_Z become comparable before a complete two-loop Quantum Electrodynamic correction to the muon lifetime was calculated in 1999 by Ritbergen [5]. With the two-loop QED correction, the theoretical errors in the G_F calculation from the muon lifetime have become negligible, leaving all the uncertainty (9 ppm) in the measurement of the muon lifetime.

In the past, studies of the muon decay have greatly contributed to developing the electroweak interaction in the Standard Model. Muon decay is now playing a role in probing for possible deviations from the Standard Model. Comparing G_F from the muon lifetime with electroweak parameters determined from other measurements, such as tau leptonic decays, M_W, or other observables at the M_Z pole could lead to the new physics[6].

1.2 Muon Lifetime Measurements—History and Difficulties

The muon was discovered in 1937 in cosmic rays, just after Yukawa postulated the existence of the pion (π) meson. The muon mass, which is about 200 times the mass of electron, is similar to that of the pion. Then, it was found that muon decays through weak interaction. Since then, measuring the muon decay and its products has played an important role in the study of electroweak interaction.

This research was significantly improved when muons became artificially produced at the accelerators. The high-intensity muon beams are available at the three meson factories, the Paul Scherrer Institute (PSI) in Switzerland, TRIUMF in Canada, and the Rutherford Appleton Laboratory (RAL) in England. It is worth pointing out that all muon lifetime experiments listed on Particle Data Book [3] were performed more than two decades ago. The world average value for the lifetime is $\tau_0 = 2.197\ 03 \pm 0.000\ 04\ \mu$s. Fig. 1.1 shows the previous lifetime measurements for both positive and negative muon particles. Their values and the reference documents are listed in Table 1.1, and their experiments are discussed in next sections.

VALUE($1.0^{-6}s$)			DOCUMENT ID	YEAR	TECN	CHARGE
2.197078	$\pm$	0.000073	BARDIN	1984	CNTR	+
2.197025	$\pm$	0.000155	BARDIN	1984	CNTR	-
2.19695	$\pm$	0.00006	GIOVANETTI	1984	CNTR	+
2.19711	$\pm$	0.00008	BALANDIN	1974	CNTR	+
2.1973	$\pm$	0.0003	DUCLOS	1973	CNTR	+

Table 1.1: Historical record of muon lifetime measurement from Particle Data Group, 2004 [3].

1.2.1 Muon Lifetime Measurement of Positive Charged Muon

The last positive muon lifetime measurements for the stopped muons were performed in late 1970s and early 1980s [7, 8, 9]. One research group worked at the Tri-University Meson

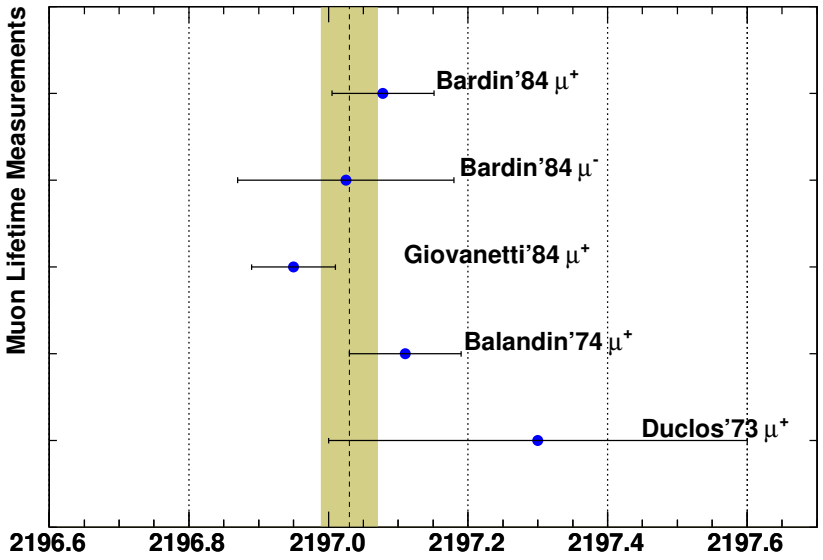

Figure 1.1: Muon lifetime measurements in history. The shadow area marks the one sigma error band around the current world average with value $\tau_0 = 2197.03 \pm 0.04$ ns.

Facility (TRIUMF) in Vacouver, and another group worked at the Saclay linear accelerator, France. The techniques used in the two experiments were quite similar. A pulsed π^+ beam was stopped in a target and the decay e^+ were detected. In reference [8], a 140 MeV/c pulsed π^+ beam was stopped in the sulfur target, which is known to depolarize the muons faster than other materials. The stopped pions provided an unpolarized muon source in the target. About 5% of beam was composed of the polarized decay muons from the pions during their flight. The decay positrons were detected by six plastic scintillator telescopes which surrounded the target along the beam axis with a 75% solid angle coverage. There were a total of 1.254 billions events (positrons) taken in several years. Among them, about 16% events were taken in liquid-hydrogen target, which will be discussed in the muon capture section 1.2.2. The measured positron was described by the exponential distribution

$$R(t) = R_0[exp(-\lambda\ t) + A\ r\ exp(-2\lambda\ t) + B] \tag{1.1}$$

where, the rate dependent term r was included, and a physical background B came mainly from cosmic rays. $B = B_0 + B_1 exp(-t/T)$, where $T = 160$ μs. The final correction to the rate effect was obtained by extrapolating from the high-rate and low-rate to $r = 0$. The final muon lifetime from the experiment was given by $\tau_{\mu^+} = 2\ 197.078 \pm 0.073$ ns as listed in Table 1.1. The final error included both the statistical and systematical error. Polarization effects contributed an upper limit of 0.06 ns to the systematic error.

The other group at TRIUMF published their positive muon lifetime experiment result in the same year (1984). A positive pion beam with energy between 150 MeV/c-170 MeV/c traversed ~10 m long channel and entered a water tank [9]. The beam contained mainly pions, with small amount of muons and electrons. The beam was in bunches of 2-5 ns time width. The particles were identified by their time-of-flight in the long channel. Two scintillation counters in front of the water tank detected the entering beam particles. While about 5% pions were removed from the population through nuclear reactions, the remaining 95% incoming π^+ were stopped in the water and decayed into μ^+. After traveling a very short distance in the water, the daughter μ^+ stopped and decayed into e^+. These decay e^+ were detected through their Čerenkov radiation in the stainless-steel cylinder water tank. Two 12.7-cm-diameter photomultiplier tubes, which were set on the two sides of the cylinder, collected the light from the radiation. The total signal from the two PMTs was used to distinguish e^+ from π^+ and μ^+, which had much smaller signals. The time information of the decay event was recorded between the start time from the entering scintillation counters and the stop time from the Čerenkov signals in a time interval 20 μs. The time histogram with the medium energy range was fitted by the decay function form $R(t) = N\ e^{-t/\tau} + B$, where B was the background term. Since the fit start time was more than 11 times pion lifetimes, the description of the initial growth of the muon population was not necessary in the fitting function. The final result was $\tau_{\mu^+} = 2196.\ 95 \pm 0.06$ ns, as listed in the table.

1.2.2 Negative Muon Capture Rate

The lifetime of the negative charged muons μ^- can not be measured precisely by using the same technique as that for μ^+ described in the previous section. Instead, an important reaction happens when the negative muons are stopped by the target. The stopped negative muons are captured by the protons in the nuclei. The muon capture rate by the proton provides excellent information to probe the weak axial correction to the nucleon and to test chiral symmetry breaking in QCD [10].

The muon capture rate has been measured by several groups. Unlike the μ^+, in which weak decay is the dominant process accounting for its disappearance in the target, the μ^- also disappears from the stopping target (for example, pure liquid hydrogen) via the nuclear capture $\mu^- + \mathrm{p} \rightarrow \mathrm{n} + \nu_\mu$. The emitted neutron has a typical energy of 5.2 MeV. The nuclear capture process takes place only after the muon has formed one of the possible bound systems with the protons in the target. Generally, the capture rate is 10^{-3} times the rate of decay process. It also depends strongly on the total spin state of the muon-proton system. Typically, after a negative muon has stopped in a liquid-hydrogen target, an atomic system $(\mu\mathrm{p})_{1s}$ is formed in less than 1 ns. The muonic system (μp atom) has a high rate to transfer to deuteron or heavier nuclei in the target. Since in the muon capture process, the other decay product, muon neutrino ν_μ, is more difficult to detect, most of the experiments to measure the capture rate have had to rely on the detection of the 5.2 MeV neutrons [11, 12, 13]. The absolute efficiency of the neutron detectors in the experiment was based on an elaborate Monte Carlo simulation, creating a significant systematic error.

Because of these difficulties in measuring the muon capture rate through the neutron detection, an accurate lifetime for the negative muon is harder to measure than the lifetime of positive muon in the stopping experiments. Instead, researchers [14] have compared the disappearance rate $\lambda_{\mu^-} = 1/\tau_{\mu^-}$ of the negative muons stopped in the isotopically pure liquid hydrogen (protium) with the disappearance rate $\lambda_{\mu^+} = 1/\tau_{\mu^+}$ of positive muons in the same target and obtained the results of negative muon capture rate λ_c. Both τ_{μ^-} and

τ_{μ^+} were measured by studying the time spectrum of the detected decay electrons/positrons.

The various atomic and molecular processes which occur when a negative muon is stopped in liquid hydrogen are known. Within 500 ns after the $(\mu p)_{1s}$ system is formed, the system gets bound in a pμp molecular ion. When the measurement starts, the muons are almost entirely within pμp molecular ions. Fig. 1.2 shows the simplified experiment setup. Protium gas was circulated and purified during the experiment to reduce the contamination of higher Z nuclei. A total amount of 1.3 billion μ^- decay events in purified protium were recorded, and in the same running period, 0.38 billion μ^+ decay events were obtained at low event rate (r=0.1). Some other 0.1 billion events for both μ^- and μ^+ were recorded at high rate (r=0.5). To reduce the muon polarization effects, μ^+ were stopped in a sulfur target as described in Sec. 1.2.1. Some of the μ^+ data were taken with the protium target surrounded by a magnetic shield. It was shown that the polarization effects were negligible.

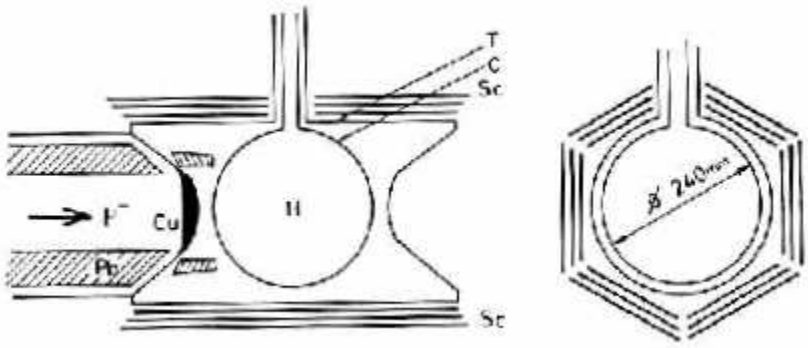

Figure 1.2: Simplified schematic view of the muon capture experiment setup. Pb = lead collimator; Cu = copper degrader; C = copper vessel; T = steel chamber; SC = plastic scintillator telescopes. (Reproduced from reference [14])

Both μ^+ and μ^- decay spectra were fitted with the Eq. 1.1. The μ^+ lifetime value from this measurement gave $\tau_{\mu^+} = 2197.182 \pm 0.121$ ns. After combining with other data to form the world average τ_{μ^+} in 1978, $\tau_{\mu^+} = 2197.148 \pm 0.066$ ns. The fitted μ^- decay constant was

$\tau_{\mu^-} = 2194.903 \pm 0.066$ ns, which was just a mathematical value. The muon capture rate in liquid hydrogen λ_c was calculated by assuming CP invariance between μ^+ and μ^-. Since the decaying negative muons were bound, a small correction had been taken into account for the relativistic effect. Finally, the measured μ^- capture rate was $\lambda_c = 460 \pm 20\ s^{-1}$. The current negative muon lifetime $\tau_{\mu^-} = 2197.025 \pm 0.155$ ns was calculated [8] after taking into account the nuclear capture rate and the ortho-to-para transition rate.

1.2.3 Lifetime Measurements of the Relativistic Muons

In the previous CERN (g-2) experiments [15, 16, 17], the lifetime of both positive and negative relativistic muons were measured in a storage ring. The measured dilated lifetime for the μ^+ was $\tau_{\mu^+} = 64\ 419 \pm 58$ ns, and for the μ^-, it was $\tau_{\mu^-} = 64\ 368 \pm 29$ ns while the muon momentum was about 3.094 GeV/c. The average special relativistic γ-parameter was measured to be $\bar{\gamma} = 29.327 \pm 0.004$. The quoted error corresponded to an uncertainty of ± 1 mm in the mean radius of the distribution of circulating muons. After assuming special relativity, the lifetime for the muon at rest τ_0 is given by $\tau_0 = \tau/\gamma$. The reported lifetimes τ_0 in CERN experiments were $\tau_0^+ = 2196.6 \pm 0.2$ ns and $\tau_0^- = 2194.8 \pm 0.1$ ns [18]. The similar muon lifetime measurements were made at the Brookhaven National Laboratory muon (g-2) experiment with more decay electron/positron data collected. The data analysis procedure and lifetime results are reported in this thesis.

1.3 The Muon (g-2) Experiment at BNL

The muon (g-2) Experiment E821 at Brookhaven National Laboratory (BNL) was designed to measure the muon anomalous magnetic moment, $a_\mu = (g_\mu - 2)/2$, to an accuracy of 0.35 ppm, where g_μ is the muon gyro-magnetic ratio. Since the electroweak interaction correction to the anomalous magnetic moment is proportional to the lepton mass square term (m_l^2), the muon magnetic moment value is more sensitive than that of electron to the effects beyond the Standard Model. This experiment started its first test run in 1997 and

the last run ended in 2001 [19, 20, 21, 22, 23].

The measurement of the anomalous spin precession frequency ω_a in the 2000 run data gave $a_{\mu^+} = 11\ 659\ 204(7)(5) \times 10^{-10}$ or 0.7 ppm, and $a_{\mu^-} = 11\ 659\ 214(8)(3) \times 10^{-10}$ or 0.7 ppm for 2001 run. The world average value of a_μ, which is dominated by the 2000 and 2001 (g-2) results, is $a_\mu(exp) = 11\ 659\ 208(6) \times 10^{-10}$ or (0.5 ppm). The total uncertainty consists of 5×10^{-10} or (0.4 ppm) statistical uncertainty and 4×10^{-10} (0.3 ppm) systematic uncertainty.

In the same (g-2) experiment, the electric dipole moment (EDM) of the muon was also measured. The EDM is related to its intrinsic spin in the same manner as the magnetic moment, $\vec{d}_\mu = \eta\ (\frac{e}{2mc})\ \vec{s}$, where η serves as the constant of proportionality. The existence of a nonzero muon EDM would tilt the plane of the spin precession, affecting the measurement of the anomalous spin precession frequency. The resultant effect on a_μ is proportional to the size of the EDM,

$$\Delta a_\mu(\text{EDM}) = \frac{m_\mu^2}{\alpha^2} |d_\mu|^2. \tag{1.2}$$

In the 2000 data, the EDM analysis showed that a vertical oscillation amplitude of $-1.3 \pm 5.9(stat) \pm 10.4(syst)$ mrad consistent with no EDM signal. It gave an EDM measurement of $(-0.1 \pm 1.4) \times 10^{-19}$ e-cm for positive muons.

The muon lifetime measurement described in this thesis is the last analysis in the BNL muon (g-2) experiment, but nevertheless it is an important analysis. The lifetime measurement in the BNL (g-2) experiment is really two tests in one. A precision value of τ_{μ^+} provides a check of the Einstein time dilation factor in the theory of special relativity, and a comparison of τ_{μ^+} and τ_{μ^-} is a further test of CPT. The determination of the lifetime is, in principle, a straightforward fit to the (g-2) oscillation envelope. In the previous CERN (g-2) experiment, the statistical error dominated in the result, but the systematic errors due to time-dependent muon losses and detector gain changes were also important. The precision achieved, both for the lifetime in flight and for the lifetime at rest (assuming special relativity), was 0.5×10^{-3} for τ_{μ^-} and 10^{-3} for μ^+. The ratio $(\tau_{\mu^+} - \tau_{\mu^-})/\tau_{\mu^+} = (0.8 \pm 1.0) \times 10^{-3}$

was obtained in agreement with the result expected on the basis of CPT invariance, but the measured value $\tau_{\mu^+} = 2.1948(10)$ μs was more than two standard deviations below the presently accepted value of $\tau_{\mu^+} = 2.19703(4)$ μs.

In the BNL (g-2) experiment, we achieved a much higher statistical accuracy and the comparison of τ_{μ^+} and τ_{μ^-} reached an overall precision of 10^{-4}, which is about a factor of 10 better than any other direct comparison of the lifetimes of free μ^+ and μ^-. A precision of 10^{-4} in determining τ_{μ^+} is achieved from the data of the BNL muon (g-2) experiment together with the time dilation factor γ.

1.4 A Test of Special Relativity

The core of special relativity is that local space-time is Lorentz invariant, which is one of the most fundamental symmetries of all modern descriptions of nature. The quantity $s = x^2 + y^2 + z^2 - (ct)^2$ is invariant in different reference frames. The physical form follows the Lorentz's transformation in special relativity, giving the time dilation effect naturally. The time interval τ observed in the laboratory frame is $\tau = \int_{t_1}^{t_2} \mathrm{d}t$. If the moving frame keeps a constant velocity v, and τ_0 is the proper time (the time interval observed in the rest frame of the system or particle), then the time interval τ is greater than τ_0 by a factor of γ, i.e. $\tau = \gamma\tau_0$. This effect is called time dilation. The lifetime measurement in the (g-2) experiment is a basic test of the time dilation by comparing the muon lifetime at flight and that of at rest.

Since the theory of special relativity was invented in 1905 by Einstein, it has been subjected to tests in various particle velocity ranges [24, 25]. The latest experiment [26] used laser spectroscopy on fast ions at the heavy-ion storage-ring to test time dilation. The Doppler-shifted frequencies of a two-level transition in $^7Li^+$ ions at $v = 0.064c$ have been measured in the forward and backward direction to an accuracy of $\delta\nu/\nu = 1 \times 10^{-9}$. The result confirms the relativistic Doppler formula and sets a new limit of 2.2×10^{-7} for deviations from the time dilation factor. The previous CERN (g-2) experiment [18] showed

that $(\tau_0 - \tau/\gamma)/\tau_0 = 10^{-3}$ in the storage ring with $\beta = 0.9994$.

In the BNL muon (g-2) experiment, the test of special relativity is best done with μ^+ rather than μ^-, because the positive muon lifetime at rest is much better known. A precision of 10^{-4} in determining τ_{μ^+} is achieved from the data of the BNL muon (g-2) experiment together with the time dilation factor γ. Even though the g-2 ring is not an inertial reference frame, the dilation relation still holds [24].

Other postulates of the special relativity have also been tested. D. Newman [24] compared the results of the gyro-magnetic ratio g of an electron for two different velocity regions, namely 5×10^{-5}, 1 and 0.5. They concluded from the measured agreement of g for free electrons at these different velocities that a major kinematic prediction of special relativity, the Thomas precession, was verified to 5×10^{-9}. The Thomas precession is a result of the kinematics of special relativity as applied to rotated axes. It affects the spin precession frequency, but not γ. All the tests made so far have not falsified special relativity.

Chapter 2

Muon Decay and Fermi Coupling Constant

The muon decay is purely leptonic process and therefore very clean both experimentally and theoretically. The decay process can be described by the local four-fermion interaction at the lowest level approximation. The first loop and second loop QED corrections to the muon decay rate are calculated in the Fermi theory. After the second loop correction is done, the uncertainty on the Fermi coupling constant is limited only by the experimental measurement of the muon lifetime, but not the theoretical calculation any more.

2.1 Muon Decay

The analysis of the muon decay has played a very important role in establishing the Standard Model. The dominant decay modes for the muons are the Michel decay, $\mu^- \to e^- + \bar{\nu}_e + \nu_\mu$ and $\mu^+ \to e^+ + \nu_e + \bar{\nu}_\mu$, with the decay branching ratio $\approx 100\%$. These normal muon decays involve pure lepton fields only, so that the physics is not obscured by the phenomenology of strong interaction fields. They can be described by the local and lepton-number conserving four-fermion point interaction Hamiltonian. The general interaction Lagrangian density is

written as

$$\mathcal{L}_{lepton} = -2\sqrt{2}\ G_F\ g_{\mu\nu} j^{\mu}\ j^{\nu\dagger} \tag{2.1}$$

where G_F is the Fermi coupling constant, which must be expressed in terms of physical observables or well prescribed renormalized parameters. The general weak current j^{μ} including all three generation of leptons is

$$j^{\mu} = \bar{\phi}_e \gamma^{\mu} \frac{1}{2}(1-\gamma^5)\nu_e + \bar{\phi}_{\mu} \gamma^{\mu} \frac{1}{2}(1-\gamma^5)\nu_{\mu} + \bar{\phi}_{\tau} \gamma^{\mu} \frac{1}{2}(1-\gamma^5)\nu_{\tau} \tag{2.2}$$

For muon decay, the effective interaction Lagrangian density is given by

$$\mathcal{L}_{Fermi} = -\frac{G_F}{\sqrt{2}}\Big[\bar{\nu}_{\mu}\gamma^{\mu}(1-\gamma_5)\mu \bar{e}\gamma_{\mu}(1-\gamma_5)\nu_e + \bar{\nu}_e\gamma^{\mu}(1-\gamma_5)e\bar{\mu}\gamma_{\mu}(1-\gamma_5)\nu_{\mu}\Big] \tag{2.3}$$

where e and ν_e are the left-handed spinor fields of electron and electron neutrino; μ and ν_{μ} are the left-handed spinor fields of muon and muon neutrino, respectively. In the low-energy limit, the intermediate bosons which mediate the current interactions are immaterial. We can refer to an effective local interaction between currents. For muon decay, the non-local graph reduces to a local four-Fermion interaction graph as shown in Fig. 2.1.

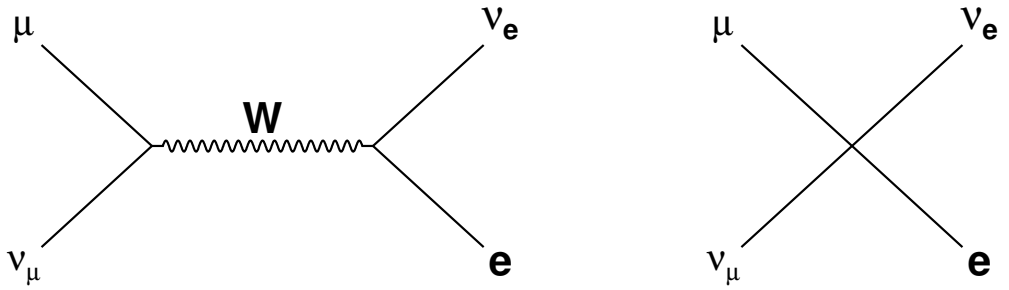

(a) (b)

Figure 2.1: Local four fermion interaction of muon decay. The W-boson in (a) is immaterial in the low energy limit. (b) is a local four-Fermion interaction graph.

The interaction Lagrangian density Eq. 2.3 implies a strong correlation between the angle θ made by the direction of the electron with the direction of the muon spin, and

the energy E_e of the electron. In the muon rest frame, to the lowest order of perturbation theory, and neglecting terms in $(m_e/m_\mu)^2$, the differential decay rate in an angular interval $\mathrm{d}\theta$ and energy interval $\mathrm{d}E_e$ is [27, 28],

$$\frac{\mathrm{d}\Gamma(\theta, E_e)}{\mathrm{d}\theta \mathrm{d}E_e} = \frac{G_F^2 m_\mu}{6\pi^3}\Big[\Big(\frac{3}{2}E_{max} - E_e\Big) + \cos\theta\Big(\frac{1}{2}E_{max} - E_e\Big)\Big]E_e^2 \sin\theta \tag{2.4}$$

where $E_{max} = (m_\mu^2 + m_e^2)/2m_\mu$ is the maximum electron energy. In the limit of zero electron mass, $E_{max} = m_\mu/2$, integrating over θ and E_e gives the total decay rate for this process

$$\tau_\mu^{-1} = \Gamma_0 = \frac{G_F^2 m_\mu^5}{192\pi^3} \tag{2.5}$$

This well-know formula provides an accuracy at the level of 10^{-3} in calculating the Fermi constant G_F.

2.1.1 First Loop QED Corrections

Better precision in the muon decay rate is achieved after including the correction to higher order interactions, the mass of final state particles, and the finite mass of W-boson. The first loop *QED* contributions to the muon lifetime were calculated in late 1950s by Berman [29] and Kinoshita and Sirlin [30]. The Feynman diagrams for the first loop QED correction are shown in Fig. 2.2. It is known that the Fermi theory in the presence of QED is finite to the leading order in G_F and to all orders in the electromagnetic coupling constant α. This remarkable fact means that G_F can be defined in a physically unambiguous manner, and at least up to the point where finite W propagator effects begin to appear. The muon decay rate after the first loop correction is given in Eq. 2.6,

$$\begin{aligned}\tau_\mu^{-1} &= \frac{G_F^2 m_\mu^5}{192\pi^3} F\Big(\frac{m_e^2}{m_\mu^2}\Big) \times \Big(1 + \frac{3}{5}\frac{m_\mu^2}{M_W^2}\Big) \times \Big(1 + \frac{\alpha(m_\mu)}{2\pi}(\frac{25}{4} - \pi^2)\Big) \\ &= \Gamma_0 \times (1 - 187.12 \times 10^{-6}) \times (1 + 1.05 \times 10^{-6}) \times \Big(1 - 4203.85 \times 10^{-6}\Big)\end{aligned} \tag{2.6}$$

where the virtual photons correction $\alpha(m_\mu)$ (*QED* radiative) term is by far the largest correction with relative magnitude of -4203.85×10^{-6}, the small electron mass correction term (m_e^2/m_μ^2) is the second largest with relative magnitude of -187.12×10^{-6}, and the finite W-boson mass correction (m_μ^2/M_W^2) is the smallest with magnitude 1.05×10^{-6}.

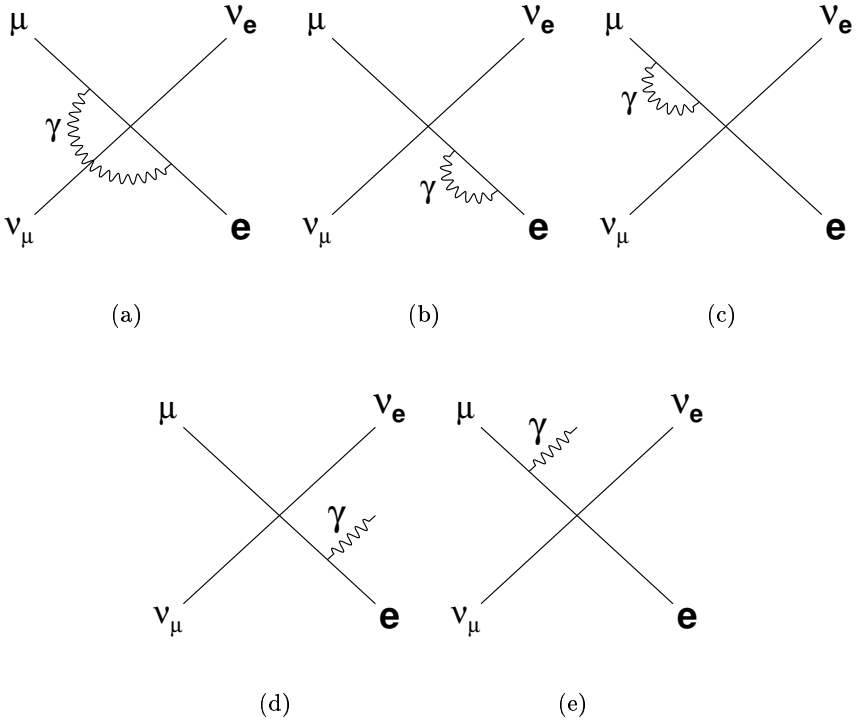

Figure 2.2: Feynman diagrams of the first loop QED corrections to the muon decay. (a, b, c) are virtual processes, (d, e) are inner bremsstrahlung processes.

2.1.2 Two Loop QED Corrections

Compared to the first loop correction which is at the level of 10^{-3}, the second loop QED radiative corrections are small at the level of 10^{-5}. This correction is at the current experimental uncertainty, and its accurate calculation is necessary to extract the G_F value. The two-loop QED corrections in the muon lifetime calculations include photonic corrections and electron loop corrections.[1] The processes, such as $\mu^- \to e^- + \bar{\nu}_e + \nu_\mu$, $\mu^- \to e^- + \bar{\nu}_e + \nu_\mu + \gamma$, $\mu^- \to e^- + \bar{\nu}_e + \nu_\mu + \gamma + \gamma$, and $\mu^- \to e^- + \bar{\nu}_e + \nu_\mu + e^+ + e^-$, contribute to the 2-loop QED corrections with up to two virtual photons. Each of the individual diagrams is infrared divergent and, in some cases, requires integration over a 5-body phase space. The problem

[1] This calculation follows Ritbergen and Stuart [5].

of canceling these infrared singularities can be avoided entirely if the QED corrections are obtained as the imaginary part of 4-loop propagator-type Feynman diagrams by means of the optical theorem [31]. Some of these 4-loop propagator-type diagrams are shown in Fig. 2.3 whose cuts give contributions to the photonic corrections in the above processes. The cuts generating imaginary parts produce all of the Feynman diagrams contributing to muon decay. The result for just the photonic diagrams is

$$\begin{aligned}\Delta\Gamma^{(2)}_{\gamma\gamma} &= \Gamma_0\Big(\frac{\alpha_r}{\pi}\Big)^2\Big(\frac{11047}{2597}-\frac{1030}{27}\zeta(2)-\frac{223}{36}\zeta(3)+\frac{67}{8}\zeta(4)+53\zeta(2)\ln(2)\Big)\\ &= \Gamma_0\Big(\frac{\alpha_r}{\pi}\Big)^2\times 3.55877 \qquad (2.7)\end{aligned}$$

where $\alpha_r = 1/135.90$, $\zeta(s)$ is Riemann Zeta function. $\zeta(2) = \pi^2/6$, $\zeta(3) = 1.2020569$ and $\zeta(4) = \pi^4/90$. The scale of the photonic correction is about 19×10^{-6} (19 ppm) to the tree level width.

The electron loop corrections to the muon lifetime calculation is at the similar magnitude as that of the photonic correction. The contribution of electron loops to the muon lifetime differs from those of other fermions in that they must be combined with diagrams with an additional e^+e^- pair in the final state in order to produce an infrared finite result. The same procedure as in photonic correction by calculating the imaginary part of 4-loop propagator-type Feynman diagrams is applied in the electron calculation. The examples of electron loop diagrams are shown in Fig. 2.4. The overall correction from the electron loop is

$$\begin{aligned}\Delta\Gamma^{(2)}_{elec} &= -\Gamma_0\Big(\frac{\alpha_r}{\pi}\Big)^2\Big(\frac{1009}{228}-\frac{77}{36}\zeta(2)-\frac{8}{3}\zeta(3)\Big)\\ &= \Gamma_0\Big(\frac{\alpha_r}{\pi}\Big)^2\times 3.22034 \qquad (2.8)\end{aligned}$$

This correction is about 17×10^{-6} (17 ppm) to the tree level width.

The same procedure and method in the calculation of the contribution of the electron loops were applied to the virtual muon loops and tau loops. The corrections to the muon lifetime coming from virtual muon and tau loops are very small [32] compared to the first loop and second loop photonic and electron correction. The muon loop correction is at the

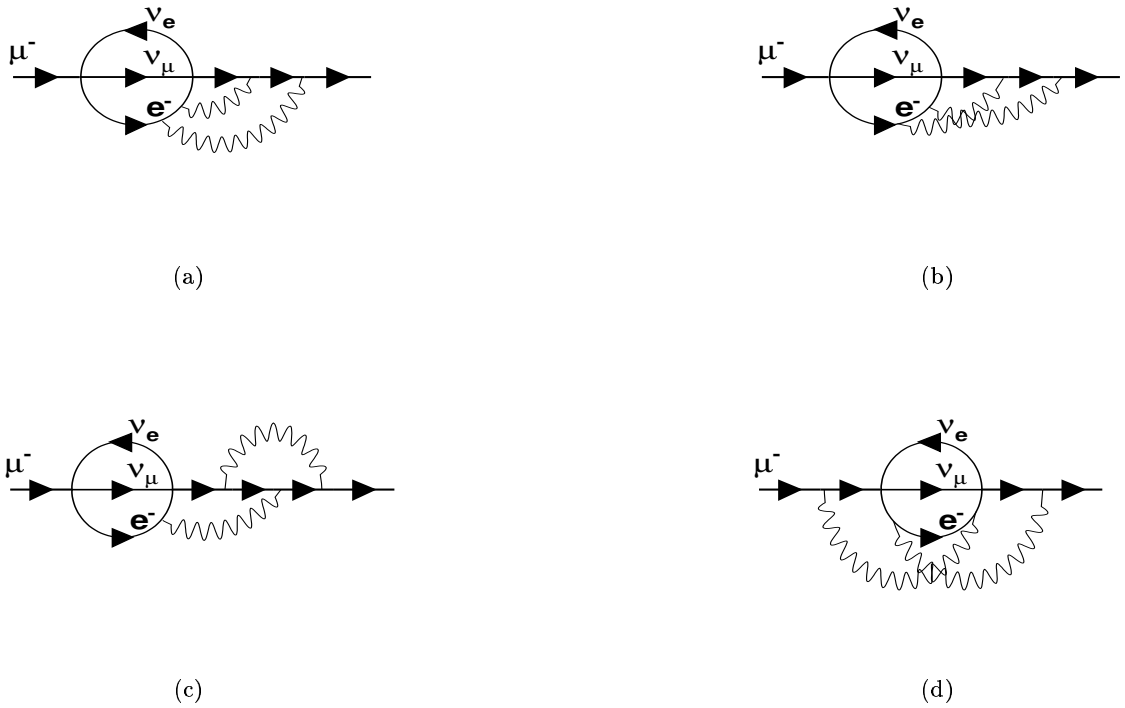

Figure 2.3: Examples of Feynman diagrams whose cuts give contributions to the photonic corrections in the muon decay. The heavy lines represent muons which are the only particles taken to have nonzero mass. The 4-fermion vertex used is the vector part of the usual one from the Fermi theory. (Reproduced from Ref. [5])

level of 0.2 ppm and tau loop correction is at 0.003 ppm to the tree level width.

$$\Delta\Gamma_{muon} = -\Gamma_0\Big(\frac{\alpha}{\pi}\Big)^2 \times 0.0364 = -0.197 \times 10^{-6}\ \Gamma_0 \tag{2.9}$$

$$\Delta\Gamma_{tau} = -\Gamma_0\Big(\frac{\alpha}{\pi}\Big)^2 \times 0.00058 = -0.003 \times 10^{-6}\ \Gamma_0 \tag{2.10}$$

The hadronic corrections to the muon lifetime are at the same order as the muon loops. They were also calculated by T. Ritbergen and R. Stuart [32] in the Fermi theory in the presence of QED using dispersion relations. The contribution is also at 0.2 ppm level.

$$\Delta\Gamma_{had} = -\Gamma_0\Big(\frac{\alpha}{\pi}\Big)^2 \times 0.042 = -0.227 \times 10^{-6}\ \Gamma_0 \tag{2.11}$$

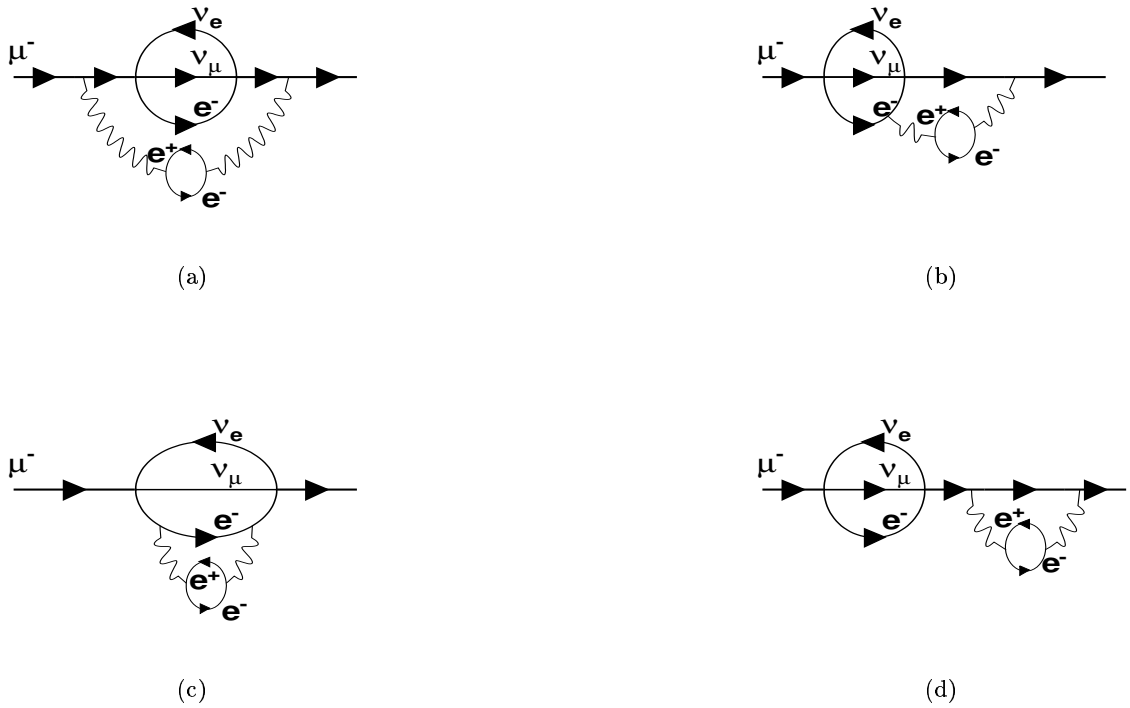

Figure 2.4: Examples of Feynman diagrams whose cuts give contributions to the electron loop corrections in the muon decay calculation. (Reproduced from Ref.[5])

The hadronic corrections and virtual muon loops are 100 times smaller than the second loop QED corrections. The tau loop contribution is much more smaller and can be ignored at this moment. Although the hadronic and muon loop contributions are small relative to the present experimental error, they might be relevant for the future muon lifetime experiments. But the hadronic uncertainty is still well under control.

Combining the two-loop corrections from the photon loops, electron loops and e^+e^- pair production together with the exact result for muon loops gives the second order QED corrections to the muon decay,

$$\Delta\Gamma^{(2)}_{QED} = -\Gamma_0\Big(\frac{\alpha_r}{\pi}\Big)^2\Big[\frac{156815}{5184} - \frac{1036}{27}\zeta(2) - \frac{895}{36}\zeta(3) + \frac{67}{8}\zeta(4) + 53\zeta(2)\ln(2)\Big]$$

$$= \Gamma_0 \Big(\frac{\alpha_r}{\pi}\Big)^2 \times 6.743 \tag{2.12}$$

This expression contains all corrections of $\mathcal{O}(\alpha^2)$, $\mathcal{O}(\alpha^3 \ln(m_e^2/m_\mu^2))$, and $\mathcal{O}(\alpha^i \ln^{i-1}(m_e^2/m_\mu^2))$ for all $i \geq 2$. Adding the hadronic and tau loop contributions, the total second order correction becomes

$$\Delta\Gamma^{(2)} = \Gamma_0 \Big(\frac{\alpha_r}{\pi}\Big)^2 \times (6.700 \ \pm \ 0.002) \tag{2.13}$$

where the error is a conservative estimate of the hadronic uncertainty. This two-loop correction is at the level of 37×10^{-6} (37 ppm) to the tree level width, and the uncertainty from the calculation is at 10^{-9} order. This theoretical uncertainty is negligible with respect to the final G_F value.

2.1.3 The Fermi Coupling Constant

With the current best value of the experimental muon lifetime for $\tau_\mu = 2.197\ 03 \pm 0.000\ 04\ \mu$s (18 ppm), the Fermi coupling constant [5] is calculated as

$$G_F = (1.166\ 37 \pm 0.000\ 01) \ \times \ 10^{-5}\ \text{GeV}^{-2} \tag{2.14}$$

which represents a reduction in the overall error on G_F of about a factor of 2 with respect to previous value. G_F is now known to 9 ppm uncertainty, which totally comes from the experimental uncertainty on the muon lifetime measurement. The theoretical error in the value of the Fermi coupling constant is rendered negligible compared to the experimental uncertainty.

Although, the muon lifetime τ_μ has been used to define the Fermi constant because of its very precise experimental value, the leptonic tau decay can be used to determine the G_F in an analogous way. These Fermi constants have been normalized, through $\mathcal{O}(\alpha)$, such that $G_{\tau e} = G_{\tau\mu} = G_\mu$ in the standard model [6]. The value for $G_{\tau e} = 1.1666(28) \times 10^{-5}\ \text{GeV}^{-2}$, and $G_{\tau\mu} = 1.1679(28) \times 10^{-5}\ \text{GeV}^{-2}$ were calculated through the corresponding tau decay branch rate. These Fermi constants are in very good agreement with G_μ at the $\pm 0.2\%$ level. These good agreement between G_μ and G_τ can be used to constrain new physics.

2.2 Muon Decay in the Storage Ring

In the (g-2) experiment, the muons were longitudinally polarized when they were injected into the muon storage ring with the relativistic speed. The differential branching ratio in the muon rest frame Eq. 2.4 has to be boosted into lab frame. Let's rewrite Eq. 2.4 as

$$\mathrm{d}^2\Gamma = \left(\frac{G_F^2 m_\mu^5}{192\pi^3}\right) n(\epsilon)\,[1 + a(\epsilon)\cos\theta]\,\mathrm{d}(\cos\theta)\,\mathrm{d}\epsilon, \tag{2.15}$$

where $\epsilon = E_e/E_{max}$, and θ is the angle between the muon spin and the electron/positron momentum (for negative muon, $a(\epsilon)$ carries a negative sign), and

$$\begin{aligned} n(\epsilon) &= (3-2\epsilon)\epsilon^2 \\ a(\epsilon) &= \left(\frac{2\epsilon-1}{3-2\epsilon}\right) \end{aligned}$$

are the number and asymmetry as a function of the electron energy. Because the muons were highly relativistic in the lab frame, the isotropic angular distribution of decay electrons is skewed toward the forward direction. Thus, the choice of a certain energy threshold in the lab frame selects a range of decay angles in the muon rest frame. Applying the Lorentz boost $\gamma_\circ = 29.3$ to $n(\epsilon)$ and $a(\epsilon)$ gives the corresponding functions in the lab frame [35],

$$\begin{aligned} N(\epsilon) &= \frac{5\epsilon - 5}{4\epsilon^2 - 5\epsilon - 5} \\ A(\epsilon) &= \frac{1 + \epsilon - 8\epsilon^2}{4\epsilon^2 - 5\epsilon - 5} \end{aligned}$$

where now $E_{max} = \sqrt{p_\circ^2 c^2 + m_\mu^2 c^4}$. In the (g-2) experiment, the functions $N(\epsilon)$ and $A(\epsilon)$ are optimized to measure the anomalous spin precession by choosing the appropriate electron energy range. The asymmetry $A(\epsilon)$ is a measure of the tendency of higher-energy electrons to be preferentially produced with momenta along the direction of the muon spin. For a given detector, a different electron counting rate is observed when the muon spin points toward the detector than when it points away. The larger the electron energy ($\epsilon \to 1$), the larger this effect ($A(\epsilon) \to 1$).

Under the constraint of $\vec{B}$ field and weak focus $\vec{E}$ field, the muons circulate around the ring with the anomalous precession frequency $\vec{\omega}_a$,

$$\vec{\omega}_a = \vec{\omega}_s - \vec{\omega}_c = -\frac{e}{mc}\left[a_\mu \vec{B} - \left(a_\mu - \frac{1}{\gamma^2 - 1}\right)(\vec{\beta} \times \vec{E})\right] \tag{2.16}$$

For the specific value $\gamma_\circ \approx 29.3$, satisfying the relation

$$a_\mu - \frac{1}{\gamma_\circ^2 - 1} = 0, \tag{2.17}$$

the $\vec{\beta} \times \vec{E}$ term is reduced to zero, and the dependence on $\vec{E}$ disappears. Choosing this so-called "magic gamma" sets the muon momentum to $3.094\text{GeV}/c$. Running the experiment at this momentum means that the use of electric quadrupole fields to provide weak vertical focusing of the muon beam does not affect ω_a to the first order. In this case, $\vec{\omega}_a$ is independent of the Lorentz boost $\gamma_\circ$, and a precise determination of a_μ can be obtained by precise measurements of ω_a and B,

$$\omega_a = \frac{e}{mc} a_\mu B. \tag{2.18}$$

Meanwhile, the lifetime of the stored muons is dilated by a factor of γ_0 in the (g-2) experiment. The dilated muon lifetime $\tau_\mu = \gamma_\circ \tau_0 \approx 64.4\ \mu\text{s}$. The exact values of the dilated lifetime τ_μ and the dilation factor γ are the topic of this thesis.

The measurement of the muon decay spectrum modulated by the spin precession in the number of electron counts with time in a given detector is the method by which τ_μ and ω_a are determined. The function that describes the exponential decay of the stored muon population is

$$N(t, \epsilon) = N_\circ(\epsilon) e^{-t/\tau_\mu}\left[1 + A(\epsilon)\cos(\omega_a t + \phi(\epsilon))\right] \tag{2.19}$$

Because the time it takes a electron to travel from the point of decay to the detector depends on its momentum, there is an energy dependence to the phase $\phi(\epsilon)$, hereafter referred to as the "g-2" phase.

The statistical precision σ_{τ_μ} with which τ_μ can be known is

$$\sigma_{\tau_\mu} = \frac{\tau_\mu}{\sqrt{N_{total}}} \tag{2.20}$$

where N_{total} is the total muon number in the ring. Appendix C gives the detailed derivation. The uncertainty of the lifetime τ_μ depends only on the total muons in the ring. For $N_{total} = 3.0 \times 10^9$ decay positrons (electrons) in the (g-2) experiments, the statistical uncertainty on the muon lifetime could reach up to 18 ppm. This statistical uncertainty matches the current best experimental measurement of positive muon, and three times better than that of negative muon.

Chapter 3

Experimental Setup

The muon (g-2) experiment E821 at Brookhaven National Laboratory (BNL) Alternating Gradient Synchrotron (AGS) was designed to measure the muon anomalous magnetic moment a_μ to a precision of 0.35 ppm. Ancillary experiments included the muon lifetime τ_μ and the muon electric dipole moment (EDM) [36]. Although the general method of this experiment was similar to that of the previous CERN (III) experiment [17], many features in the experiment were improved by using new technologies, for example, a superconductor inflector for injection and a continuous super-ferric magnetic ring. In this chapter, the details of the experimental setup will be described.

3.1 The Muon Beam and Beamline

The schematic overview of the BNL muon (g-2) experiment setup is shown in Fig. 3.1. The AGS delivered 12 proton bunches[1] at the momentum of 24 GeV/c to V-line in every AGS cycle of 2.6 seconds. The bunches were separated by about 33 ms. Typically, 20-60 Tera-protons (Tp) per AGS cycle strike the nickel target in the V-line and produced pions. The nickel target was designed to withstand high beam intensities. It consisted of 24 nickel

[1]Depending on the mode of operation, 6 to 12 proton bunches can be extracted per AGS cycle. In 1999, 6 proton bunches were extracted per AGS cycle. In both 2000 and 2001 run, 12 proton bunches were extracted in every AGS cycle.

disks 15 cm in diameter and 6.4 mm thick. The disks rotated about its axis and was cooled with water to minimize thermal stress. After the target, the resulting pions were focused

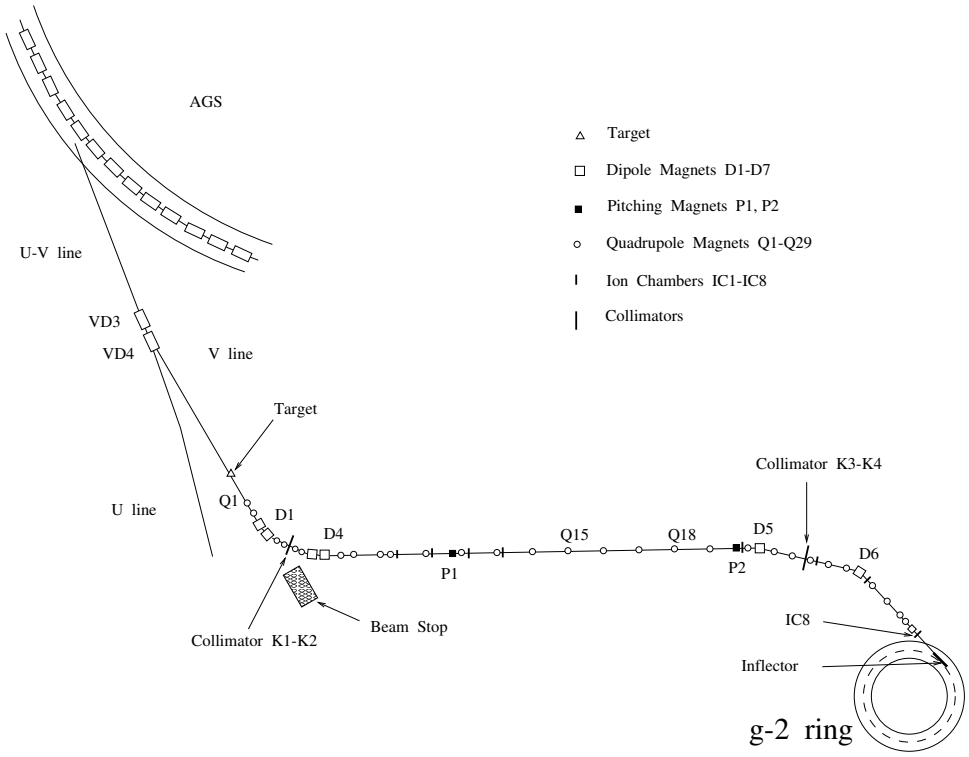

Figure 3.1: Diagram of the beamlines for BNL (g-2) experiment.

by quadruples Q1 and Q2, and were momentum selected through dipoles D1 and D2 and the collimator K1-K2. K1 determined the upper limit on the pion momentum and K2 the lower limit. The selected pions had a central momentum of 3.11 GeV/c, about 0.5% above the muon "magic" momentum of 3.094 GeV/c. These pions were then transported along a 116 m secondary beamline to the muon storage ring. During their 89 m long flight between collimators K1-K2 and K3-K4, about 40% of the pions underwent the decay process $\pi \rightarrow \mu\nu_\mu$. The collimators K3-K4 along with the dipole magnets D5 and D6 were used to select the final momentum of particles to be injected into the storage ring. Pion injection was used in the first run in 1997, while in both 2000 and 2001 runs, muon injection was

used. Muons with "magic" momentum 3.094 GeV/c were selected. These high energy decay muons were highly polarized with the average of 92% longitudinal spin polarization.

Inside of the muon transport beamline, a series of ten Segmented Wire Ion Chambers (SWICs) monitored the beam horizontal and vertical position. The beam profile from these detectors were used to tune the beam. The tuning was necessary to maximize the pion and muon transport efficiency. Other detectors were also used to monitor the intensity of the beam at various points. The eight Ionization Chambers (ICs) placed at various locations between the target and the storage ring (see Fig. 3.1) were used to measure the beam pion/muon intensity. A calibrated Secondary Emission Chamber (SEC) was placed immediately downstream of the target to measure the proton intensity. The beam flux information from each of these detector systems was important in tuning the beam.

A Čerenkov counter was used to study the composition of the beam just before injection into the storage ring. In the 2000 run, at this point, the beam consisted of approximately equal numbers of μ^+, π^+, and e^+. The p^+ number was estimated to be about one third of the pion number so that the beam was made of 30% μ^+, 30% π^+, 30% e^+, and 10% p^+[38]. In the 2001 run, the same study showed the composition of 37% μ^-, 33% π^-, and 30% e^-, when the ratio of ICs to SEC was $\sim$ 0.33. Anti-protons were negligible at the injection point. A different IC/SEC ratio meant different beam composition. During the normal data taking period, the Čerenkov counter was removed from the beam path, while the IC/SEC ratio was constantly monitored to maintain the measured composition.

A pulsed sweeper magnet was installed in the pion decay channel during the 2000 run. This was to prevent the accidentally extracted protons passing through the secondary beamline and reduced the background in the calorimeters (so-called "flashlets") during the data taking period. The sweeper magnet was turned off at the time of injection, and quickly ramped up to a field of 50 mT during the ensuing 15 μs. This was sufficient to stop the particles extracted out of time from being injected into the storage ring.

3.2 Superconducting Inflector

A direct current iron-free superconducting magnetic inflector was used to inject muons into the (g-2) storage ring [39]. The 1.7-meter-long inflector, placed inside a hole in the magnet yoke, created a magnetic dipole field which locally canceled the 1.45 T main magnetic field from the storage ring, so that the muons entered the storage region over as short a path as possible. A diagram of the superconducting inflector is shown in Fig. 3.2. The radial distance between the injection point and the storage ring equilibrium orbit was only 77 mm. Any field leakage could influence the uniformity of the main magnetic field. The truncated double cosine theta design of the inflector made it possible to trap most of the return field [40], and the remaining fringe field was trapped by a special superconducting shielding sheet surrounding the magnet.

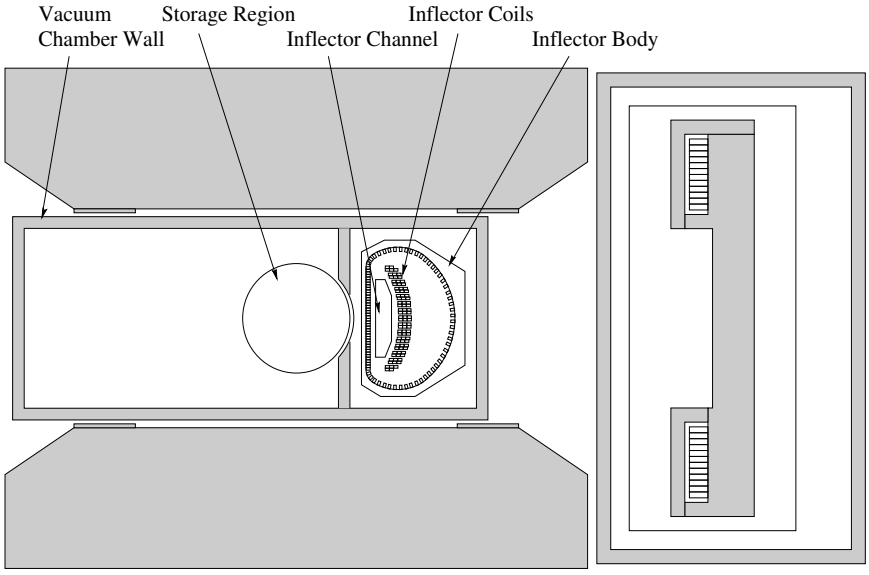

Figure 3.2: Cross section of the superconducting inflector at the point of injection. The two outer coil blocks of the main magnet are also drawn to the right.

The inflector was operated using a warm-to-cold cryogenic cycle. When the main magnet was powering up, the inflector was not in the superconducting state. The 1.45 T magnetic

field flux went through the shield. Then the inflector was cooled down by two phase helium, and both its coils and shield became superconducting. A DC current of 2700 A was applied to the coils to excite the field to cancel the magnetic flux inside the inflector. The large change of the magnetic field was trapped inside the inflector by the internal eddy currents in the shield and did not affect the precision field of the ring.

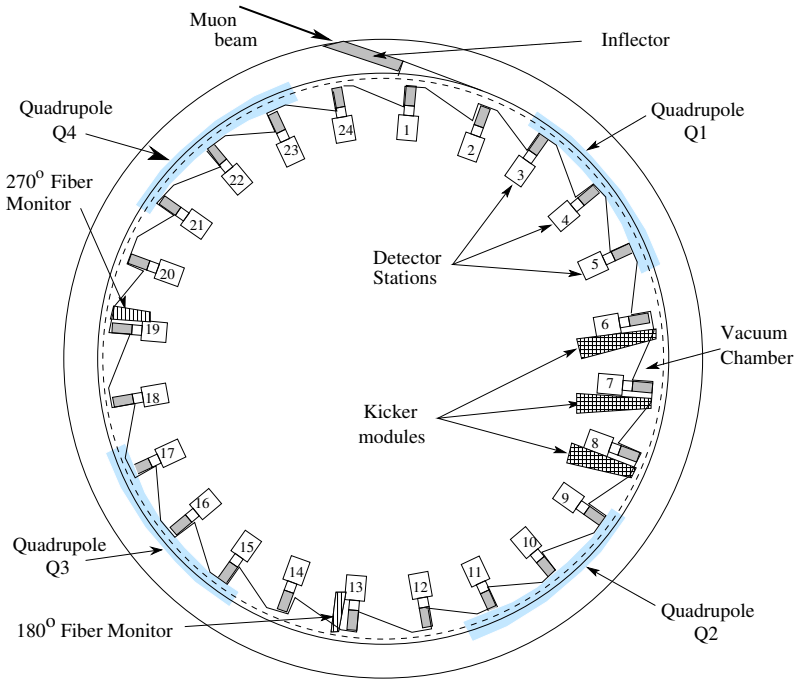

Figure 3.3: A schematic view of the muon storage ring featuring in particular the superconducting inflector, three kicker modules, four focusing quadrupole plates (Q1-Q4) in blue shade, and two fiber beam monitors (FBM). (Reproduced from reference [37])

3.3 Muon Storage Ring

After the superconducting inflector, the muons were injected into the muon storage ring. The BNL muon storage ring had been built as a single continuous magnet with a diameter of 14.2 m. The super-ferric magnet created a highly homogeneous dipole magnetic field of 1.45 Tesla, which constrained the 3.094 GeV/c muons to move in a circle with a central orbit radius of 7.112 m. To avoid the muons striking the inflector and being lost, the magnetic kickers were used to place them onto stable orbits. The electrostatic quadrupoles provided the weak vertical focusing necessary to store the muons. The locations of these various elements are shown on the schematic view of the muon storage ring in Fig. 3.3.

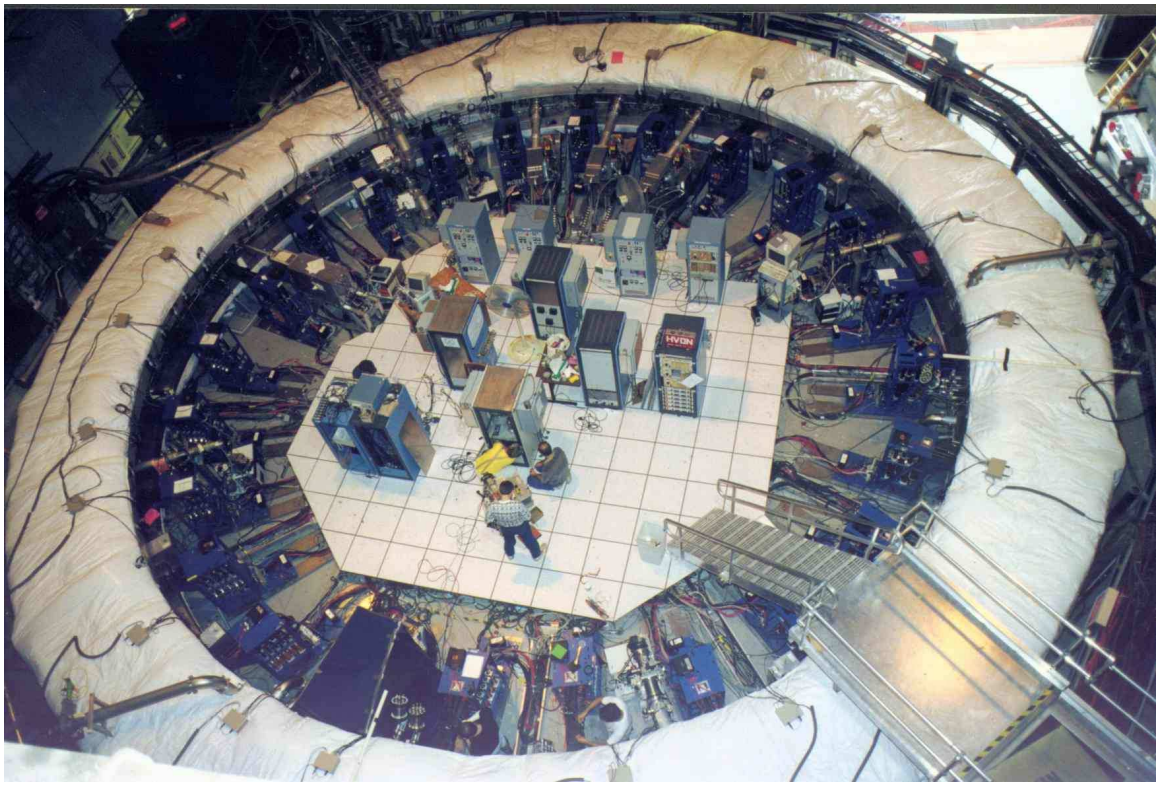

Figure 3.4: Photograph of the muon (g-2) storage ring with the thermal insulator.

3.3.1 Main Magnet

The storage ring was built as one continuous super-ferric magnet, an iron magnet excited by three superconducting coils [41]. The C-shaped magnet had the opening facing toward the center of the ring, since the decay electrons were bent inward by the magnetic field. A photograph of the ring is shown in Fig. 3.4. The whole ring magnet was constructed with twelve 30° yoke sectors. Each sector was made of steel plates and consisted of an upper and lower yoke separated by a spacer plate. A cross section of the magnet was shown in Fig. 3.5. In order to achieve the required uniformity of the magnetic field, extensive shimming work

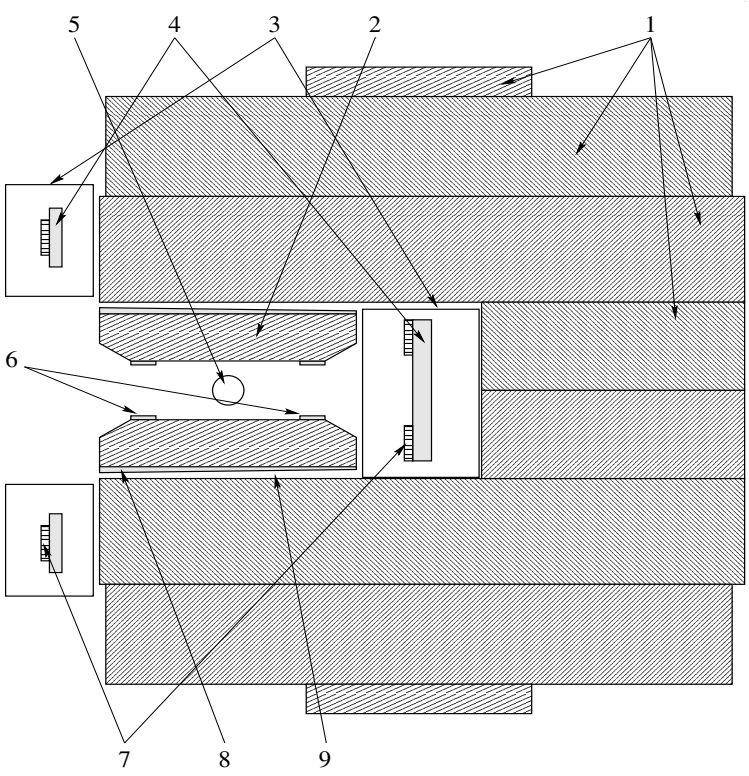

Figure 3.5: Cross section of the main magnet. The various sections are 1. yoke plates; 2. pole tip; 3. cryostat; 4. mandrel; 5. muon storage region; 6. rose shims; 7. superconducting coils; 8. wedge shim; 9. air gap. The opening points to the center of the ring (left).

was required, including the adjustments to the yoke plates tilt and end shims of the poles,

inserting iron wedges in the air gap between the yokes and the poles, and adding correction coils on the pole surfaces [42, 43]. To reduce the field fluctuation due to the temperature variation during day and night, thermal insulation was installed to cover both the yoke and poles (see the white insulation on the ring photograph).

Two inner and one outer superconducting coil excited the 1.45 Tesla field. The advantage of using the niobium-titanium superconducting coils was obvious. The superconducting coils had good thermal stability and once cold, they consumed relatively low power, needing only low voltage to maintain the required 5200 A current. The coils were housed within aluminum cryostats, which were thermally isolated from the yoke plates.

The magnetic field in the storage region was measured periodically between data-taking periods by a set of 17 NMR probes housed inside a cylindrical trolley. During data taking, the field was monitored by a set of 378 NMR probes fixed to the top and bottom of the vacuum chamber walls.

3.3.2 Vacuum Chamber

An aluminum vacuum chamber filled the space between the magnet poles. They consisted of twelve sections to match the magnet sectors. Within the vacuum chamber was the actual

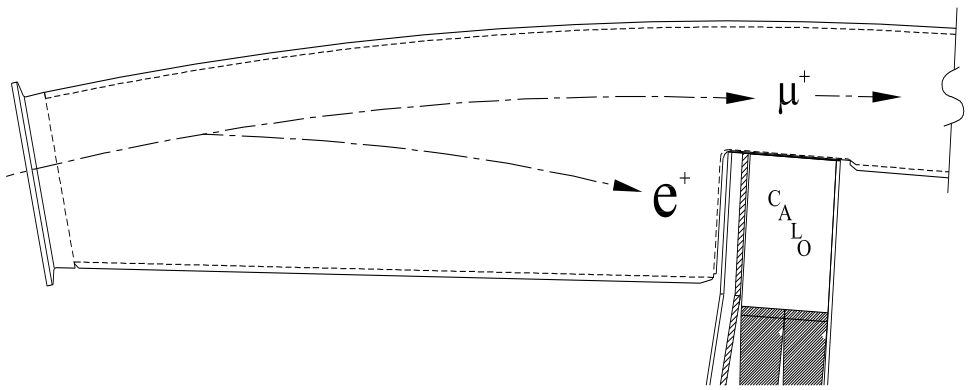

Figure 3.6: The trajectories of a muon and a decay electron, respectively, in the scallop-shaped vacuum chamber. Reproduced from [50].

storage region which had a cross-section of 9 cm in diameter. The storage aperture was defined by a set of copper collimators [44]. These circular copper collimators were 3 mm thick. Muons striking the collimator would undergo multiple scattering, and were lost after a few turns. The vacuum level in the chamber was maintained in the range of 10^{-7} torr by a combination of turbomolecular, ion, and cryogenic vacuum pumps. Fig. 3.6 shows the top view of a part of the vacuum chamber, and Fig. 3.7 shows a cross section view of the vacuum chamber. The chamber sections were scallop-shaped to minimize the scattering and pre-showering of the decay electrons on their way to the calorimeters. The support frame inside each chamber section provided rails for the NMR trolley. There were about 31 fixed NMR probes embedded in the top and bottom walls of each vacuum chamber.

3.3.3 Magnetic Kickers

A fast muon kicker was necessary in the muon injection. Muons exiting the superconducting inflector had approximately a parallel orbit to the central orbit, but 77 mm further out in radius. The trajectory of the injected muons must be altered to avoid striking the inflector at the end of the first turn. This was achieved by applying three fast magnetic kickers located at 90° downstream of the inflector [45]. Each kicker consisted of a pair of 1.7 m long aluminum plates, a width of 8 cm and a thickness of 0.75 mm. The fast kicker was fired at 95 kV high voltage and produced a peak current of 4200 A with a half-period of 400 ns. The current pulse was formed by an under-damped LCR circuit. The switching of the high voltage was performed by deuterium thyratron tubes. The kickers provided ~ 10 mrad shift to the muon beam and placed them onto the storage orbit.

3.3.4 Electrostatic Quadrupoles

The muon beam in the storage ring was focused horizontally by the main magnetic field and vertically by electric quadrupoles. At the magic momentum, the electric field did not affect the anomalous precession frequency. There were four quadrupole regions in the storage ring

which are shown as the long (blue) shades with labels Q1, Q2, Q3 and Q4 on Fig. 3.3. Each quadrupole region consisted of an electrode azimuthal length of 39°. The four-fold symmetric electrodes occupied 43% of the total circumference [46]. Fig. 3.7 shows the cross section of the vacuum chamber with quadrupole electrode plates mounted on the vacuum chamber wall. The top and bottom electrodes were 3 mm aluminum plates. The inner and outer electrodes were 0.5 mm thick except the Q1 outer plate, which was only 0.10-0.13 mm thick to allow the injected muons passing through without lossing much energy. It was found that the decay electrons lost negligible amount of energy when spiraling through the thin aluminum plates.

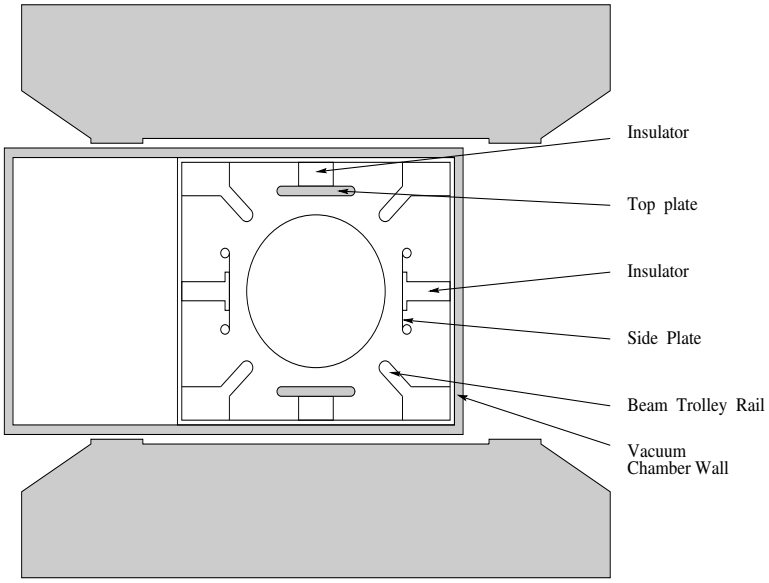

Figure 3.7: The cross section view of the electric quadrupole within the vacuum chamber. The electrodes are mounted on the vacuum chamber wall. The ring center is on the left.

The average field index n is defined as following in the presence of the dipole magnetic field B and electric field gradient $\partial E_R/\partial R$,

$$n = \frac{R}{\beta B}\frac{\partial E_R}{\partial R} \tag{3.1}$$

where $\beta = v/c \approx 1$, $R = 7.112$ m was the radius of the central orbit, and $B = 1.45$ T. The

n-value used in 2000 run was 0.137 with 24.0 kV applied to the quadrupole electrodes. In 2001, two different tunes were used. In one case, $n = 0.122$ with high voltage of 21.7 kV, and in another case, $n = 0.142$ with 25.3 kV. The choice of applied voltage determined a number of interesting characteristics of the dynamics of the muon beam [47].

To minimize the muon losses at later time, *scraping* was implemented after injection. The muon beam was shifted slightly off the central orbits by applying asymmetric high voltage values on the electrodes. Therefore muons with a large injection angle or with momenta too different from the magic value scattered on the collimators and got lost. The asymmetry scraping voltage, i.e. the difference between the initial setting and the operating voltage, was set to 7 kV for most of the data in 2000 and 2001. The scraping time was set to 16 μs in 2000, while it was shortened to 7 μs in 2001. After the scraping time, the high voltage of the scraping plates were recovered to the operating voltage with a rise time of 5 μs. During normally data taking period, the high voltage was pulsed on for $\sim$ 1 ms when muons were stored in the ring, then it was turned off to avoid electrical breakdown.

3.4 Beam Monitor Detectors

3.4.1 T0 Counter

The T0 counter was used to monitor the incoming muon beam and provide a beam injection reference time. It was a 1 mm thick by 10 cm diameter Lucite Čerenkov counter located immediately upstream of the inflector. The light collected from the counter was proportional to the number of particles passing through the counter. The trace shape of the T0 signal on its Wave-Form Digitizer (WFD) was a good approximation of the muon beam bunch shape before it entered the storage ring, and the area of its WFD trace was proportional to the intensity of the incoming beam for that particular fill. Fig. 3.8 shows a typical WFD trace of the T0 signal. It was digitized by WFD operating at a 200 MHz clock, but interleaved to provide 2.5 ns timing bin. The amplitude was in ADC counts unit. The trace can be fitted by a Gaussian function with a constant pedestal. The RMS width of the Gaussian

fit was about 28 ns for this sample. The fitted mean time of the T0 pulse was designated $t = 0$ in order to align the fills in time for analysis purposes. Also, the characteristics of the T0 trace (e.g. size and shape) were used to identify and eliminate bad fills at the data selection stage.

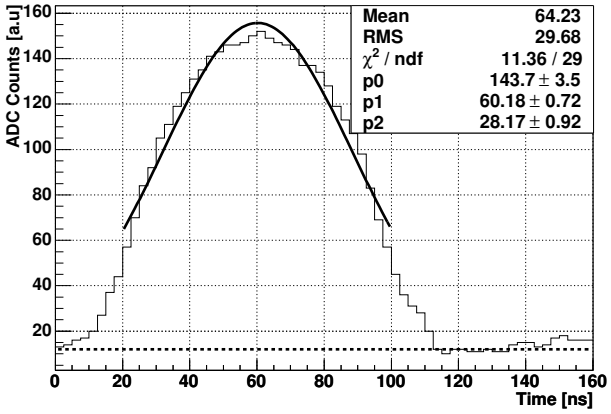

Figure 3.8: A typical WFD trace of the T0 counter signal. The trace was fitted by a Gaussian function (solid line) with a constant pedestal (dashed line).

3.4.2 Fiber Beam Monitor

The profile of the stored muon was monitored directly by two scintillating fiber detectors, which were located at 180° and 270° downstream from the injection point (as shown in Fig. 3.3). Each detector contained a vertical and a horizontal plane set, and each plane set consisted of seven scintillating fibers, 0.5 mm in diameter, separated by 10 mm. Light output from the fibers was sent to photomultiplier tubes via clear fiber feedthroughs. The fibers and PMTs were calibrated with respect to each other by rotating the plane 90° to expose all fibers to the same portion of the beam. Fig. 3.9 shows a vertical set of fiber monitor at measurement position and calibration position, respectively. The fiber monitor measurement was destructive to the stored muons, since muons strike on the fibers would undergo multiple scattering and be lost. Therefore, the fiber monitors were only inserted

into the storage region for dedicated beam dynamics studies.

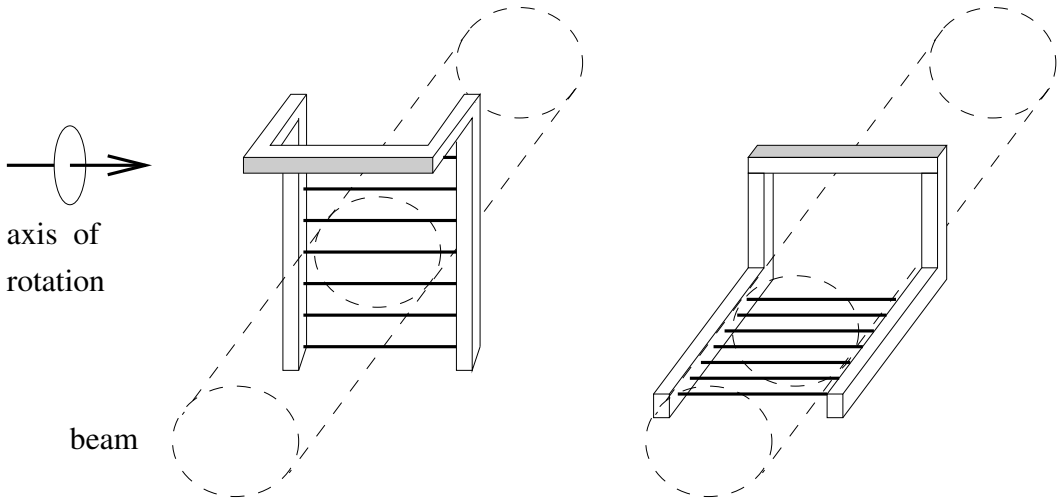

(a) measuring position (b) calibration position

Figure 3.9: A vertical set of scintillating fiber monitor at two positions. During the normal data taking period, the fiber monitors were moved out the storage region.

3.4.3 Traceback Wire Chamber

The traceback wire chamber system was designed to make a non-destructive measurement of the muon profile in the storage region by reconstructing the muons through the decay electron trajectories in the chambers [48]. The traceback detector consisted of four identical XY drift wire chambers as shown in Fig. 3.10. Each chamber contained two planes, a vertical chamber plane and a horizontal chamber plane, and each plane consisted of three columns of straws. Each drift tracking straw was composed of a 15 micron diameter gold plated tungsten anode sense wire, and 8 mm inner diameter spiral wound aluminized mylar straw cathode. This wire chamber used a mixture gas of argon (47.5%), carbon dioxide (47.5%), and ethane (5%). The detector was located just before calorimeter station 20, whose signal was used as a trigger for the wire chambers. The scallop-shaped vacuum chamber wall was

shortened to allow for the placement of the chamber. Also, a 14 μm thick plastic window was constructed in the exit wall of the vacuum chamber to minimize the multiple scattering of the incoming electrons. Decay electrons spiraling radially inward pass through the drift

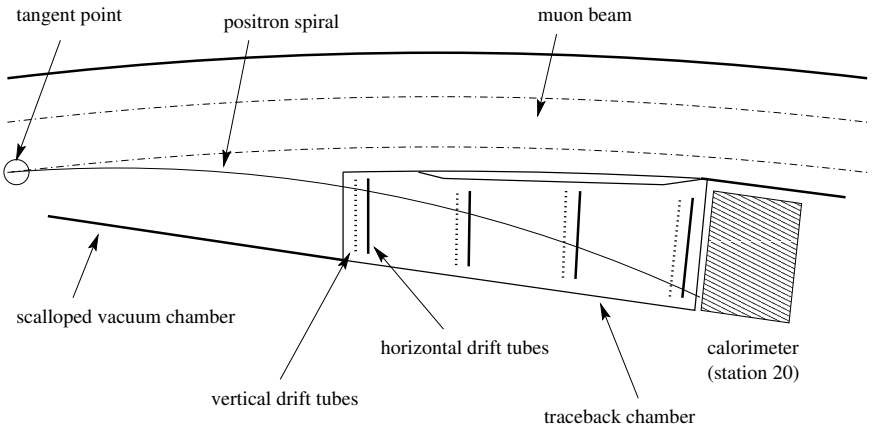

Figure 3.10: The diagram of the traceback wire chamber. It consists four identical horizontal and vertical drift tube tracking chambers. (Reproduced from [51])

tubes, ionize the gas mixture, and create position signals. The signals from a group straws in both horizontal planes and vertical planes defined the X-Y position of the particle. The passage of the decay electron in the wire chamber was traced back to the storage region in the vacuum chamber, where a possible muon decay point was found. If at any time, there were more than one straw cluster ionized in the same plane, the event could not be fit, and therefore it was thrown out. This set the limitation of the traceback chamber starting time, which was later than 100 μs. The precise position of the muon decay could not be recovered for any individual event; the tracking program traced the electron paths until the maximum radius was found. The resultant beam profile could be related statistically to the actual muon distribution. The traceback was used to reconstruct trajectories for electrons with energy between $\sim$ 1.5 GeV and 3.1 GeV. The lower-energy electrons spiraled inward with a smaller radius of curvature in the fringe fields of the magnet and did not pass through all four planes and reach the calorimeter to create a trigger. The traceback system functioned

in 2000 and in the first part of 2001 run. The data have been used to perform a muon EDM analysis [49].

3.5 Electron Detectors

3.5.1 Electromagnetic Calorimeters

The decay electrons from the stored muons were detected by 24 compact electromagnetic calorimeters distributed at uniform intervals inside of the (g-2) storage ring[50]. Fig. 3.11 shows a diagram of a calorimeter station within its support frame. The calorimeter was made of polystyrene-based scintillating fibers, 1 mm in diameter, embedded in a lead alloy (Pb/SciFi). Each calorimeter was 22.5 cm wide, 14 cm high, and 15 cm deep. The plastic-to-volume ratio was adjusted to yield an effective radiation length X_0 about 1 cm, which implied that the 15 cm deep detectors were 13 X_0 deep. For the electron energy between 1-3 GeV, this depth corresponded to a 93-96% shower containment fraction. The calorimeter block was inserted into position along the scalloped vacuum chamber walls as shown in Fig. 3.6 such that the fibers were oriented perpendicularly to the incoming electron trajectories. Lower energy electrons had smaller radii in the fringe field of the magnet. By choosing the reasonable width and depth of the calorimeter, these electrons curled away between the gaps of calorimeters, thereby reducing the overall event trigger rate. A simulation study showed that the calorimeter coverage around the ring was sufficient to capture 87% of positrons above 0.8 GeV [51].

To reduce the high instantaneous rate effecting the timing and gain stability on the readout system, the calorimeter was divided into four separate segments glued to each other. The light from each of the quadrant was collected by a tapered UV-absorbing acrylic lightguide, which then piped the light to the 2" photomultiplier tube (PMTs) through its 1 m long rod. The PMT provided a fast signal risetime and a short pulse duration which were essential to the precision measurement of the event time. The PMTs, which were covered by the steel shields, were placed far away from the storage ring central plane (see

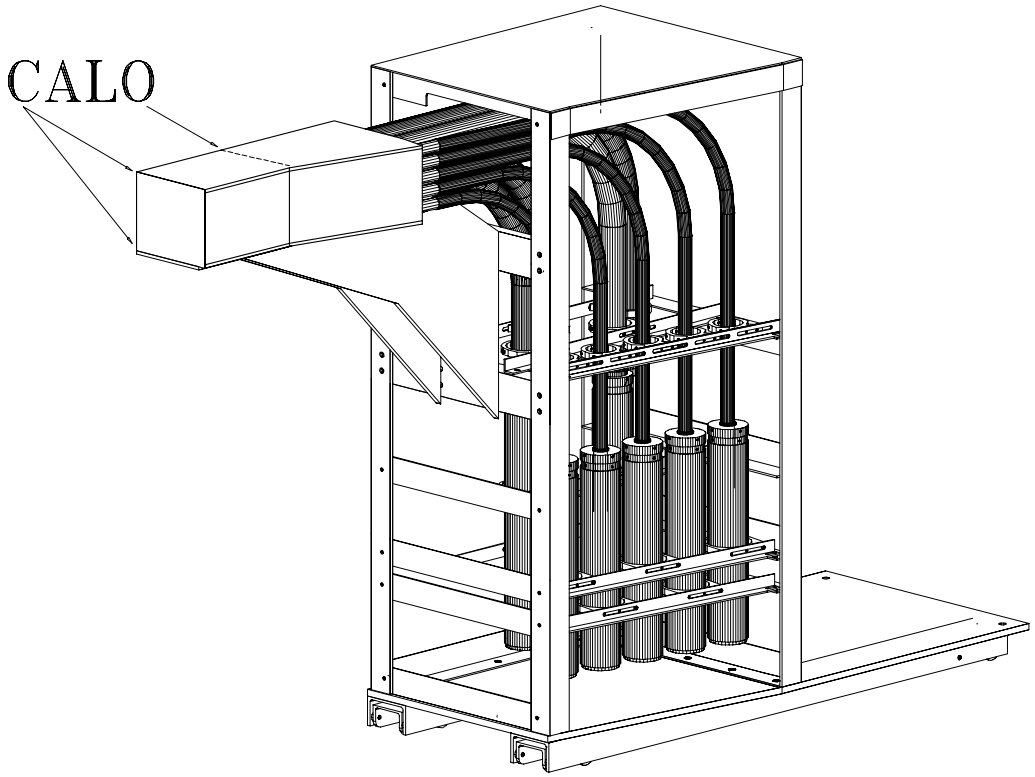

Figure 3.11: 3D view of the calorimeter detector station on the support frame. The acrylic lightguide pipes the light through its long rod to the PMTs far away from the magnet mid-plane. FSDs are mounted in front of the calorimeter and their light guides are shown. (Reproduced from reference [50]).

Fig. 3.11), in order to minimize effect of the fringe field from the magnet. The PMTs were turned off by a special gating circuit on their bases at early times after each injection to avoid the damage from the strong flash. The flash was more severe near the inflector and kicker region. Some detectors near this region remained off for as long as 45 μs in 2000. The PMTs each had two identical outputs; one was sent to a custom-made VME (Versa Module Europa) waveform digitizer (WFD), and the other was sent to a standard CAMAC analog-to-digital converter (ADC) module (see Sec. 3.6).

The absolute energy calibration of the calorimeters was performed in the BNL test beam before the (g-2) test run in 1997. The average resolution was about $\sigma/E = 6.8\%$

for 2 GeV electrons. For electron energy between 1 GeV and 3 GeV, the calorimeters had a linear response of better than 1%. During data taking, two relative calibration systems were maintained. One was based on light-emitting diodes (LED), and the second used a laser-illuminated fiber optic system. These calibration systems were also used to monitor short-term time and gain stability of the response of the calorimeters. This calorimeter with PMT readout system had achieved excellent stability in the experiment. It had less than 20 ps timing shift and less than 0.2% energy shift in 200 μs and with a wide event rate range from peak counting rate $\sim$ 2 MHz to several tens Hz at $\sim$ 800 μs.

3.5.2 Front Scintillating Detectors (FSDs)

A set of five scintillating tiles mounted in front of each calorimeter provided the vertical position information of the incoming electrons. These FSD tiles were 1 cm thick, 22.5 cm long, and 2.8 cm high plastic scintillators. The five segments covered the entire front face of the calorimeter. Similarly to the calorimeter, the light signal from each scintillator was collected by lightguide and transported through a long acrylic rod to the 1" PMTs located far away from the magnet mid plane (see Fig. 3.11). For the same reason as the calorimeters, the FSD PMTs were also covered in the steel shields, and their bases were gated on later after the injection. The FSD PMT signals were sent to discriminators. The thresholds for the discriminators were fine-tuned by looking at the FSD outputs in a WFD to determine the amplitude of minimum ionizing particle (MIP) signals. The outputs of the discriminators were routed to multi-hit time to digital converters (MTDCs) which recorded the time of hits in each FSD tile.

Although the FSD position and time information were designed to study the time coincident (pileup) events in the calorimeter, they were practically used for *electric dipole moment* (EDM) and muon loss studies since a novel approach for pileup spectrum construction was developed. A nonzero intrinsic muon EDM would tilt the anomalous precession plane and cause a vertical oscillation. The EDM analysis based on FSD data

had been finished for the 2000 data[52], which gave a vertical oscillation amplitude of $-1.3 \pm 5.9(stat) \pm 10.4(syst)$ mrad consistent with no EDM signal. It gave an EDM measurement of $(-0.1 \pm 1.4) \times 10^{-19}$ e-cm for positive muons. This result is consistent with zero, and a new EDM limit is set at 2.8×10^{-19} e-cm at 95% confidence level.

Both the lost muons from the storage ring and the decay electrons are MIPs in the scintillators, and they excite the electron shells when passing through the atoms in the tile. Comparable light signals were emitted when the excited atoms return to their ground states. In contrast the muons do not produce electromagnetic shower in the calorimeters, and lose very little energy. Therefore, the lost muon time spectrum could be constructed by looking for three-fold coincident events in successive FSDs (see Sec. 5.6). The muon loss time spectrum is essential to the muon lifetime analysis. Although most detector stations had FSD tiles mounted on them, only 11 stations were equipped with PMTs to fully function in 2000, which formed a limited number of three-fold combination. In 2001, four more FSD stations were installed with readout system.

3.5.3 Position Sensitive Detectors (PSDs)

The Position Sensitive Detectors (PSDs) were 2D hodoscopes of both horizontal (X) and vertical (Y) scintillating tiles [53]. The Y plane consisted of twenty 22.5 cm long tiles to provide the vertical position, and the X plane consisted of thirty two 14 cm long tiles which provided the horizontal position. All PSD tiles were 7 mm wide by 8 mm deep with an embedded wavelength shifting fiber in the middle. Like the FSDs, the PSDs were mounted in front of the calorimeters along the path of decay electrons.

In 2001, there were five PSD stations. One of the PSDs was equipped with multi-channel photomultiplier tube (MCPMTs), and the other four used *hybrid photodiode* (HPDs) [54] to read out the fibers. The HPDs were more uniform than MCPMTs. The resulting electronic signals were sent into discriminators, and the outputs of the discriminators were sent to the custom readout electronics. The PSD readout was usually triggered by the calorimeter.

Once the calorimeter signal reached the threshold, the time of the trigger was recorded, along with a bitmap indicating which PSD channels were fired in coincidence with the trigger. At the end of each fill, this data was sent to the PSD VME board which held it for readout by DAQ.

The PSDs provided 5× finer vertical position information than FSDs. In 2001, the PSD data was more favorable to perform the EDM analysis. The phase method [55] which measured the (g-2) phase versus beam vertical position gave the EDM signal of $(-0.48 \pm 1.3) \times 10^{-19}$ e-m for the negative muons. The FSDs could not be used in this method because of its coarser vertical position resolution.

3.6 Data Acquisition System (DAQ)

The analog signals from the calorimeter PMTs were input to the custom designed waveform digitizer (WFD) modules in the counting room. These WFDs were VME [56] standard bus modules which digitized and stored analog input data with 8-bit *flash ADCs* at a rate up to 200 MHz. The four PMT signals from each calorimeter were summed in the WFDs, and two identical copies of the summed signal were sampled at 180° out of phase to give the effective 400 MHz (2.5 ns) resolution. Fig. 3.12 shows the typical analog signal in the WFD for one fill of the beam. At the beginning of each injection, a triangular marker pulse was input to the WFDs a few μs later after receiving a PREPULSE signal from the AGS. The flat region in early times meant the PMTs were gated off. Although the WFDs kept digitizing continuously during the $\sim$ 1 ms storage time, only those signals whose amplitude exceeded the pre-set hardware threshold were written to on-board memory. In 2000, the pre-set hardware threshold was equivalent to $\sim$ 1 GeV positron signal amplitude in the calorimeter. In 2001, it was lowered to 0.9 GeV. For each signal triggering the recording, the WFD also kept at least 6 time bins (15 ns) before and at least 32 time bins (80 ns) after the current trigger signal to record the whole pulse shape. An example of WFD digitized event is also shown on Fig. 3.12. Besides the calorimeter data, the WFDs were also used

to digitize T0 signal, the reference photodiode signal for the laser calibration system, and the muon kicker waveform. The traces of the electric quadrupole waveforms and the signals from the fiber beam monitors were also read out using special WFDs in single-phase mode.

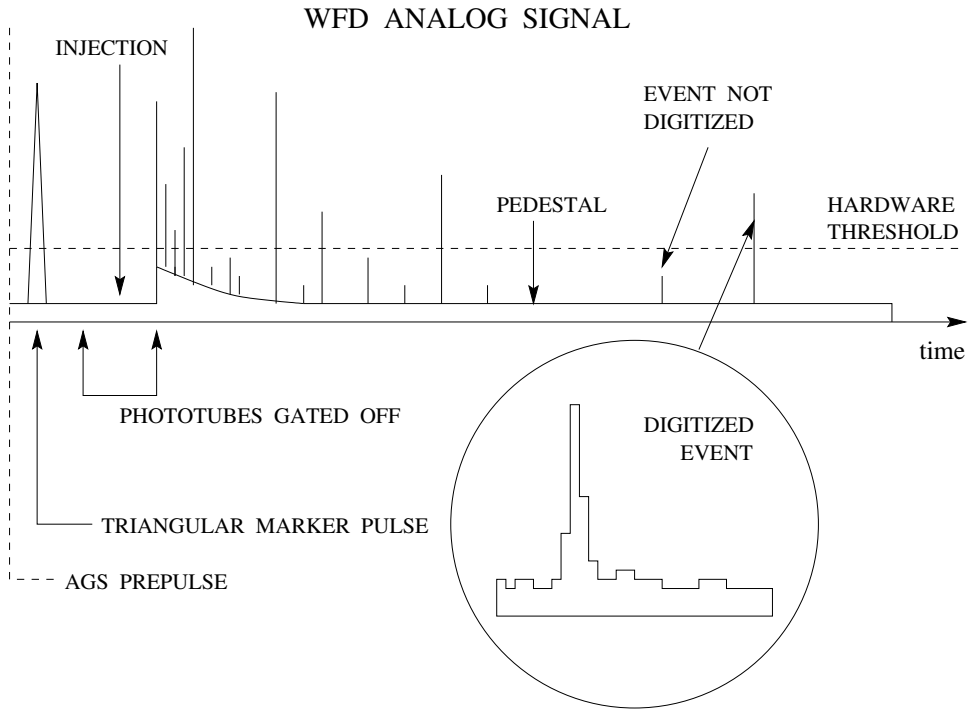

Figure 3.12: A cartoon view of the analog signal in a WFD for one fill of the beam. Analog signals input to WFD were digitized continuously. The digitized signal was written to the on-board memory only when its amplitude exceeded the hardware threshold. (Reproduced from reference [51]).

The signals from FSD PMTs, traceback and time signal from the WFD sum of calorimeter were first discriminated, and then recorded by the custom *multi-channel time-to-digital converters* (MTDCs)[57]. Each MTDC had 27 independent digital inputs. The times of electron events were recorded at 800 MHz (1.25 ns resolution), along with the channel number. Each transition of the input signal (NIM or ECL) was converted into a time word. Because the boundaries of the time bins were potentially rate-dependent, some MTDC

channels used external de-randomizer circuits that placed the input pulse in the center of a 5 ns bin in a stable manner. The laser calibration data was recorded by CAMAC [58] analog-to-digital converters (ADCs) and time-to-digital converters (TDCs). The PSDs had their corresponding electronics.

All electronics systems used in the experiment received clock signals from frequency synthesizers which were stabilized by a 10 MHz reference. This ensured a common frequency standard. This reference was provided by a Stanford Research Systems FS700 module locked to the LORAN-C standard radio frequency. The specifications quoted short-term stability of the FS700 10 MHz signal at the level of 10^{-10}, and stability of the LORAN-C standard to 10^{-12}. The magnetic field measurement electronics utilized this same standard.

The data acquisition system consisted of six 9U front-end VME crates, which housed the WFD, MTDC, and PSD VME modules, and one central 6U VME *Event builder* crate, which connected to the six front-end crates. The front-end crate CPUs read out the data from the on-board memory buffers between each fill of the storage ring in the 33 ms interval and stored the data until the end of each AGS cycle of 2.5 s period. Then the central crate CPU read out the data from each front-end crate between AGS cycles and write it tape. This data acquisition system [59] was controlled by software based on UNIDAQ [60]. An online computer using the LINUX operating system and running UNIDAQ connected the user to the individual VME CPUs via an Ethernet connection. Data from a fraction of the fills (typically 10%) was sent to this computer for immediate online analysis. Calorimeter time and energy histograms, FSD and PSD distributions, and quadrupole traces were examples of information which allowed the user to verify in real time that proper data-taking was occurring.

Chapter 4

Magnetic Field Measurement and Analysis

The uniform magnetic field in the muon storage ring was measured by a pulsed *nuclear magnetic resonance* (NMR) system [61]. The precise value was determined in terms of the free-proton Larmor precession frequency (ω_p) in this magnetic field. A trolley with 17 NMR probes, which were calibrated with respect to the standard probe [62], was used to measure the field around the storage ring twice a week during the experiment running period. A total of 378 NMR probes fixed on the vacuum chamber walls were used to monitor the magnetic field between the trolley runs. The final ω_p result was obtained by weighting the average field map by the muon radial distribution in the storage region [43, 63].

4.1 Principle of Pulsed Nuclear Magnetic Resonance (NMR)

The magnetic field was determined by measuring the proton nuclear magnetic resonance frequency in the magnetic field. The proton with spin $I = \frac{1}{2}$, mass m and charge e has its magnetic moment $\vec{\mu}$

$$\vec{\mu} = \eta \vec{I} = g_\eta \Big(\frac{e}{2mc}\Big)\vec{I} \tag{4.1}$$

where η is the proton gyro-magnetic ratio and g_η is the proton Landé g-factor, $g_\eta = 5.58$. For point-like particle, $g_\eta = 2$. When the proton is in an external magnetic field $\vec{B}$, its motion is described by the Hamiltonian $\mathcal{H}$

$$\mathcal{H} = -\vec{\mu} \cdot \vec{B} \tag{4.2}$$

The proton occupies two distinct eigenstates with spin projection along the magnetic field direction $I_z = \frac{1}{2}$ and $I_z = -\frac{1}{2}$. The energy splitting between these two eigenstates is

$$\Delta E = \hbar\omega_L, \qquad \omega_L = g_\eta\Big(\frac{eB}{2mc}\Big) \tag{4.3}$$

where ω_L is the proton *Larmor frequency* and $\hbar$ is the Plank constant. The proton magnetic moment $\vec{\mu}$ precesses about $\vec{B}$ at this frequency.

$$\frac{\mathrm{d}\vec{\mu}}{\mathrm{d}t} = \eta\vec{\mu} \times \vec{B} \tag{4.4}$$

This precession frequency can be measured precisely giving the magnetic field $\vec{B}$.

The magnetic moments $\vec{\mu}_i$ of protons in a sample add up to a static macroscopic magnetic moment $\overrightarrow{M}$,

$$\overrightarrow{M} = \sum_{i=1}^{N} \vec{\mu}_i \tag{4.5}$$

which is parallel and proportional to the applied field B. The time evolution of the expectation value $< \overrightarrow{M} >$ can be calculated using classical equations of motion since the value is a macroscopic quantity. In thermal equilibrium the magnetization $\overrightarrow{M}$ is aligned with respect to the external magnetic field to minimize the total energy.

To measure the field $\vec{B}$, another external magnetic field $\vec{B}_1$, which was circularly polarized at angular frequency ω and perpendicular to $\vec{B}$, was applied to the proton sample. The motion of $\overrightarrow{M}$ under the field $\vec{B} + \vec{B}_1$ is best described in a rotating coordinate system S^r which is rotating at angular velocity $\vec{\omega}$ about $\vec{B}$ [64],

$$\frac{\mathrm{d}\overrightarrow{M}}{\mathrm{d}t} = \eta\overrightarrow{M} \times (\vec{B}_r + \vec{B}_1), \tag{4.6}$$

$$\vec{B}_r = \vec{B} - \frac{\vec{\omega}}{\eta} \tag{4.7}$$

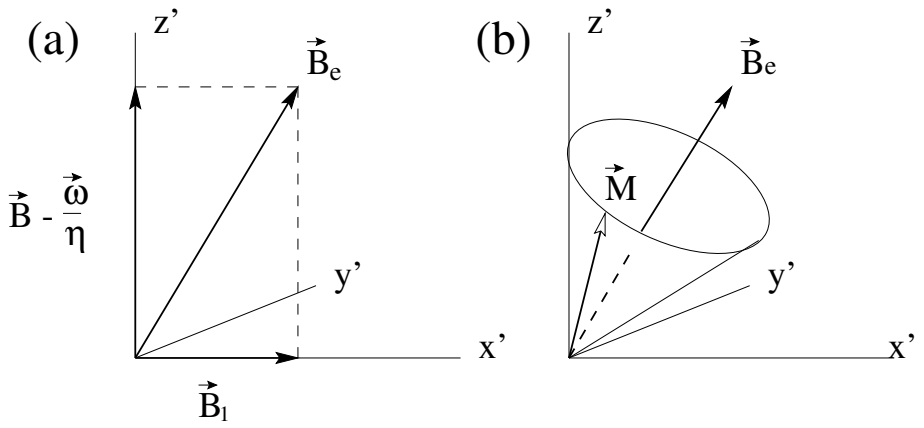

Figure 4.1: (a) Effective magnetic field in the rotating frame S^r. (b) Precession of the magnetic moment $\vec{M}$ in effective magnetic field.

The magnetic moment $\vec{M}$ rotates in the S^r frame about an effective magnetic field $\vec{B}_e = \vec{B}_r + \vec{B}_1$ (see Fig. 4.1). In the resonance case $\omega = \omega_L = \eta B$, the z' component of $\vec{B}_e$ vanished and $\vec{M}$ rotated about the x'-axis with frequency ω_L. If the external field $\vec{B}_1$ is switched on only for a finite time interval t, $\vec{M}$ is rotated by an angle,

$$\alpha = \omega_L \, t. \tag{4.8}$$

For a pulse duration time $t = \pi/(2\omega_L)$, the magnetization $\vec{M}$ is tilted 90° and turned to along the y' direction. In the laboratory frame, $\vec{M}$ then precesses with frequency $\omega = \omega_L$ around the static magnetic field $\vec{B}$. The magnetization precession induces a voltage signal in a coil. This voltage is refereed to as the NMR signal.

After $\vec{B}_1$ is switched off, the magnetization decays back to its thermal equilibrium value due to thermal transitions. For proton magnetization in a pure water sample, the characteristic relaxation time T_r was about ~ 3 seconds, which corresponded to a FWHM resolution $\Delta\omega$ of $2\pi \times 0.1$ Hz [65]. In a field of 1.45 T, $\omega_L = 2\pi \times 61.7$ MHz, and therefore the pulsed NMR measurement could reach up to 2×10^{-9} (0.002 ppm) accuracy. About 1 ms long NMR signal was sufficient to achieve the required 0.05 ppm accuracy in (g-2) experiment.

Fig. 4.2 shows a block diagram of the pulsed NMR magnetometer module used in (g-2) experiment. Each module served up to 20 NMR probes through the multiplexer. The nuclear spins of the water sample in the probe were excited by a Radio Frequency (FR) pulse applied to the resonance circuit formed by an inductance coil L_s and a capacitance C_s. The magnetization of the proton in a water sample was tilted by 90° by the linear polarized RF-field B_1 of about 2 mT in the coil L_s. The RF-pulse was switched off after about 10 μs. The NMR signal from the precessing magnetization was picked up by the same resonance circuit L_sC_s and transmitted by a duplexer to the input of a low noise preamplifier. The

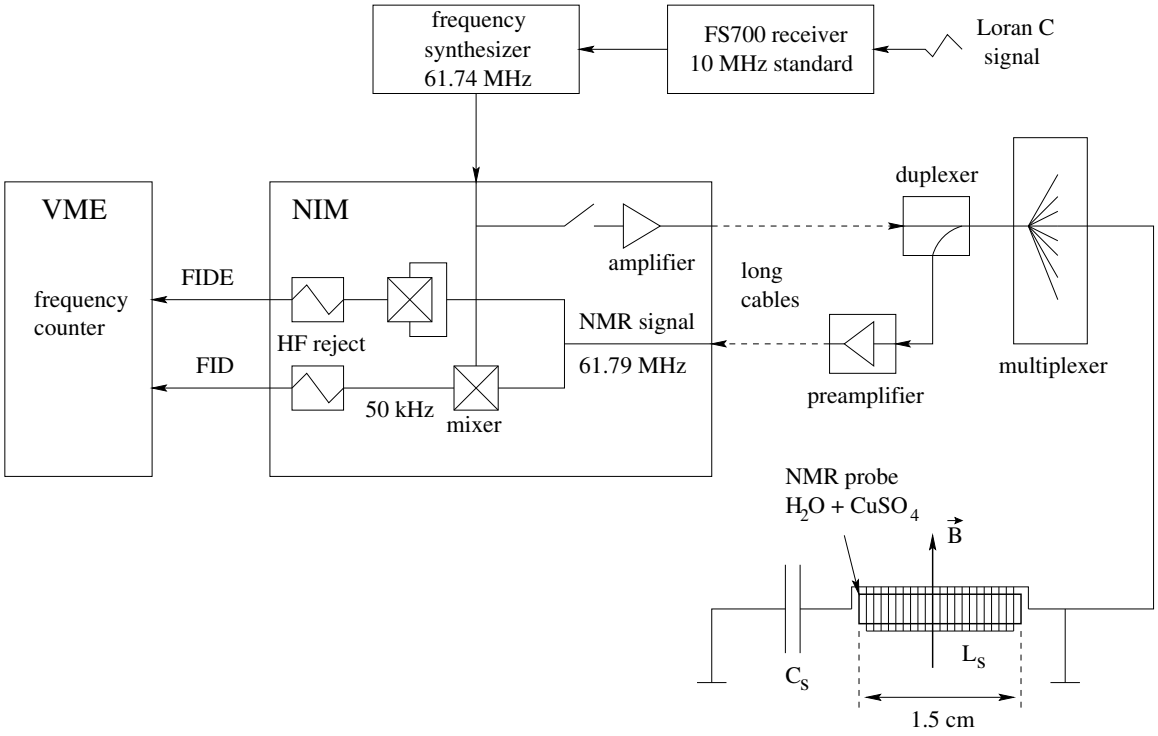

Figure 4.2: The diagram of the pulsed NMR magnetometer. The resonant circuit formed by the inductance L_s and the capacitance C_s is used to both excite the NMR probe and to pick up the Larmor precession signal. (Reproduced from reference [61])

NMR signals with frequency of $f_p \approx 61.79$ MHz were mixed with a reference signal, which normally had a frequency of $f_{\text{ref}} = 61\ 740\ 000$ Hz, to obtain beat signals with a frequency $f_p - f_{\text{ref}}$. The corresponding magnetic field to f_{ref} was $B_{\text{ref}} \approx 1.45\ T$. The beat signal,

referred to as a *free induction decay* (FID) signal with frequency $f_{\rm FID} \approx 50$ kHz, was measured directly with a frequency counter by counting the zero crossings within a time interval. For convenience, the magnetic field in this experiment was defined relative to $B_{\rm ref}$ as follows

$$B = \frac{B_{\rm real} - B_{\rm ref}}{B_{\rm ref}} = \frac{f_{\rm FID}}{61.74{\rm MHz}}, \tag{4.9}$$

where $B_{\rm real}$ was the value of the magnetic field.

4.2 Magnetic Field Measurement

The magnetic field measurement system in BNL (g-2) experiment consisted of two parts. One was the trolley, a vacuum-tight vessel with cylindrical shape housed 17 NMR probes and its calibration devices. The other was a system with 378 NMR probes embedded in the outer side of the vacuum chamber wall above and below the beam storage region.

4.2.1 Azimuthal Field Measurement with Trolley Probes

Between data runs, the magnetic field in the muon storage region was mapped twice a week, using 17 NMR probes housed within a cylindrical aluminum trolley. The trolley rode on the rails in the vacuum chamber (see Sec. 3.3.2) and was pulled by two cables which were also used to send and receive the signals from the trolley. The cables were wound on a drum with a potentiometer whose measurement gave the cable length and hence the azimuthal position of the trolley. The trolley position was calibrated with respect to 36 selected fixed probes on the vacuum wall, whose exact positions were known. An error of 0.1 ppm (See Table 4.1) was assigned to the field averaged over the azimuth due to the trolley position uncertainty in 2000. The trolley position measurement in 2001 was improved by using an encoding system the uncertainty was lowered to 0.05 ppm. Fig. 4.3 shows the relative position of the 17 NMR probes on a trolley.

The trolley probes were calibrated with respect to the plunging probe by comparing the measurements at the same position. Then they were calibrated with respect to a spherical

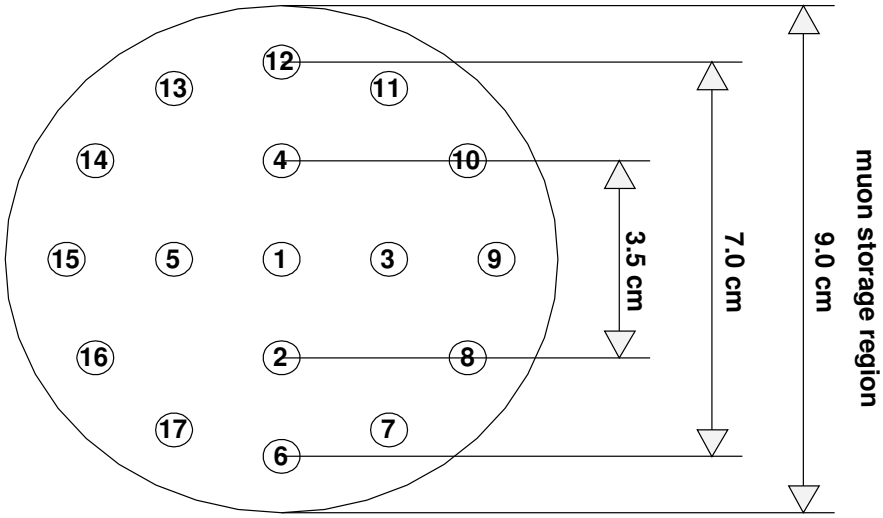

Figure 4.3: Position of the 17 NMR probes on the trolley. (Reproduced From reference [63])

water standard probe which had an uncertainty of 0.034 ppm. The total uncertainty on the dipole field from the calibration was taken to be 0.15 ppm in 2000 and 0.09 ppm mainly due to the position uncertainties between the plunging probe and trolley probes.

Each trolley measurement consisted of 150,000 readings (<1 cm per step) covering the whole 360° in azimuth. Each NMR reading had a statistical precision of about 0.05 ppm. After averaging over azimuth, the statistical uncertainty for a particular probe was negligible. The averaged field was expanded into two dimensional multi-poles,

$$B(x,y) = B(r,\theta) = B_0 + \sum_{n=1}^{\infty} a_n \left(\frac{r}{r_0}\right)^n \cos(n\theta) + \sum_{n=1}^{\infty} b_n \left(\frac{r}{r_0}\right)^n \sin(n\theta), \tag{4.10}$$

where x and y are the radial and vertical direction, and (r,θ) are polar coordinates with the origin at the center of the storage region. The coefficients a_n are the normal multi-poles, and b_n the skew multi-poles. The 17 trolley probe measurements were used to determine the dipole moment B_0 and other multi-poles a_n and b_n. A 0.5 ppm contour plot and the multi-poles of the azimuthal average of the field measured from one trolley run are shown in Fig. 4.4 for both 2000 and 2001 to demonstrate that the field was uniform to 2 ppm.

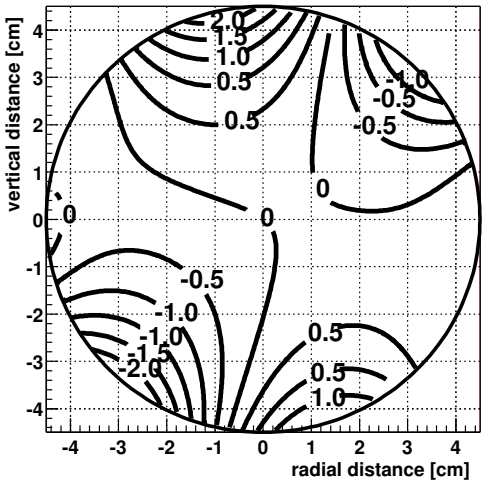

(a) 2000

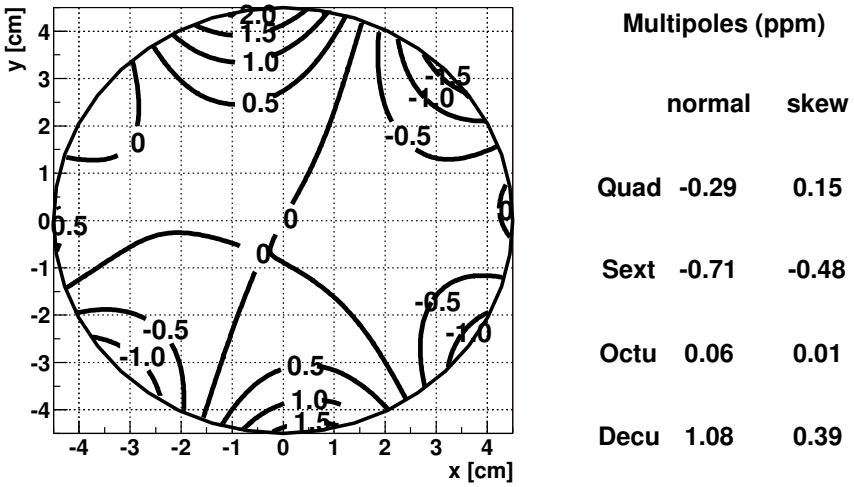

(b) 2001

Figure 4.4: The 2-dimensional multipole expansion of the magnetic field averaged over azimuthal. The zero ppm matches to the azimuthal average field $B_0 = 1.451\ 274$ T in 2000, and $B_0 = 1.451\ 269$ T in 2001 at the center of the storage region. The coefficients for order n=2-5 at edge of the storage region are listed.

The trolley probes measured the magnetic field in the muon storage region extending to a radius of 3.5 cm. The magnetic field beyond 3.5 cm radius was obtained by extrapolating the measured moments up to and including the decupole terms.

4.2.2 Tracking of the Field with Fixed Probe

During data-taking periods, the field in the storage region was monitored by 378 NMR fixed probes which were embedded in the upper and lower walls of the vacuum chamber every 5° in azimuth. The structure and the magnetometer of the fixed NMR probes were the same as those of the trolley probes. The average magnetic field over the ring from the fixed probes was determined by a weighted average of the measurements from a set of selected fixed probes. In 2000 and 2001, two independent analyzes were conducted using distinct subsets of these fixed probes, and their results agreed within 0.03 ppm range. These fixed probes were calibrated by the trolley runs in the same magnet-on period. This calibration through interpolation was the main systematic uncertainty on the fixed probe measurement, and was at 0.10 ppm level (see Table 4.1).

To reduce magnetic field fluctuations, the average readings of 36 uniformly distributed fixed probes were maintained to 0.1 ppm by feedback to the main magnet power supply. The feedback was turned off during the trolley measurements since the presence of the trolley disturbed the local field seen by the fixed probe.

4.3 Final ω_p Value and its Systematic Errors

The magnetic field was weighted by the muon distribution (see Chapter 6) in the storage region. With an uncertainty of ± 2 mm in the beam vertical offset, and 2.3 ± 1 mm radial displacement from the storage center, the systematic uncertainty on the dipole magnetic field was 0.03 ppm.

The final average magnetic field averaged over the muon distribution across all runs expressed in terms of the proton precession frequency was $\langle f_p \rangle = 61.791\ 595(15)$ MHz [22]

for 2000 run and $\langle f_p \rangle$ = 61.791 400(11) MHz [23] for the 2001 run. Table 4.1 summarizes the major systematic uncertainties in the magnetic field measurement. The final total uncertainties of 0.24 ppm (2000) and 0.17 ppm (2001) were at the same level as those of the spin precession frequency measurement. The magnetic field measurement uncertainties were negligible compared to the statistical and systematic uncertainties in the lifetime measurement.

Year	2000	2001
Source of errors	Size [ppm]	Size [ppm]
Absolute calibration of standard probe	0.05	0.05
Calibration of trolley probes	0.15	0.09
Trolley measurements of B_0	0.10	0.05
Interpolation with fixed probes	0.10	0.07
Uncertainty from muon distribution	0.03	0.03
Others	0.10	0.10
Total Systematic Error on $\langle \omega_p \rangle$	0.24	0.17

Table 4.1: Systematic uncertainties for the magnetic field analysis of both the 2000 and 2001 data. The "Others" includes higher multipoles, trolley temperature and power supply voltage response, eddy currents from the kickers, time-varying stray fields.

Chapter 5

Data Preparation for the Lifetime Analysis

5.1 Data Selection

The raw data from the various WFD/FSD/PSD electronics were reprocessed to reconstruct the decay electron energy and time information via pulse-fitting of the digitized traces. There were two slightly different pulse fitting algorithms [66, 67] used in two different analysis frameworks: *G2Too* using *ROOT* [68] and *G2OFF* using *PAW* [69], respectively, to make the data production. The G2OFF, which was written in FORTRAN, fitted the pulse and extracted event energy and time from the peak amplitude and peak central time. G2Too, which was written in the C++ programming language, extracted the event energy from the integrated pulse area and assigned the weighted center of the pulse to be the event time. This analysis used data from the *G2Too* production.

In the experiment, data were separated into runs lasting normally $\sim$ 1 hour in data taking time. Division of the data into these *runs* facilitated the storage, distribution, and eventually, the analysis of the data. The run number went from 6001 to 8873 in the 2000 run, and from 9000 to 11387 in 2001. These runs underwent a run-by-run and a fill-by-fill based

data selection process. All runs used in this analysis were chosen based on an internal run selection performed on the *G2Too* produced data. To be included in this list, a particular run must have had, among other criteria, no obvious problems written in the logbook, a T0 pulse for at least one fill, a certain minimum number of counts from all calorimeters, an acceptable normalization of counts across detectors, and the presence of quadrupole traces with no excessive sparking. A statistical comparison to a random selection of 'good' runs was made in order to eliminate isolated runs with significant differences of the calorimeter energy and time spectra. Lastly, the run must also have had analyzable magnetic field data for the field analysis.

Besides the run selection, fill selection criteria were also applied to the *G2Too* production. For example, a fill was excluded if the quadrupole sparked (spontaneous electric discharge), or the quadrupole trace was not read out or was too short in duration. A fill was discarded if the T0 signal was too small or not read out at all. A fill was removed if there was more than one fitted T0 event from the fitter. All runs which contained laser calibration pulses were also excluded. Calorimeter station 20 was excluded from the data analysis for both 2000 and 2001 runs, because it was located immediately downstream of the traceback chambers. This caused multiple scattering of the electrons and a subsequent energy distribution which was very different compared with other detectors. Detector station 2 was excluded in 2000 run because of a problem with the WFD which led to a distorted average pulse shape and consequent problems with the pulse fitting. That WFD module was replaced in 2001, and data from station 2 was used in the analysis.

There were a total of 1188 runs from *G2Too* production which were finally used in 2000 data analysis. A total of 979 runs were selected and analyzed for 2001 run data.

5.2 Energy Calibration

The decay electrons from the stored muons were detected by calorimeters. The integrated ADC counts of a pulse recorded in the WFD data were proportional to the amount of energy

deposited by a decay electron in a calorimeter. According to the *G2GEANT* simulation [51], the maximum energy on the simulated spectrum was equal to the maximum energy of the muon beam, 3.094 GeV. In the experiment, the energy spectrum also had a high energy tail from pileup events, giving a maximum energy greater than 3.094 GeV. A straight line fit on the linear part between 60% and 20% of the maximum of the electron spectrum returned the correct energy end-point, as illustrated in Fig. 5.1. The electron events on

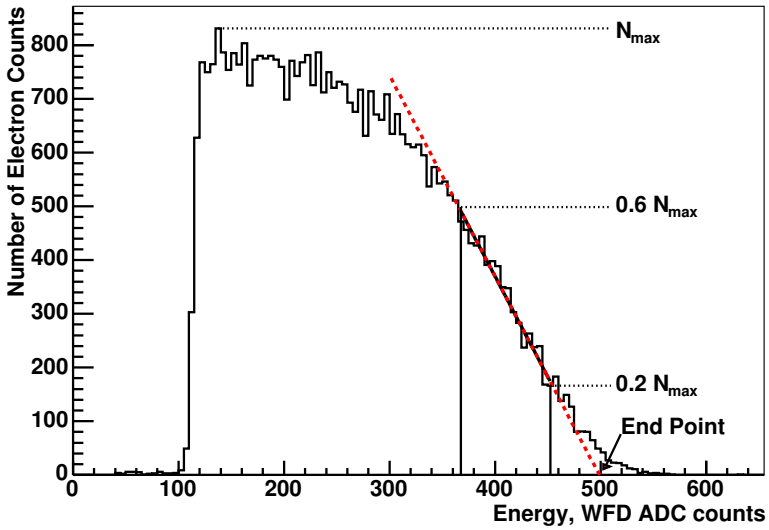

Figure 5.1: The electron energy spectrum of detector 23 in run number 10285. The electron events are between 200 μs and 600 μs after injection. A straight line fit to the linear part of the spectrum gives the energy end-point value, which is about 500 ADC counts.

this spectrum were between 200 μs and 600 μs after muon injection into the storage ring in order to ensure minimal contributions from pileup effects and gain changes which could distort the Michel spectrum. The end-points from the fitting fluctuated sharply between adjacent runs because of the statistics of the energy spectrum. A χ^2 cut on the linear fitting was applied to minimize the fluctuation.

The end-point of each run was calculated in the 2001 data, then the runs were grouped into small periods for each calorimeter based on its PMT high voltage adjustment history.

In each period, either a constant or a linear function was used to fit the end points, as shown in Fig. 5.2 for detector 23. The start and end run number for each group are shown on the plots, as well as the parameters. The end-points of other detectors were determined individually in the same way in each of available runs in 2001 data. Generally, the end points drifted down slowly with run number. A sudden change in the end-points occurred when there was an adjustment on the PMT high voltage. This parameterized run-by-run end point calibration had been used in the ω_a analysis for 2001 data.

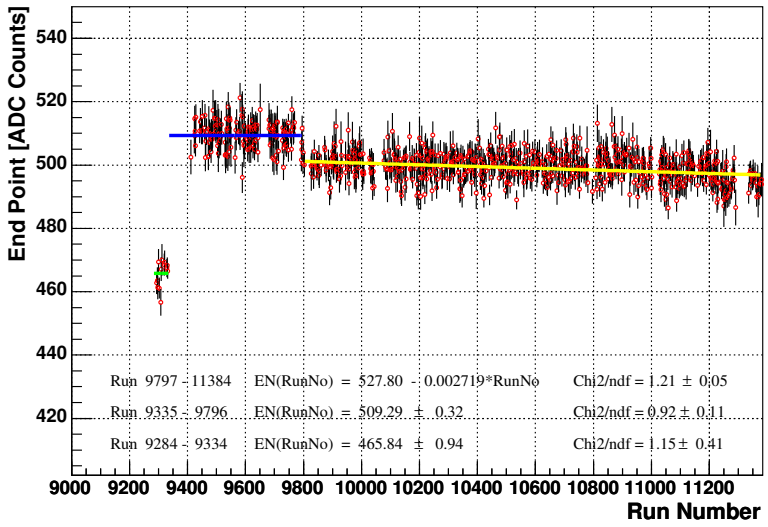

Figure 5.2: The parameterized end-point versus run number in 2001 data, detector 23. The same parameterized end-points are made for other detectors.

For the 2000 data, I adopted the end point calibration used by F. Gray [71] which was also run-by-run based calibration. In that scheme, the end point as a function of run number was averaged over discrete groups of runs during which the calibration was stable.

5.3 Gain Correction

The detector gain stability or energy scale change within a fill was caused by the non-uniform response of the calorimeter photomultiplier tubes. This was one of the most significant effects in the muon lifetime analysis. As described in Sec. 3.5.1, the photo-multipliers were gated off when the muons were injected into the storage ring accompanying a big flash. The gates were turned on after 15 μs for the detectors in the quiet second half of the ring, and much later for the side of the ring which suffered from the flash. Due to the slow rise-time of some tubes, the PMT gain depended on the electron arrival time at the calorimeter. The energy scale of the detected electron thus varied from early to late time within a fill. The time-dependent gain translated into a time-dependent variation in the average value of the electron energy. We used the average energy information to correct for this gain change in the following way.

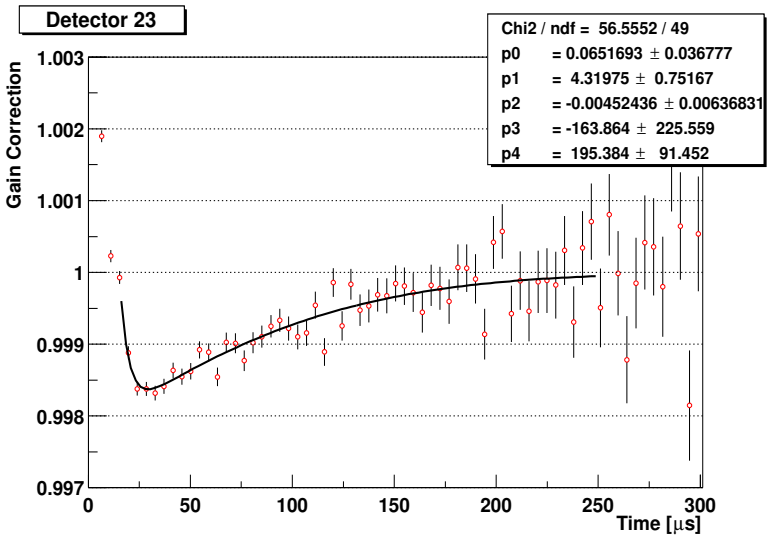

Figure 5.3: The gain correction of detector 23 as an example in 2001 data.

The average energy value was extracted for each (g-2) period, i.e. 4.3654 μs, in order to cancel the muon spin precession effect. In the half (g-2) period when muon spin and their

momentum were in the same direction, the average energy was high, and vise versa (see Sec. 2.2). The range to get the average energy was set to be from 2.0 GeV to 4.2 GeV on the Michel spectrum. The pileup events had been subtracted from the energy spectrum. Then, the gain correction is calculated from the average energy of each calorimeter by multiplying by a sensitivity factor, ~ 2.0. It was known that the gain change was negligible at late time. The gain was normalized by the average value between 200 μs and 400 μs to find the relative gain fluctuation. As an example, in Fig. 5.3, the open dots are the gain change of detector 23 in 2001 data. This change was fitted by the correction function (solid line on Fig. 5.3) Eq. 5.1.

$$g(t) = (1.0 + A \cdot e^{-t/B}) \cdot (1.0 + C \cdot e^{-(t-D)^2/E^2}) \tag{5.1}$$

where A, B, C, D and E are fitting parameters different for each detector. The fit started as early as possible for each detector, and ended at 250 μs. After 250 μs, the gain correction was negligible and $g(t)$ was equal to one. The electron energy $E(t)$ was corrected from the raw energy $E_{raw}(t)$ by

$$E(t) = \frac{E_{raw}(t)}{g(t)} \tag{5.2}$$

The function $g(t)$ had different parameters for different detectors. Overall, the gain shift

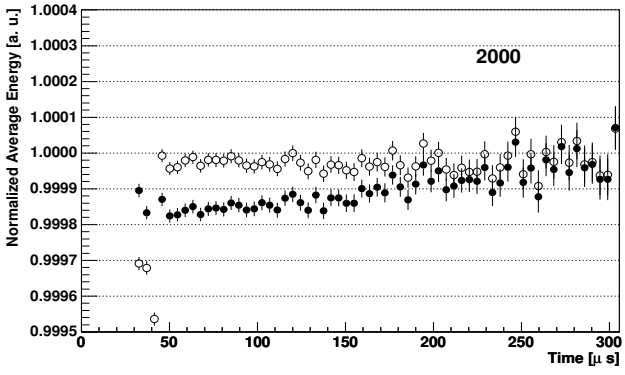

Figure 5.4: The average energy of the 2000 data for the sum of all detectors except detector 2 and 20. Close dots are before the gain correction, and open dots are after the gain correction.

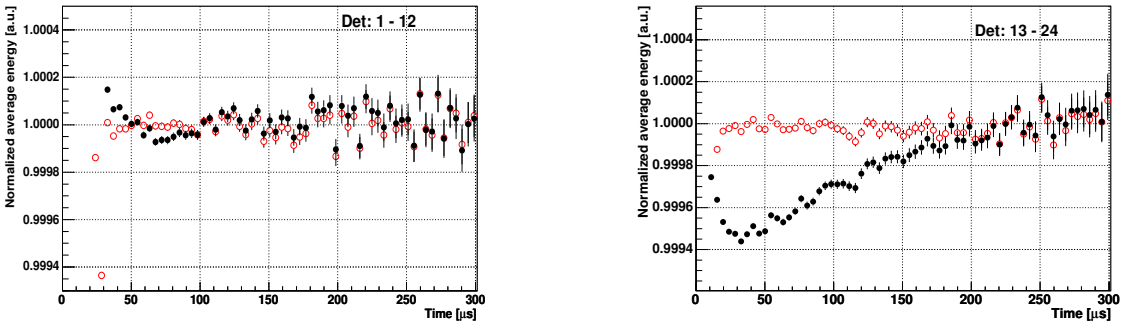

(a) (b)

Figure 5.5: The average energy as a function of time is flatter after the gain correction. The left is for the sum of the first half ring detectors, and the right is for the second half ring. The dots are the average energy before applying the gain correction, and the open circles are the average energy after applying the gain correction.

was smaller than 0.2% for all detectors after 50 μs. A systematic uncertainty in the muon dilated lifetime from any possible inaccuracy in this gain correction effect is discussed in Sec. 7.2.6. The same procedure was performed to correct the gain change in both 2000 and 2001 data. In Fig. 5.4 (2000) and Fig. 5.5 (2001), the normalized average energy was consistent with one after the gain correction.

5.4 Pileup Spectrum Construction

The way in which pulses overlap in time was understood from Monte Carlo simulation studies. For pulse separation times less than 3 ns, only a single pulse was reconstructed by the pulse fitter. Conversely, for separation times greater than 4 ns, two pulses were always found. In the region between 3 and 4 ns, pulses could be assigned incorrect times and energies. In fact, it was only for separations of at least 5 ns that the reconstructed times and energies of individual pulses could be deemed reliable. However, the energy-weighted average time and the sum of individual energies were treated consistently by the pulse

fitter, even in the troublesome region. From the simulation studies of pulse fitting, the reconstructed total energy was determined to be 0.94 of the true total energy in overlap cases. To simplify this situation, an artificial dead-time of 5 ns was applied when filling histograms even though double pulses separated by < 5 ns might be reconstructed. Whenever two pulses were found within this time interval, they were combined into a single pulse and the sum of the individual energies, weighted by the aforementioned scale factor of 0.94, was assigned to this single pulse. The energy-weighted average time was taken to be the time of the combined pileup event.

We made use of the long digitization islands characteristic of the WFDs to artificially construct a spectrum of pileup pulses. Any pulse whose amplitude exceeded the hardware threshold (between 0.9 GeV and 1.2 GeV depending on detector station) triggered the digitization of WFD. Around this *trigger pulse*, we located the so-called *shadow pulses* in the searching windows. In this analysis, the symmetric windows, i.e. one window before and one after the trigger pulse, were used to search for the shadow pulses. Typically, these windows were 10 ns away from the trigger pulse. Since the WFD always recorded at least 15 ns before and 25 ns after each trigger pulse, which gave a sufficient region for shadow pulse searching. Fig. 5.6 illustrates the pulse placements in this method.

For each trigger pulse S_1 of energy E_1 at time t_1, a pre-shadow pulse S_{pre} was sought at t_{pre} with energy E_{pre}, and/or a post-shadow pulse S_{post} pulse was sought t_{post} with energy E_{post} within the same digitization island. The searching window was set to $\pm\frac{T_r}{4}$ centered at $(t_1 - T)$ for pre-shadow pulse and $(t_1 + T)$ for the post-shadow pulse, respectively. T_r was the resolution time in the pulse fitting algorithm and T was the arbitrary dead time. For the *G2Too* production, $T_r = 5$ ns. Pulses S_{pre} and/or S_{post} were shifted back in time and combined to form a shadow pulse S_2 at time t_2 with energy E_2.

$$t_2 = \frac{(t_{pre} + T)E_{pre} + (t_{post} - T)E_{post}}{E_{pre} + E_{post}} \tag{5.3}$$

$$E_2 = E_{pre} + E_{post} \tag{5.4}$$

Then, the pulse S_2 was combined with S_1 to form a double pulse D having a time and

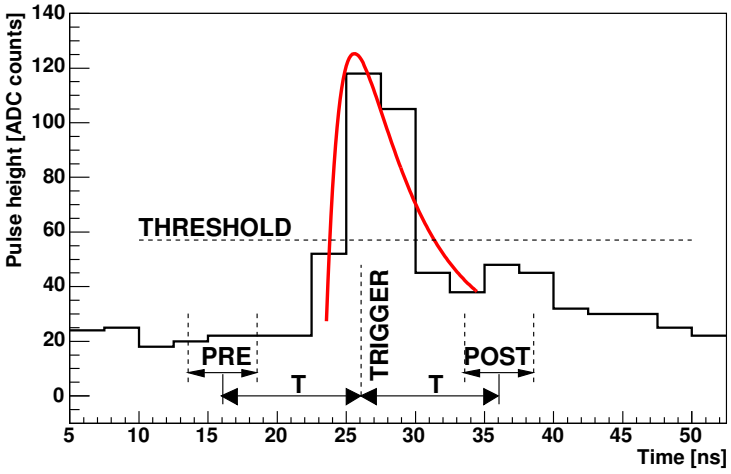

Figure 5.6: A cartoon drawing of the trigger and shadow pulses placement in symmetric window pileup construction method. The red smooth line is the fitted trigger pulse. The pre-shadow, labeled as "PRE", and post-shadow, labeled as "POST", searching windows are twice size of that in application.

energy given by

$$t_D = \frac{t_1 E_1 + t_2 E_2}{E_1 + E_2} \tag{5.5}$$

$$E_D = f(E_1 + E_2) \tag{5.6}$$

where, the coefficient $f = 0.94$ was the previously mentioned energy scale factor. Finally, the pileup spectrum $P = D - S_1 - S_2$ was formed and subtracted from the data.

In this analysis, the time shift T was chosen to be 10 ns. The probability of finding a shadow pulse before the trigger pulse was the same as that after the trigger pulse in a short time range. This time shift T could be any value greater than the resolution time T_r. In 2001 run, 10 detector stations, including 7, 8, 9, 12, 13, 14, 16, 18, 19 and 24, contained so-called "pre-shower" pulses. These pre-shower pulses were about 6 ns earlier than the trigger pulse. Figure 5.7 shows the "pre-shower" pulses on the flat distribution of the time distance between the trigger pulse and shadow pulse for the data from 100 μs to 600 μs.

The summed energy of pre-shower pulse and trigger pulse was less than 3.2 GeV. These pre-shower pulses were not in shadow pulse searching windows when we set the artificial dead time to be 10 ns, therefore they did not affect the constructed pileup events.

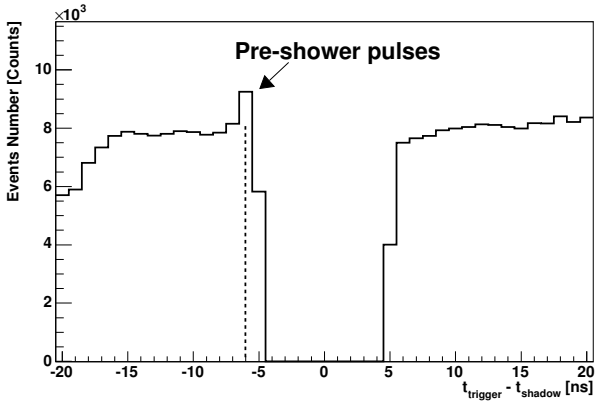

Figure 5.7: The distribution of the time distance between trigger pulse and shadow pulse is flat except the peak at -6 ns. The peak is from the so-called "pre-shower" pulses. The time distance is defined as $t_{trigger} - t_{shadow}$. The trigger pulse has energy greater than the WFD hardware threshold. And the shadow pulse can have any energy value.

This method also constructed the triple events when both pre-shadow and post-shadow pulses were present. The probability of having triple events was higher at the earlier time after the injection. Its effect on the dilated lifetime analysis was small.

This pileup technique had been shown to effectively remove pileup to at least the 90% level. The fraction of pileup that was inaccessible due to the higher hardware energy thresholds in 2000 data was less than 1% for most of detectors when the electron energy cut was chosen 2.0 GeV. In the 2001 run, the hardware threshold was lowered to around 0.9 GeV for most calorimeter stations. This made the pileup subtraction efficiency higher than that in 2000 when the electron energy cut was set to 1.8 GeV.

As Table 5.1 indicates, pileup subtraction with the designed energy cut adjusted the time spectrum for the dilated lifetime analysis and fast rotation analysis. In 2000 run, for positron energy cut $2.0 \leq E \leq 3.2$ GeV, the pileup subtraction recovered about 0.05% electrons from

lost single events, while in the 2001 run, for an electron energy cut of $1.8 \leq E \leq 3.2$ GeV, the pileup subtraction recovered 0.15% electron events. Study [51] had shown that the net event number integrating over pileup spectrum was negative for the event energy below about 2.6 GeV, and was positive for that above 2.6 GeV. When the energy cut range was even around 2.6 GeV, the pileup subtraction would only change the shape of the time spectrum, but not the electron counts. The pileup subtracted data set consisted of about 3.23 billion positrons in 2000 and 2.87 billion electrons in 2001 between 47.6 μs and 600 μs.

		M e^+					
2000	Sub Period	P1	P2	P3	P4	P5	Sum
	Before PUS	201.08	367.20	278.03	1681.21	701.54	3229.06
	D	0.87	3.55	2.13	12.90	4.98	24.43
	S_1	0.45	1.91	1.14	6.89	2.66	13.06
	S_2	0.45	1.91	1.14	6.89	2.66	13.06
	$P = D - S_1 - S_2$	-0.04	-0.27	-0.14	-0.90	-0.35	-1.69
	After PUS	201.12	367.46	278.17	1682.11	701.89	3230.75
	Sub Period	LB	LA	HB	HA	SO	Sum
2001	Before PUS	945.94	768.30	1055.45	96.10	67.84	2933.63
	D	3.44	2.88	4.25	0.39	0.28	11.24
	S_1	1.93	1.62	2.38	0.22	0.16	6.30
	S_2	1.93	1.62	2.38	0.22	0.16	6.30
	$P = D - S_1 - S_2$	-0.42	-0.35	-0.52	-0.05	-0.04	-1.38
	After PUS	946.36	768.65	1055.97	96.15	67.91	2935.03

Table 5.1: Number of electrons involved in pileup subtraction in 5 sub data sets in 2000 run with 47.6 μs $< t <$ 600 μs and $2.0 \leq E \leq 3.2$ GeV for the 2000 run. P1, P2, P3, P4 and P5 are the different data sets in 2000. LB, LA, HB, HA and SO are data sets in the 2001 run with the same time range and $1.8 \leq E \leq 3.2$ GeV for 2001 run.

5.5 Coherent Betatron Oscillation

The muons in the storage ring were focused by the main magnetic field horizontally and by electrostatic quadrupole field vertically. In the electrostatic field each individual muon

particle underwent harmonic oscillations known as betatron motion about its momentum-dependent central radius. The equation of motion is better derived if we set up the coordinate system such that $x = 0$ at the storage ring central orbit and $y = 0$ in the mid-plane of the storage ring. In the magnetic field $\vec{B} = B_0\hat{y}$ and electrostatic field $\vec{E} = \kappa x\hat{x} - \kappa y\hat{y}$, the net force applied on the muon particle is the Lorentz force $\vec{F} = q\vec{E} + q\vec{\beta} \times \vec{B}$, where $\kappa = \frac{\partial E_r}{\partial r}$ is the field strength of the field and $c = 1$ in the derivation. At the central orbit, $\frac{\gamma m v^2}{R_0} = e\beta B_0$. The equations of motion in the x and y directions for the muon are described as

$$\gamma m\ddot{x} + \frac{\gamma m v^2}{R_0^2}(1-n)x = 0 \tag{5.7}$$

$$\gamma m\ddot{y} + \kappa e y = 0 \tag{5.8}$$

where the field index $n = \frac{\kappa R_0}{\beta B_0}$. The solutions of the equations give the betatron oscillations of the muon about its central orbit,

$$\begin{aligned} x &= A_x \cos(2\pi f_x t + \phi_x) \\ y &= A_y \cos(2\pi f_y t + \phi_y) \end{aligned} \tag{5.9}$$

The muon oscillates in the horizontal direction with frequency $f_x = f_c\sqrt{1-n}$, and in the vertical direction with frequency $f_y = f_c\sqrt{n}$. The muon cyclotron frequency is $1/f_c = 2\pi R_0/v$.

The solutions in Eqs. 5.9 assumed that the electrostatic field was continuous along azimuthal. In the g-2 storage ring, since the quadrupole electrodes covered 43% of the ring circumference with a four-fold symmetry of the placement, there was a more sophisticated treatment. However, Eqs. 5.9 still hold after multiplying by a beta-function which are approximately constant [46, 47].

In the macroscopic view, the entire muon population in the storage ring also coherently oscillated with the betatron frequencies. However, any individual detector located at a fixed azimuthal position observed this "Coherent Betatron Oscillation" (CBO) with frequencies

which were at the beat frequency f_{CBO} of the cyclotron and the betatron oscillation frequencies. In the radial direction, $f_{CBO} = f_c - f_x = (1 - \sqrt{1-n})f_c$, and in the vertical direction $f_{VCBO} = f_c - f_y = (1 - \sqrt{n})f_c$. f_{CBO} and f_{VCBO} were the apparent frequencies that we observed in the decay electron data from any individual detector. The field index was $n \approx 0.135$ with some small adjustments throughout the run in 2000. In 2001, we ran at two distinct values: $n = 0.122$ and $n = 0.142$. The radial CBO frequencies are listed in Tables 5.2.

	Set	runs	CBO Frequency f_{CBO} (kHz)	CBO lifetime $\tau_{CBO}(\mu s)$	Comments
2000	P1	6369 - 6621	474.1	125.5	
	P2	6712 - 7151	468.3	87.9	
	P3	7226 - 7445	465.3	146.6	
	P4	7446 - 8350	465.3	146.6	Hardware Threshold Change
	P5	8351 - 8821	466.8	116.7	Radial Field Change
2001	LB	9000 - 9754 9992 - 10272 10713 - 10788	419	94	
	HB	9756 - 9989 10274 - 10710	490	114	
	LA	10789 - 10960 11267 - 11354	419	94	Radial Field Change
	HA	10962 - 11009 11357 - 11384	490	114	
	SO	11299 - 11324	419	94	Scraping off

Table 5.2: Sub data set definitions for the 2000 data and 2001 data. There was only one radial CBO frequency with some small variations in 2000. In 2001 run, the period LB stands for (L)ow quads voltage (B)efore radial field changing. LA is for (L)ow voltage (A)fter radial field changing. HB is for (H)igh voltage (B)efore changing. And HA is for (H)igh voltage (A)fter radial field changing. SO is for Scraping Off data set.

The radial CBO was especially important in the analysis, since the calorimeter acceptance depended on the radial position of the muon. The beam center oscillation caused a modulation of the electron counting rate at the level of a few percent. The amplitude of

the coherent betatron oscillation decreased throughout the fill due to the spreading of the muons or beam debunching. The run lists in year 2000 and 2001 data were divided into several subsets based on the apparent CBO frequency and radial magnetic field adjustment. This data separation is defined in Table 5.2 for 2000 and 2001 data, respectively. There were five sub data sets in 2000. In 2001 data, all runs were separated to nine sub periods, then combined into four big chunks according to the radial magnetic field change.

Each data sets in the above table had their own CBO frequency which was determined by the quadrupole high voltage setting during the data taking period. The CBO frequency was obtained from a Fourier transform of the residue spectrum, i.e. data spectrum subtracted by a 5-parameter fitting function $N(t) = Ne^{-t/\gamma\tau}[1 + A\cos(\omega_a t + \phi)]$. The radial magnetic field adjustments during the run were chosen in order to move the muon beam center in the vacuum chamber to reduce the muon losses.

5.6 Construction of Muon Losses

Most of the muons in the (g-2) storage ring decayed into electrons which were recorded by the calorimeters. A small fraction of the muons disappeared from the stored muon population before they decayed. For example, the muon could hit the collimators or kicker plates during its betatron oscillation motion, and lost a small amount of energy. This would cause it to move to a smaller cyclotron orbit, collide with more materials on its path, losing energy until it bent inward into the ring and was lost from the stored muon population. This is called *muon loss*. There was no decay electron recorded for this event. The muons on the outer edges of phase space were more likely to interact with the materials, therefore they were more likely to be lost. In the (g-2) experiment, the beam scraping procedure was designed to force muon losses at early times after injection. After scraping was done, the stored muons occupied a smaller phase space than the storage aperture, and were less likely to be lost, thus insuring that the exponential decay spectra accurately portrayed muon lifetime.

Unlike the previous CERN experiment, there was no dedicated muon loss detector in BNL (g-2) experiment. Instead, the lost muons were constructed by relating them to the three-fold coincidences in consecutive FSDs and calorimeter detectors. Fig. 5.8 illustrates the different paths of electrons and lost muons. The decay electrons produced electromagnetic showers in the calorimeter and were stopped in the first calorimeter detector which they hit. In contrast, high energy muons ($\sim$ 3.0 GeV), which were minimum-ionizing particles (MIPs), deposited $\sim$ 200 MeV in the calorimeter block. The signal amplitude from this small energy deposition was much lower than the hardware threshold, and it was even smaller than the pulse-fitter software threshold in many cases. Therefore, the lost muons could pass several calorimeter detectors in a row. However, both electrons and muons produced a big signal in the FSD and PSD scintillating tiles when they passed through.

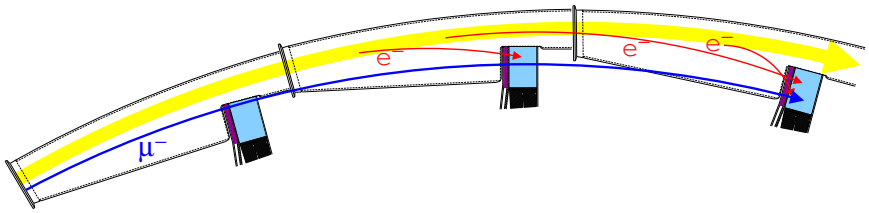

Figure 5.8: A three-fold coincidence between the consecutive FSDs and calorimeter detectors. Reproduced from reference [70].

Based on the distinguishable behavior of the lost muons in the detectors, we constructed the three-fold coincidence $L(t)$ in the consecutive FSDs and calorimeters [70]. A successful lost muon candidate must leave signals in three consecutive FSDs, but deposit zero or small energy (less than the hardware threshold) in three associated calorimeters. Because muon loss events were quite rare compared to the decay electrons, any accidental coincidences could form a background event, for example, a low energy electron hitting the first FSD with pre-showering from a second electron which triggered the second and third FSDs. For this reason, random coincidences were constructed and subtracted from the triple events.

The muon losses were the constructed triples after random subtraction and after applying corrections for *discriminator deadtime* and *accidental calorimeter veto*. The discriminator deadtime correction was necessary because once the FSD discriminator fired on an event, it could not respond to another event in a certain deadtime. This deadtime was 12 ns in the 2001 run, and was $\sim$ 30 ns in 2000 run. The accidental calorimeter correction was done in a similar way as the deadtime correction.

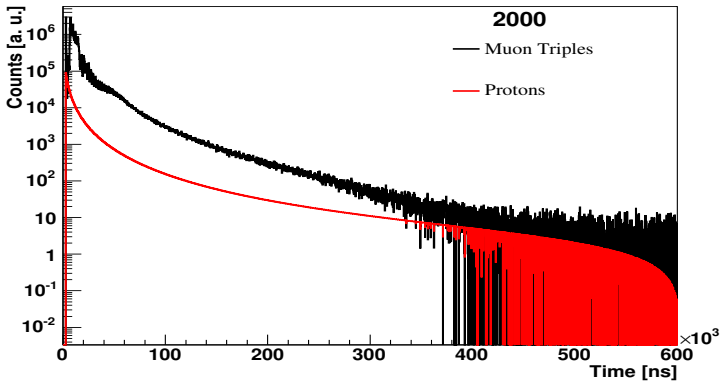

Figure 5.9: The triple coincidence time spectra recorded by FSDs in the 2000 run. The dark line (top) is the reconstructed lost muons, and the light/red line (bottom) is the constructed lost protons.

The time spectrum of FSD triple coincidences after corrections for the 2000 run is shown in Fig. 5.9, summed over all runs, and the triple coincidence spectra for 2 separate sets in the 2001 run are shown in Fig. 5.10.

For the 2000 (μ^+) run, there was a significant background in the triple coincidences in FSDs which came from the losses of the stored protons in the ring. It had been estimated from a Čerenkov counter study that nearly 10% of the particles injected into the storage ring were protons in the 2000 (μ^+) run along with equal portion of μ^+, π^+ and e^+. Since the protons were stable, they did not distort the decay positron time spectrum. But they could be lost in the same way that the muons did, thus skewing the lost muon spectrum. However, the protons behaved very differently in the calorimeter. They left a small amount

of energy in the first two calorimeters, and more energy (more than 1 GeV) in the third calorimeter. This had been verified by the three-fold coincidence signals when the electrostatic quadruples were turned off (around 1.0 ms after injection). The energy distribution for these events was consistent with what one would expect from proton-induced hadronic showers. Based on this, an upper limit for the fraction of lost three-fold coincidence protons was made, and plotted on Fig. 5.9 as the light (red in color) line.

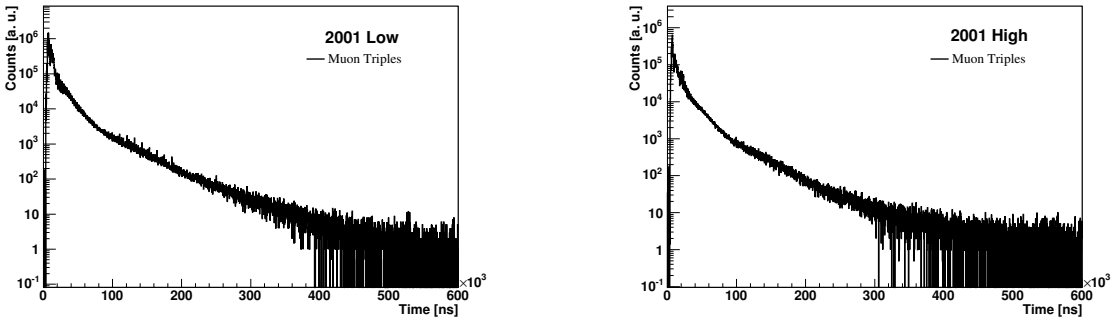

(a) Muon Loss in LB and LA Data Set

(b) Muon Loss in HB and HA Data Set

Figure 5.10: Muon triple events in the 2001 run. (a) is for quadruples high voltage 21.7 kV. (b) is for quadruples high voltage 25.3 kV.

The number of constructed triple coincidence events depended strongly on the experimental running condition. The extreme case was the scraping off data set in 2001 run. About seven times more triple coincidences were reconstructed in the scraping off data set compared to that in normal data sets indicating that scraping succeeded in reducing subsequent muon loss. Figs. 5.11 and 5.12 show the ratio between the reconstructed triple coincidence and the electron events as a function of time for the 2000 and 2001 data in different data subsets. The triples were from the sum of all possible FSD combinations. The electrons were those whose energies were above the hardware threshold in the first calorimeter of the three consecutive detector stations. On the figure, each point could be interpreted as the nominal differential muon loss rate during 12 μs (about three (g-2) periods).

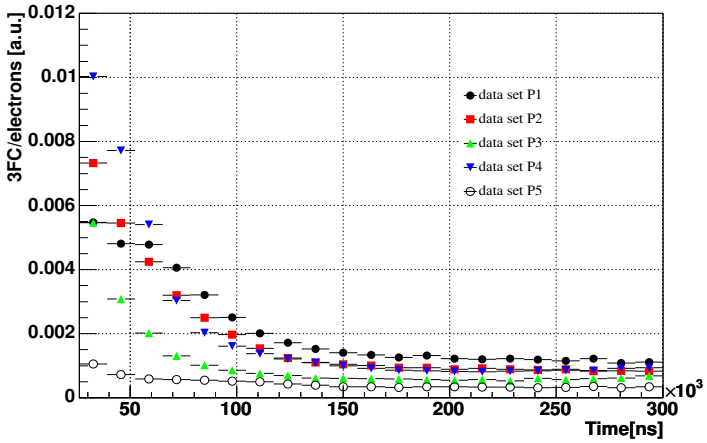

Figure 5.11: The ratio between the constructed triple coincidence and the positron as a function of time in 2000 run. The dark close circle is P1, red square is P2, green up triangle is P3, blue down triangle is P4 and open circle is P5 data set.

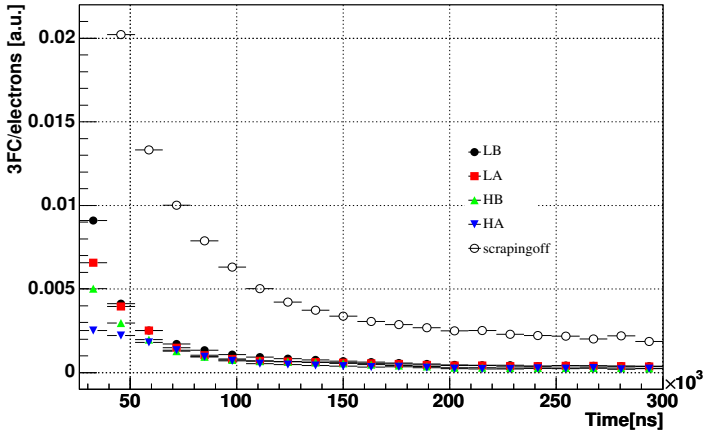

Figure 5.12: The ratio between the constructed triple coincidence and the electron as a function of time in the 2001 run. The dark close circle is LB, red square is LA, green up triangle is HB, blue down triangle is HA and open circle is scraping off data set.

The large differential loss of the scraping off data set is clearly shown on Fig. 5.12. Since the absolute detection efficiency of the lost muon cannot be determined exactly, we could only compare the overall trending over time in a fill. Fig. 5.11 shows the similar differential loss plots for five data sets in 2000 run. According to the experimental record, data set P3 and P4 were under the same running condition except that the hardware threshold on calorimeter stations 3, 4, 5 and 6 were increased in order to balance the event rates on different VME crates. Because there were no FSDs on these detector stations, this adjustment should not affect the detection of the triple coincident at all, yet there was a discrepancy between the differential losses in P3 (upward triangle) and P4 (downward triangle).

As described in Appendix B, it was the integrated muon loss function form which was used in the final fitting function. The effect of muon loss on the dilated lifetime is discussed in Sec. 7.2.

Chapter 6

Fast Rotation Analysis

6.1 Data Preparation for Fast Rotation Analysis

The data in the fast rotation analysis were matched with those in the dilated lifetime analysis by sub data sets accordingly, see Sec. 5.5. The electron energy cuts were 2.0 GeV $\leq E \leq$ 3.2 GeV in the 2000 data, and 1.8 GeV $\leq E \leq$ 3.2 GeV in the 2001 data. They were the same as those in the dilated lifetime analysis. The gain correction was applied as well.

A *pure fast rotation* spectrum $F(t)$ was created by dividing out the (g-2) spectrum (*randomized by fast rotation period*) $G(t)$ from the *actual signal* spectrum $S(t)$. The statistical errors on the time spectra were propagated, and the spectra of all available detectors were combined.

6.1.1 Pure Fast Rotation Spectrum

The muon particles were injected into the muon storage ring in bunches. The RMS width of each bunch was about 28 ns in 2001 run, while in 2000, the beam bunch width varied from 18 ns to 28 ns. This width was shorter than the cyclotron period of the bunch in the ring. Any particular calorimeter detected the decay electrons only when the bunch passed by. Therefore, the electron time spectrum appeared as a discrete pattern at early times.

This "fast rotation" spectrum is shown in Fig. 6.1 for detector station 23 in 2001 run where the discrete pattern is clearly visible. Let us label the observed decay electron spectrum as $S(t)$, and call it the *actual signal*, which contained all physical effects, including fast rotation, exponential decay, (g-2) modulation, CBO, etc. The time bin width was set to be 5 ns on the plot.

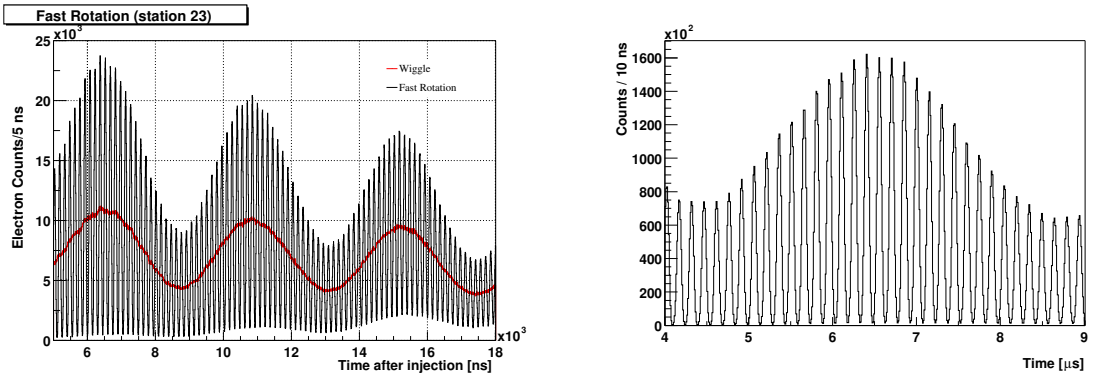

(a) (b)

Figure 6.1: The black spectrum is the actual observed electron signal $S(t)$ with time bin width 5 ns. The smooth line is the spectrum randomized by the cyclotron period with exactly the same data as in $S(t)$. The spectrum of detector 23 in LB data set of 2001 run is plotted.

The fast rotation structure could be isolated if we divided out by a function $G(t)$ which excluded only the fast rotation frequency. A naive example of $G(t)$ was the so-called 5-parameter function 6.1 describing the g-2 wiggle.

$$G(t) = Ne^{-t/\gamma\tau}[1 + A\cos(\omega_a t + \phi)] \tag{6.1}$$

However this function did not include other effects, such as CBO. The best way to ensure that all such effects were properly included in $G(t)$ was to use the data itself by randomizing away the short frequency component. An example of the randomized spectrum is shown superposed on the fast rotation structure in Fig. 6.1 (a), where the randomization interval

was the estimated cyclotron period 149.185 ns.

The *pure fast rotation spectrum*, $F(t)$, was defined as the ratio of the *actual signal* $S(t)$ to the *randomized function* $G(t)$,

$$F(t) = \frac{S(t)}{G(t)} \tag{6.2}$$

Fig. 6.2 (a) shows the pure fast rotation time spectrum $F(t)$ in a wide time range. As stated in reference [73], the advantage of using pure fast rotation signal $F(t)$ was that both decay exponential $e^{-t/\tau}$ and the g-2 frequency ω_a were obviously excluded. Since the $G(t)$ function was a fill randomized version of $S(t)$, i.e. normal g-2 wiggle spectrum with 5 ns time bin width, other kinds of multiplication effects, such as CBO, were reduced greatly as well. In order to make the *randomized spectrum* $G(t)$ as smooth as possible, ten (10) random seeds were used, and the spectra were averaged.

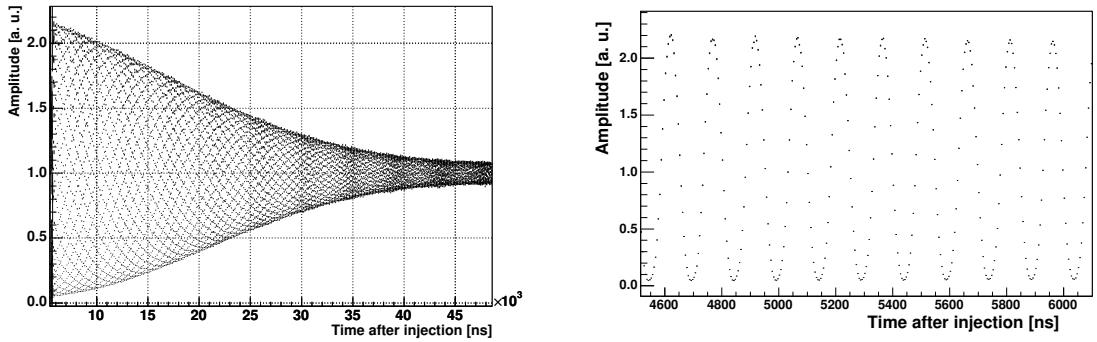

(a) (b)

Figure 6.2: The pure fast rotation spectrum $F(t)$ for detector 23 of LB sub-run-period in the 2001 data. (a) is in the wide time range. (b) is the zoomed in version.

The statistical uncertainty $\sigma_{F(t)}$ on the spectrum $F(t)$ was propagated from the uncertainty $\sigma_{S(t)}$ of $S(t)$ and $\sigma_{G(t)}$ of $G(t)$,

$$\sigma^2_{F(t)} = \frac{S(t)^2}{G(t)^2}\left(\frac{\sigma^2_{S(t)}}{S(t)^2} + \frac{\sigma^2_{G(t)}}{G(t)^2} - 2\frac{\sigma^2_{S(t)G(t)}}{S(t)G(t)}\right) \tag{6.3}$$

Both $S(t)$ and $G(t)$ were the counting histograms. The error on each time bin was approximated by a Gaussian distribution. The standard deviation $\sigma^2_{S(t)} = S(t)$ at time t, and $\sigma^2_{G(t)} = G(t)$. Let us neglect the 3% data overlap between $S(t)$ and $G(t)$ at any time bin, and assume that $S(t)$ and $G(t)$ were uncorrelated. In this case, we over-estimated the uncertainty on $F(t)$, and assigned a upper limit $\sigma_{F(t)}$ as in Eq. 6.4 to $F(t)$ at each time bin. The uncertainty on $F(t)$ was no longer a Gaussian distribution.

$$\sigma_{F(t)} = \frac{\sigma_{S(t)}}{G(t)}\sqrt{1 + \frac{S(t)}{G(t)}} \tag{6.4}$$

6.1.2 Combining Detectors for the Pure Fast Rotation Spectrum

When the time spectra $S(t)$ and $G(t)$ for 24 detectors were built, they were aligned according to the (g-2) phase of each detector in the muon storage ring. To create the sum of the pure fast rotation spectrum $F(t)$ coherently from individual detectors, the histogram $F(t)$ for each detector had to be shifted according to the fast rotation phase.

The histogram of the i^{th} detector in the storage ring was shifted by n bin to match the phase of the first detector.

$$n = \bar{\tau}_c/24 \times (i-1)/w \tag{6.5}$$

where $\bar{\tau}_c$ was chosen to be 149.182 ns and w was the time bin width. The content at time t on the summed histogram was calculated by the weighted data from individual detectors.

$$F_{sum}(t) = \frac{\sum_{i=d1}^{d2}(F_i(t)/{\sigma_i}^2(t))}{\sum_{i=d1}^{d2}(1/{\sigma_i}^2(t))} \tag{6.6}$$

$${\sigma_{sum}}^2(t) = \frac{1}{\sum_{i=d1}^{d2}(1/{\sigma_i}^2(t))} \tag{6.7}$$

where $d1$ and $d2$ were the desired start and end detector number in the ring.

In this analysis, the bin width w was 5 ns for most cases. Therefore n was not exactly an integer. The histogram for a particular detector could be shifted too early or too late. As a comparison, another set of histograms were made with $149.182/48 = 3.108$ ns time bin width. The time difference for two consecutive detectors was 2 time bins wide. For the

two different bin-width histograms, the χ^2 of the individual fast rotation peak fittings on the summed histograms were almost the same. Although the linear fittings on the peak position versus peak number in the two cases had slightly different χ^2, the average fast rotation period versus time plots (see Fig. 6.7) were exactly matched.

6.1.3 Fast Rotation Cyclotron Period

Physically, the pure fast rotation function, $F(t)$, describes a bunch of stable spinless particles circling in the ring. The amplitude $F(t)$ at time t is proportional to fraction of the muon particle numbers in the bunch passing by the current detector station. Although all particles in the storage ring are running essentially in the same speed, the speed of light, the bunch is spreading out because of the small momentum distribution of the particles. Ignoring any weak vertical focusing field, the particles with momentum p are circling in the storage ring at a radius r in the uniform magnetic field B,

$$r = \frac{p}{eB} = \frac{\gamma m_\mu \beta c}{eB} \tag{6.8}$$

And the cyclotron period τ_c is

$$\tau_c = \frac{2\pi r}{\beta c} = \frac{2\pi \gamma m_\mu \beta}{\beta eB} = \gamma \frac{2\pi m_\mu}{eB} \tag{6.9}$$

After considering the radial component of the quadrupole electric field, the relation between the gamma and cyclotron period is

$$\gamma = \frac{eB}{2\pi m_\mu f_c}\Big(1 + n(1 - \frac{f_0}{f_c})\Big) \tag{6.10}$$

From Equations 6.8 and 6.9, we see that the higher momentum particles, which occupy the larger radial orbits, take longer time to finish a revolution than those with lower momentum. As time goes by, the bunch spreads out gradually. Eventually, the particles fill the storage ring in azimuth. The bunch spreading rate is uniquely determined by the particle momentum distribution.

In order to properly account for the beam debunching, it is necessary to first fit the average rotation period directly, then extract the distribution of frequencies by means of Fourier transform. An iterative approach using a simulation of the debunching is necessary to compensate for taking a Fourier transform of a truncated time domain.

6.2 Direct Fit Methods to Extract Average Cyclotron Period

The rotation of the muon bunch in the g-2 ring is like a classical oscillation. Theoretically, we can measure the rotation frequency with high accuracy just by counting the rotation turns at a fixed position. The finite observation time, which limits the measurement accuracy of the Fourier transform, does not forbid the classical counting method from achieving a high accuracy. The first method is to count the fast rotation peak centroids, making a average over time to find the average cyclotron period. The second method is to use a sine function to fit the average cyclotron period.

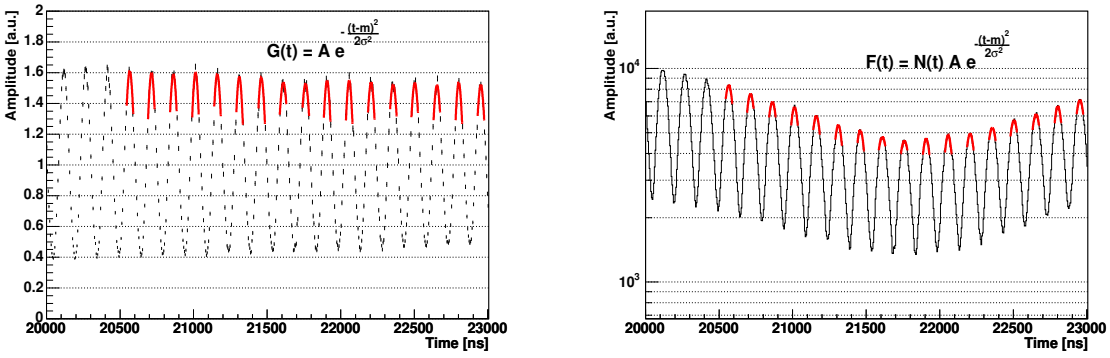

(a) Peaks on $F(t)$ spectrum

(b) Peaks on $S(t)$ spectrum

Figure 6.3: (a) Gaussian fits to fast rotation peaks on the $F(t)$ spectrum. (b) Gaussian fits modulated by g-2 frequency applied to $S(t)$ spectrum. This example uses detector 23, LB chunk data in 2001 run.

6.2.1 Peak Fitting

The centroid of the detected electron bunch could be easily identified in the actual signal spectrum $S(t)$ (see Fig. 6.1) or in the pure fast rotation signal spectrum $F(t)$ (see Fig. 6.2). Since the decay electrons were moving at the same speed as the muons in the storage ring, the centroid in time of these electron signals was equivalent to that of the muon bunch. A Gaussian function was used to fit the peak of each bunch in the pure fast rotation spectrum $F(t)$. Fig. 6.3 (a) shows Gaussian fit examples on the $F(t)$ spectrum. The fitting range was about 45 ns around the peak center. The mean value of each fit gave the centroid of each bunch. Fig. 6.4 (a) shows the first 200 fast rotation peak mean versus turn number measured by detector 23 during 2001 run. Since in the 2000 and 2001 runs, the injected

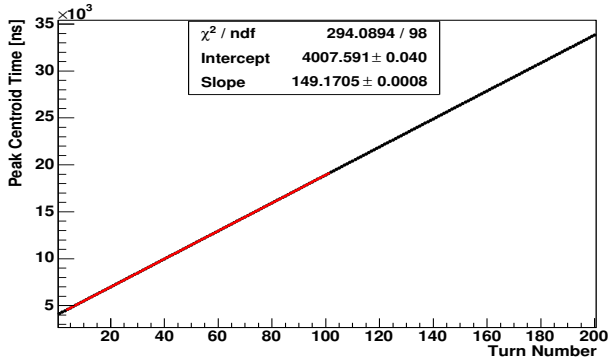

Figure 6.4: The first 200 fast rotation peak centroid time measured by detector 23 during 2001 run. The slope of a straight line fitting in the first 100 turns gives the average fast rotation period. As an example, for the 100 fast rotation turns with the 50^{th} peak at 12.067 μs, the average fast rotation period is 149.170 5 $\pm$ 0.000 8 ns.

muon bunch was quite wide, only the central portion of the peak was used for the fitting. Generally, the Gaussian fitting had a reasonable good χ^2/ndf. The average χ^2 for the 200 peak fits was 1.31 with the RMS 0.69 for the peak fitting on the $F(t)$ spectrum (See Fig. 6.5 (a)). The average rotation period was obtained by fitting a straight line to these peak means. Applying this fit to the pure fast rotation spectrum $F(t)$ gave the slope on Fig. 6.4,

corresponding to $\tau_c = 149.170\ 5 \pm 0.000\ 8$ ns for the 2001 run LB data set. The statistical uncertainty from the fitting was 5.4 *ppm*. This statistical uncertainty was the upper limit for the fitting, since we had and used more than 100 fast rotation turn data.

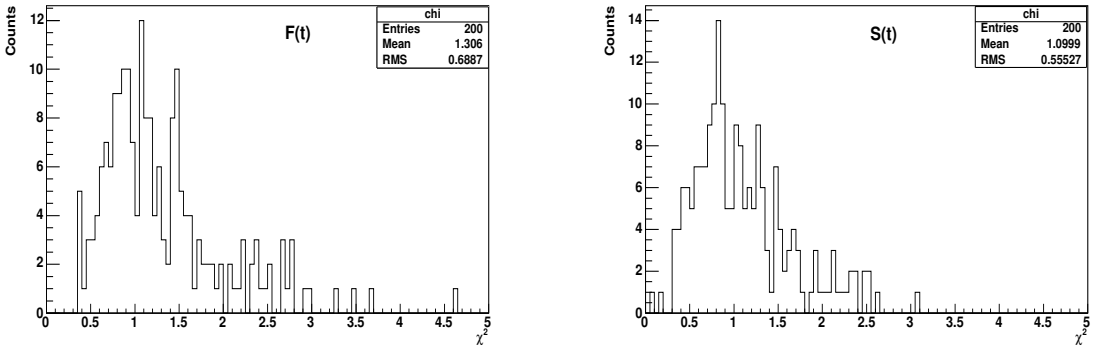

(a) χ^2 for Fast Rotation Peak Fits on the $F(t)$ spectrum

(b) χ^2 for Fast Rotation Peak Fits on the $S(t)$ spectrum

Figure 6.5: χ^2 Distribution for the first 200 fast rotation peak fits on the $F(t)$ spectrum (a) and on the $S(t)$ spectrum (b). The examples uses detector 23, LB chunk data in 2001 run.

The same fitting procedure was applied to the actual signal histogram $S(t)$, except that the Gaussian peak shape was modulated by a 5-parameter function. The fast rotation spectrum was first fit by Eq. 6.1 in the later range between 150 μs and 300 μs, then the fitted parameters were used to modulate the form of the Gaussian peak fit function to ensure that the g-2 modulation did not shift the fitted peak. Fig. 6.3 (b) shows the fitting examples on the $S(t)$ spectrum. The average χ^2/ndf for individual Gaussian fitting was 1.1 with RMS 0.55 for the first 200 fast rotation peaks (See Fig. 6.5 (b)). The linear fitting gave an average rotation period of $\tau_c = 149.172\ 2 \pm 0.000\ 9$ ns with a little higher $\chi^2/ndf = 366.3/98$.

The *peak centroid* method was applied on all sub data sets for the 2000 and 2001 data. Detector 17 was taken as an example for the 2000 run data and Detector 23 was taken as the sample detector for the 2001 data. The average fast rotation period fit for all sub data

sets are listed in Table 6.1. For each separate detector, the statistical error on each data sub set was at the level of 5.4 ppm. It was about 1.3 ppm if we used the sum of the second half ring detectors. This statistics was sufficient in the fast rotation analysis. The fast rotation spectrum from the first half ring detectors were used for systematic study only.

Year	Run Period	Average Period [ns]	Statistical Error [ns]	χ^2/ndof
2000	P1	149.179 9	0.001 5	1.17
	P2	149.196 8	0.001 3	1.05
	P3	149.197 8	0.000 8	1.20
	P4	149.185 9	0.000 4	1.79
	P5	149.172 4	0.001 3	1.17
2001	LB	149.172 5	0.000 8	2.19
	LA	149.160 1	0.000 8	1.03
	HB	149.182 6	0.000 8	2.28
	HA	149.165 8	0.003 7	0.46
	SO	149.182 0	0.001 4	2.45

Table 6.1: Average fast rotation period as determined by the peak counting method. The 2000 results are based on detector 17, which is gated on at 2.6 μs. The average period is an average over 100 fast rotation turns centered at 11.59 μs. The 2001 results are based on detector 23, which is gated on at 4.0 μs. The average period is an average over 100 fast rotation turns centered at 12.96 μs.

This peak counting method was used in previous CERN experiments, when the injected muon bunch had a width of 10 ns. This bunch width was much smaller than the average cyclotron period of 147 ns, and did not overlap itself 10 μs after injection. In the BNL g-2 experiment, the incoming muon bunches had a RMS width about 28 ns. Fig. 6.6 shows the Gaussian peak width versus turn number. The initial full width of the bunch was comparable to the mean fast rotation period and widens by ~ 2 ns each turn. The bunch spreaded out and overlapped itself in the first 20 or 30 turns after injection, which was earlier than most of detectors gate on. For the central part of the peak (45 ns width), it would spread out and overlap in about 130 turns.

After applying the peak Gaussian fitting on the debunched time spectrum and plotting the average fast rotation period of each 100 turns versus time after injection, the average

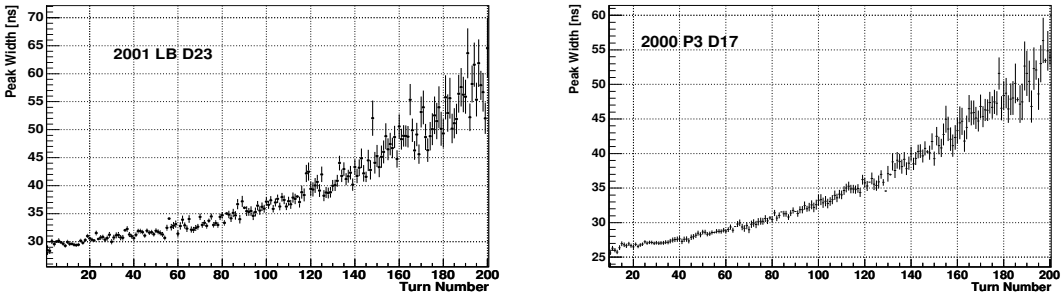

(a) (b)

Figure 6.6: The increasing peak width as the muons debunch over the first 200 turns. (a) Detector 23 (2001, LB data set). (b) Detector 17 (2000, P3 data set).

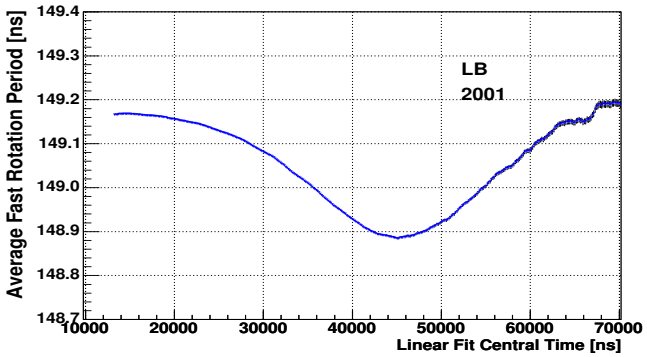

Figure 6.7: The "debunch dip" structure is shown clearly in the average fast rotation period as a function of time. Each point is the slope of the straight line fit as in Fig. 6.4. The time assigned to each point is the middle of the fitting range of 100 turns. The data used in this plot is the sum of detector 13 to 24 in LB period 2001 run.

period varies as shown in Figure 6.7. Each point on the plot is the fast rotation period averaged over 100 turns and plotted with respect to the time of 50^{th} turn. Each bin is the average over ± 7.5 μs. From the figure, we see that the average period decreases from 149.170 ns at early times to a minimum value of 148.85 ns at about 45 μs after injection, after which it again rises. This pattern is unique to the momentum distribution of the

injected muon bunch. Let us define it as the *debunch dip*. We will take advantage of this debunch dip to verify the fitted momentum distribution in Sec. 6.4. For each individual detector, the fast rotation peaks are smeared by the amount expected by statistics after 40 μs. Thus it is necessary to use the detectors in the second half of the ring (i.e. detector 13 to 24 except detector 20) in order to enhance the fast rotation signal. The fast rotation peaks are then very clear, even at 80 μs after injection.

6.2.2 Sinusoidal Fitting

An equivalent method was to fit the fast rotation spectrum with a sinusoidal function. This method extended the fitting range to later time using only one single detector time spectrum. To compare the sinusoidal fit with the peak fit method, the range of the fit was set to be 15 μs, which was equivalent to 100 fast rotation turns. The fitting function was

$$F(t) = 1.0 + \rho(t)\cos(\frac{2\pi t}{T_c} + \phi) \tag{6.11}$$

where $\rho(t)$ was the empirical debunching envelope function (see Fig. 6.2 (a)), which de-

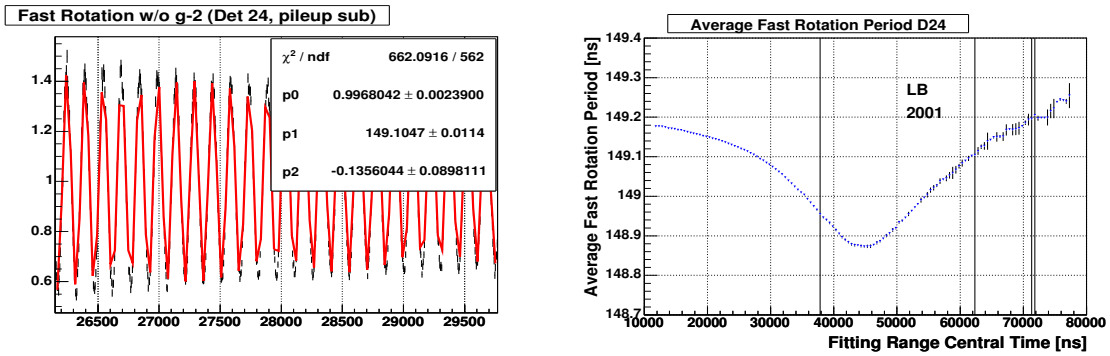

(a) Sinusoidal Fitting Sample

(b) Debunch Dip Structure

Figure 6.8: (a) is the sample fitting using cosine function. (b) is the average fast rotation period of the sinusoidal fitting using cosine function with empirical debunching envelope in LB data chunk 2001 data, detector 24. It shows the dip clearly.

scribed the decreasing peak amplitude. Fig. 6.8 (b) shows the "debunch dip" structure clearly even with one detector data.

The *debunch dip* structures were unique for each data set. Fig. 6.9 shows the overlap of the debunch structures of all 23 detectors in the 2001 run HB data set. It is clear that debunch structures from different detectors match to each other very well in the same data set, although the detectors near kicker have slightly deeper dips, especially for detector 8. The difference was treated as a systematic uncertainty.

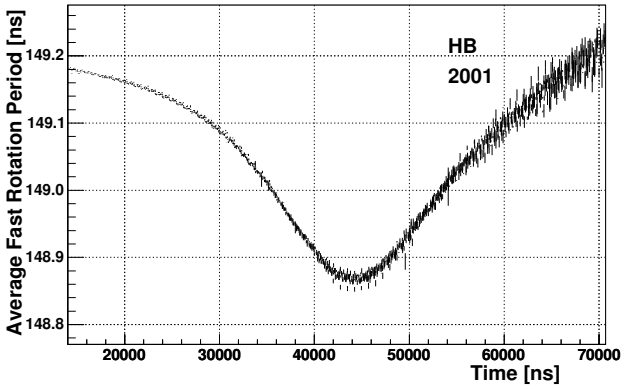

Figure 6.9: Overlap of the "debunch dip" structures measured by sine function fitting method in the 2001 HB data set. Results from all 23 detectors were plotted to show that dip structures are same across azimuthal position.

The debunch structure on the average fast rotation period plots warned us that it was not fair to arbitrarily pick one value at early times to represent the actual average cyclotron period. We need to develop further methods to extract the correct muon momentum distribution. The real Fourier transform method and the comprehensive simulation model are two approaches.

6.3 Real Fourier Transform to Extract Momentum Distribution

The real Fourier transform can be used to extract the muon cyclotron frequency from the observed decay electron spectrum. Since only a cosine Fourier transform with the properly determined initial time t_0 gave the correct frequency distribution, a special procedure must be used to compensate for the missing signal information in the early time after injection, but before detector was gate-on.

The muon revolution frequency distribution $F_\mu(f)$ can be extracted from the real Fourier transform of the pure fast rotation spectrum $F(t)$ when the initial time t_0 was correctly chosen,

$$F_\mu(f) = A \sum_{t_k=t_0}^{t_{max}} F(t_k) \cdot \cos\, 2\pi f(t_k - t_0) \tag{6.12}$$

where the initial time t_0 was the time when the center of mass of the initial bunch passed the detector for the first time after injection. At time $t = t_0$, all frequency components in the fast rotation signal $F(t)$ were simultaneously at maximum. Factor A was practically a constant which was related to the width of the initial muon bunch. The physical electron signals were recorded from t_0 to the maximum time t_{max}.

In the g-2 experiment, the PMTs on the calorimeter stations were gated on after start time t_s to avoid damage to the detectors from the early flash. During the 2001 run, depending on the detector azimuthal position, the start time t_s ranged from 5 μs to 10 μs after the injection. Since t_s was much later than t_0, the frequency distribution $F_\mu(f)$ contains a unknown part $\Delta(f)$ from t_0 to t_s and an available part $F_\mu^1(f)$ from t_s to t_{max} [73].

$$F_\mu(f) = \Delta(f) + F_\mu^1(f) \tag{6.13}$$

where $\Delta(f)$ and $F_\mu^1(f)$ were defined as follows,

$$\Delta(f) \equiv A \sum_{t_k=t_0}^{t_s} F(t_k) \cdot \cos\, 2\pi f(t_k - t_0)$$

$$F_\mu^1(f) \equiv A \sum_{t_k=t_s}^{t_{max}} F(t_k) \cdot \cos\, 2\pi f(t_k - t_0) \tag{6.14}$$

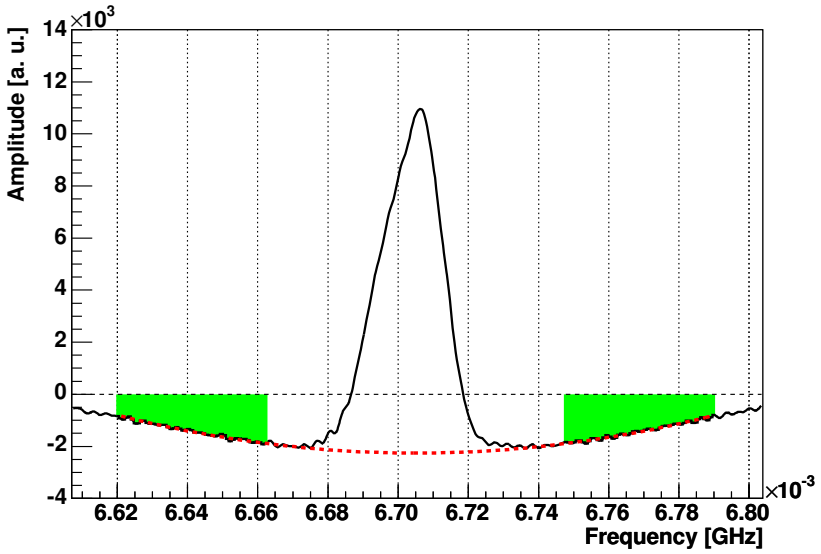

Figure 6.10: The real Fourier transform $F_\mu^1(f)$ from the available data which was between the start time $t_s = 4.7$ μs and $t_{max} = 300$ μs for detector 23 LB run period in 2001 run. The t_0 time had been carefully determined, such that the spectrum was the most symmetric about the mean. The (red) parabolic curve was the approximated $\Delta(f)$. The two (green) shade regions were used to determine the background shape. Since these regions corresponded to the area immediately outside of the vacuum chamber, there were no stored muons in these area, so they could safely be used to fit the background.

Figure 6.10 shows the real Fourier transform $F_\mu^1(f)$ between the start time $t_s = 4.7$ μs and $t_{max} = 300$ μs for detector 23 in 2001 run, after the t_0 was determined carefully. Studies had shown that the correct t_0 time corresponded to a symmetric $F_\mu^1(f)$ spectrum.

Although the $\Delta(f)$ cannot be obtained from the data $F(t_k)$ directly, it was shown that it can be calculated, to first approximation, simply by using the available part of the Fourier transform. In practice, this approximation was treated as a parabolic background on the available part of the transform $F_\mu^1(f)$. See the (red) parabolic curve on Figure 6.10.

$$\Delta(f) = a\{1 - b[(f - \langle f \rangle)^2 + \sigma^2]\} \tag{6.15}$$

where $\langle f \rangle$ and σ are the mean and standard deviation of the frequency distribution. a and b are constants.

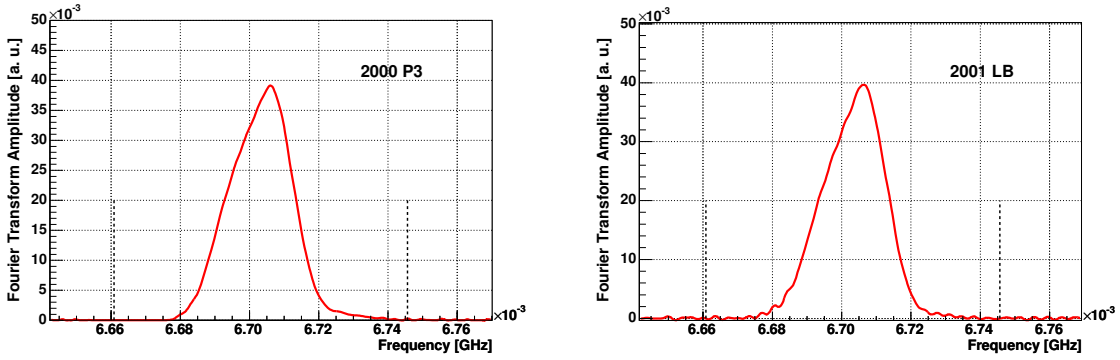

(a) (b)

Figure 6.11: (a) is the muon cyclotron frequency distribution in 2000 after background subtraction using the real Fourier transform. After applying the parabolic background treatment to the first approximation $F_\mu^1(f)$, we got the muon cyclotron frequency distribution, hence the muon momentum distribution. The data of detector 17 in P3 run period is shown. Detector station 17 was gated on at 2.6 μs in 2000 run. (b) is the 2001 muon cyclotron frequency distribution from real Fourier Transform. The data of detector 23 in LB run period was used. The dash lines indicate the equivalent vacuum chamber edges.

Subtracting the background as described above, we extracted the muon cyclotron frequency distribution, which was equivalent to momentum distribution. Two examples are shown on Figure 6.11 (a) and (b) for 2000 and 2001 data. The muon momentum distributions for other data sets were also produced. In these cases, the initial zero time t_0 was found by sweeping through with a step of 0.1 ns to determine the best value. This step size was 5 time smaller than that was used in the reference [73].

The uncertainty of the mean radius found using this Fourier transform method was about 0.1%, which was sufficient to estimate the systematic uncertainty on ω_a at the level of 0.1 ppm. The Table 6.2 lists the mean fast rotation frequency of all data sets. The biggest

Year	Run Period	Mean on Distribution [MHz]	RMS [MHz]
2000	P1	6.701 91	0.009 40
	P2	6.702 63	0.010 17
	P3	6.702 00	0.009 59
	P4	6.702 46	0.008 69
	P5	6.703 55	0.009 82
2001	LB	6.703 26	0.009 66
	LA	6.703 19	0.009 89
	HB	6.702 78	0.009 62
	HA	6.703 48	0.011 82
	SO	6.704 49	0.010 84

Table 6.2: Average fast rotation frequency from the real Fourier Transform for 5 sub data sets in 2000 and 4 sub data sets in 2001. The 2000 results are based on Detector 17, which is gated on 2.6 μs. The 2001 results are based on Detector 23, which is gated on 4.0 μs.

difference, which was 0.025%, was between P1 and P4 sub sets in 2000 data. This uncertainty was not acceptable for the lifetime analysis. There were two potential limitations to this method. The first one was that the accuracy of the Fourier transform was limited to $\delta f \sim 1/\Delta t$ by the finite time of observation Δt. The second was that a systematic error could be introduced when compensating for the missing data while the detectors were gated off. The later the detector gate-on time, the bigger the background compensation and the less reliable the results.

6.4 Comprehensive Simulation Model

In order to improve the resolution of mean momentum, I have developed a simulation model to reproduce the fast rotation time spectrum. The momentum distribution from the Fourier transform was parameterized to provide the initial input to the simulation. The distribution was then adjusted such that data and simulation match not only the fast rotation time spectra $F(t)$, but also the "debunch dip" structures.

6.4.1 Simulation Model

The muon particle in a uniform magnetic field moves along a determined orbit with the cyclotron frequency before it decays. In the BNL g-2 experiment, a weak electrostatic field is also applied, yet the above statement still holds; the determined orbit simply becomes an equilibrium orbit for a group of muons with cyclotron frequency f_k. The injected bunch consists of a set of such muon groups with a spatial envelope $R(t)$. The full interval of the muon cyclotron frequency spread Δf is divided into N small frequency bands, $\Delta f = N\delta f$. Muons in each group circle around their equilibrium orbit coherently and do not spread out in a very long time, t_{max}. The amplitude of these coherent oscillations, $A_k(f)$, is proportional to the number of muons inside the frequency interval $(f_k - \delta f/2) < f < (f_k + \delta f/2)$, for $k = 1, 2, \ldots, N$. At time t after injection, the fast rotation signal $F(t)$ measured by a detector is the superposition of amplitude from all frequency components. Figure 6.12 shows a schematic view of the fast rotation simulation model.

For simplicity, but without loss of generality, let us assume there is only one detector, which is located at zero degree in azimuthal position. Initially, at $t = 0$ time, the center of frequency band with cyclotron frequency f_k is at $\phi_k(0)$. At time t, the k^{th} frequency band has circled n turns around the ring, and its center gets to $\phi_k(t)$ in azimuth with respect to the detector,

$$\phi_k(t) = 2\pi f_k t + \phi_k(0) - 2n\pi \tag{6.16}$$

$$n = \mathrm{Int}(\frac{2\pi f t + \phi_k(0)}{2\pi}) \tag{6.17}$$

The value of $\phi_k(t)$ is in the range of $(-\pi, \pi]$. If $\phi_k(t) > \pi$ in Eq. 6.16, $\phi_k(t) = \phi_k(t) - \pi$.

The spatial amplitude immediately in front of the detector from this frequency band is $R_k(t)$,

$$R_k(t) = \begin{cases} G(\phi_k(t)), & -\frac{\delta\varphi_k}{2} \le \phi_k(t) \le \frac{\delta\varphi_k}{2} \\ 0, & \text{otherwise} \end{cases} \tag{6.18}$$

where $\delta\varphi_k$ is the spatial width in radians and $G(\phi)$ is the bunch spatial function form. The bunch spatial shape $G(\phi)$ could be any analytical function or empirical form. This

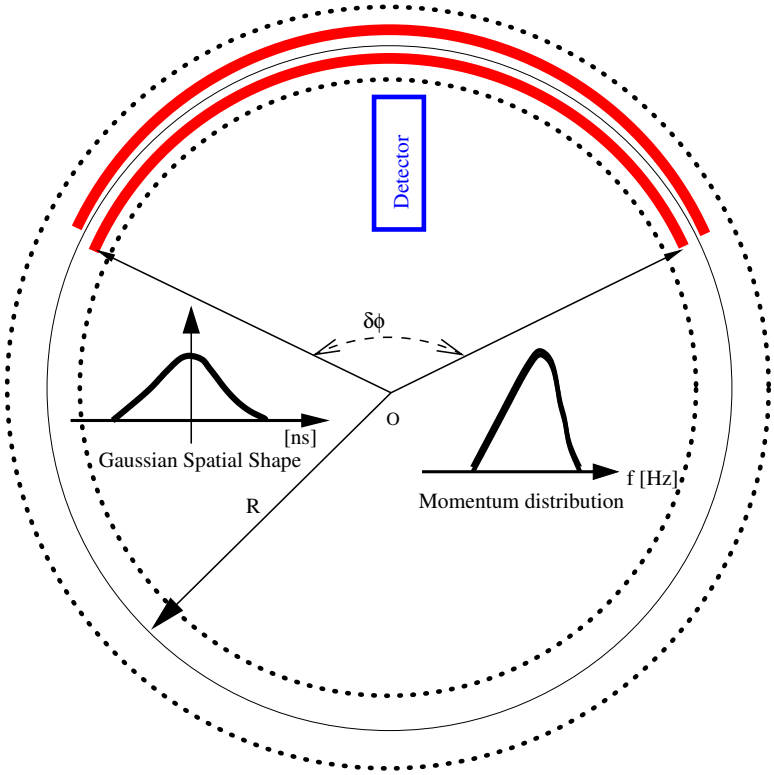

Figure 6.12: A schematic view of the fast rotation simulation model. Two muon bands are shown as examples. Each band represents a group of muons with the same cyclotron frequency. Each group of muons has a truncated Gaussian spatial distribution. The group of muons circulates in the ring. Its amplitude is recorded when the band passes by the detector. The sum of all frequency components (bands) gives the fast rotation signal at any time.

functional form can be verified by the signals from the Fiber Harp Monitor, a skein of vertical scintillating fibers. Although, a square shape, a triangle shape and a Gaussian function form have been tested in this model, a typical signal from the T0 counter (Fig. 3.8) shows that the beam bunch is approximately Gaussian in shape. The RMS width σ of Gaussian varies from 18 ns to 28 ns depending on the data sets in the 2000 and 2001 run.

The tail of the Gaussian function are truncated beyond the expansion factor d range since the injected bunch has limited width. The actual bunch spatial width or effective width W then is $W = 2\sigma \cdot d$. All frequency bands have the same length W in nanoseconds,

whereas their angular width $\delta\varphi_k = 2\pi f_k W$ in radians are different. The bunch spatial center is aligned at the initial time $t = t_0$. The initial phase of all frequency bands are set to be equal. In this case, they are set to be zero.

The fast rotation signal $F_{sim}(t)$ is the superposition of N frequency components,

$$F_{sim}(t) = \sum_{k=1}^{N} A_k(f)\ R_k(t) \tag{6.19}$$

where $\sum_{k=1}^{N} A_k(f) = c$. The normalization factor c is proportional to the total stored muon number.

6.4.2 Determine the Frequency Width

In this model, the muons having cyclotron frequency f_k with bounds $f_k \pm \delta f/2$ will rotate coherently at all time, or at least up to the time we are still interested in. The width of the interval δf is estimated such that the above requirement is satisfied. Let us assume at time $t = 0$, the muons of band f_k are at azimuth $\phi = 0$. At time t, the azimuth spread $\delta\phi$ between $f_k - \delta f/2$ and $f_k + \delta f/2$ will be,

$$\delta\phi = 2\pi\ \delta f\ t \tag{6.20}$$

For simplicity, let us neglect the electron drift time difference and detector geometric size; only considering the time bin width of the spectrum. The requirement is that the muons, which were at the same azimuthal position at $t = 0$ time, will remain in the same time bin at $t = t_{max}$. This is equivalent to saying that about 50% of the muons originally in the same time bin will remain in the same time bin until $t = t_{max}$. The fast rotation pattern is visible even until $t_{max} = 80\ \mu$s and the bin width of histogram is 5 ns. Therefore the azimuth spread $\delta\psi \leq 2\pi \times 5/149.2$ radians. The 149.2 ns is the approximated mean fast rotation period.

$$\delta f \leq \frac{\delta\phi}{2\pi t} = \frac{5}{149.2 \times 80\ \mu\text{s}} = 0.42\ \text{kHz} \tag{6.21}$$

The $\delta f = 0.42$ kHz frequency width is sufficient for the simulation.

In the experiment, we observe decay electrons, not the muons themselves. However, this makes no difference on the time spectra $S(t)$ and $F(t)$ because the decay electrons, like the muons, are moving at roughly the speed of light and under small angles to the parent muon trajectories. A study shows that doubling the minimal frequency width δf from 0.42 kHz to 0.84 kHz, only changes the simulated time spectra within the statistical error up until $t = 80$ μs. For the average fast rotation period spectra, the difference is zero up to 30 μs, and less than 0.004 ns up to 60 μs. These errors are within the statistical uncertainty as well.

6.4.3 Defining Minimization Criteria

When a cyclotron frequency distribution is fed into this simulation, it produces a pure fast rotation time spectrum as that shown on Fig. 6.2 in Sec. 6.1.1. Only the correct distribution produces a simulated time spectrum $F_{sim}(t)$ which matches to the data spectrum $F(t)$ best. Two parameters will be used to quantify the degree of similarity between simulation $F_{sim}(t)$ and data spectrum $F(t)$. One is the χ^2 of the fast rotation time spectrum, and the other is the distance square DD value between the debunch dip structures.

The first step of minimization is applied to the difference between the simulated fast rotation spectrum $F_{sim}(t)$ and the data $F(t)$. The general χ^2 from start time t_{min} to maximum time t_{max} is given by

$$\chi^2 \equiv \sum_{t_j=t_{min}}^{t_{max}} \frac{(F_{sim}(t_j) - F(t_j))^2}{\sigma^2_{F(t_j)}} \tag{6.22}$$

where the continuous integral over time becomes summation over discrete time t_j for the histograms. Substituting $F_{sim}(t)$ (Eq. 6.19) into χ^2 gives

$$\chi^2 \equiv \sum_{t_j=t_{min}}^{t_{max}} \frac{(\sum_{k=1}^{N} A_k(f)\ R_k(t) - F(t_j))^2}{\sigma^2_{F(t_j)}} \tag{6.23}$$

The start time t_{min} is any time after detector gate-on and is set to 20 μs, and t_{max} is about 60 μs. This late time is chosen to avoid the unpredictable effects from beam scraping at early times. In this 40 μs time range, there are 8,000 time bins in the spectrum. Recall

that the error $\sigma_{F(t_j)}$ on the data spectrum was over-estimated (see Sec. 6.1.1), the χ^2 could be small.

A second step of the minimization is made on the so-called "debunch dip" structure as shown on Fig. 6.7. The distance square between the simulated average fast rotation period τ_{sim} and the data τ is calculated.

$$DD \equiv \sum_{t_j=t_{min}}^{t_{max}} \Big[\tau_{sim}(t_j) - \tau(t_j)\Big]^2 \tag{6.24}$$

where $\tau_{sim}(t)$ and $\tau(t)$ are the average fast rotation period at time t from the best simulation and real data, respectively. Again, t_{min} is set to be 20 μs, and t_{max} is set to be 60 μs. When the best momentum distribution is found, both Eq. 6.22 and Eq. 6.24 should have their optimal values.

6.4.4 Parameterizing the Momentum Distribution

Theoretically, it is possible to minimize the χ^2 in Eq. 6.23 by solving N equations simultaneously of $\frac{\partial \chi^2}{\partial A_k(f)} = 0$. Recall that N is the total bin number on the momentum distribution histogram. This fitting is applicable when there are 20 or 30 bins on the momentum distribution histogram. However, there are 90 bins in the distribution histogram which is equivalent to 90 free parameters. Although, it is still possible to fit all these free parameters to extract the frequency distribution, there is a way to reduce the parameter number.

The intuition on how to parameterize the momentum distribution comes from the Fourier transform study. We have obtained a good approximation of the muon momentum distribution from the simple Fourier transform in Sec. 6.3, which showed that the central part on the frequency distribution is recovered very well. As an example, Fig. 6.13 shows three Fourier transform results. The black solid line, which is the 90-bin background subtracted Fourier transform of $F(t)$ (copy of Fig. 6.11 (b)), forms the input momentum distribution to the simulation model. The simulation then produces a fast rotation time spectrum based on this input. Then, the simulated fast rotation spectrum is Fourier transformed at two

different starting times. The red dashed line is the Fourier transform starting at $t = 0$ μs, and the green dash-dotted line is the Fourier transform starting at $t = 4$ μs.

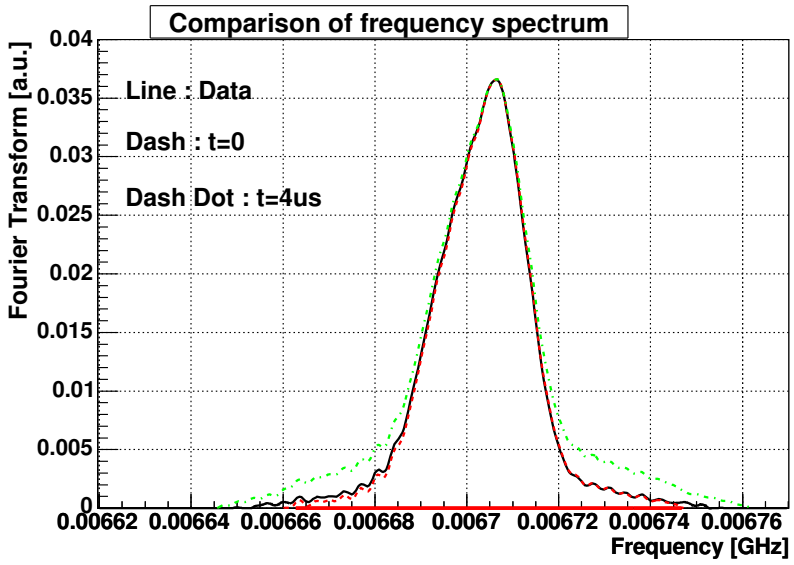

Figure 6.13: The black solid line is the Fourier transform result from data. It is the input distribution to the simulation program. The red dashed line is real Fourier transform starting at $t = 0$ μs. The green dash-dotted line is the real Fourier Transform starting at $t = 4.0$ μs.

It is clear that the red dashed line matches to the black line very well, which means that the Fourier transform *does* recover the momentum distribution if we have the full information on the decay electrons. But, in BNL g-2 experiment, the earliest gate-on time of the calorimeters is about 4.0 μs. The green dash-dotted line matches the black solid line only in the central region, meaning that the Fourier transform of the truncated time spectra does not do well in the wings. In the wings, the green dash-dotted line is too high compared to the input spectrum. In order to extract the original time spectrum from the Fourier transform of a truncated spectrum, the transform will be parameterized in a manner that allows the wings to be lowered independently of the central part. Six parameters can characterize the momentum distribution based on the Fourier transform result.

Fig. 6.14 depicts how the parameterization is done and Table 6.3 shows the meaning of these six parameters and their typical value. The center of the frequency distribution matches the mean radius of the vacuum chamber center in the storage region. Since the magic gamma is 29.30344 and 29.30343 for the 2000 and 2001 run, respectively, the center of the cyclotron frequency is at $f_{2000} = 6.704\ 841\ 31$ MHz and $f_{2001} = 6.704\ 822\ 43$ MHz. By introducing the parameterized distribution, we no longer have to fit the array of 90 parameters.

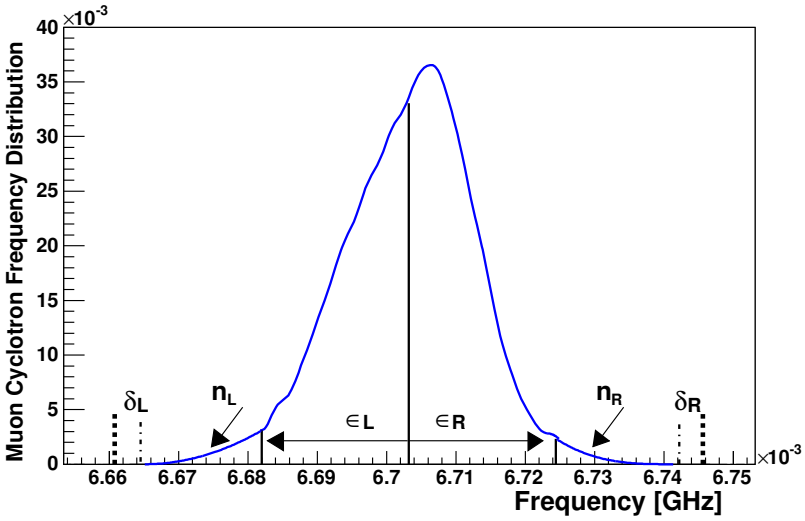

Figure 6.14: The parameterized momentum distribution. See Table 6.3 for the typical value of each parameter.

The parameterized distribution is created as follows:

- The central $\epsilon_L + \epsilon_R$ part on the distribution remains unchanged from the Fourier transform result.
- The part of δ_L on the low frequency end and δ_R on the high frequency end are unfilled or removed because of the beam horizontal scraping at early time.
- The distribution between the f_{Lc} and f_{Lb} is approximated by a n_L order polynomial

function.

- The distribution between the f_{Rc} and f_{Rb} is approximated by a n_R order polynomial function.
- The distribution at boundary f_{Lb} and f_{Rb} is continuous. Both the value and its first order derivative at the boundary points are zero.
- At the point f_{Lc} and f_{Rc}, the values are equal on two sides.

Parameter	Typical Value	comments
ϵ_L	0.240	left central part
ϵ_R	0.230	right central part
δ_L	0.005	left edge scraped
δ_R	0.050	right edge scraped
n_L	3	n_{th} polynomial on left
n_R	2	n_{th} polynomial on right

Table 6.3: Six parameters are used to construct the muon cyclotron frequency distribution which will be input to the simulation.

6.4.5 The Iteration Procedure and the Final Momentum Distribution

The parameterized momentum distribution of each data set was fed into the simulation model and a fast rotation time spectrum was reproduced. The initial phase of the simulated spectrum was shifted by adjusting the t_0 parameter to align itself with the data spectrum. Since the χ^2 defined in Eq. 6.22 was very sensitive to the t_0 parameter, the t_0 parameter was optimized easily by scanning at a step size of 0.05 ns. The t_0 parameter was about 55 ns in the 2000 run and 15 ns in the 2001 run, as listed in the last column in Table 6.4.

Each of the muon bunch has Gaussian spatial shape in the analysis. The RMS width of the muon bunch in the simulation model is initialized to the width of the earliest (first complete) fast rotation peak on the fast rotation time spectrum (see Sec. 6.2.1). Then, the Gaussian RMS of muon bunch is varied and input into the simulation in order to match

simulated spectrum and data spectrum. The expansion (cut off) factor d is also varied to change the effective width of the bunch. The fast rotation peak amplitudes and the depth of the trough at early time are sensitive to the total bunch width. The narrower bunch produces the higher peak and the deeper trough, and vise versa. Both Gaussian RMS and d parameter are adjusted recursively until a reasonable χ^2 is reached.

After optimizing phase shift t_0 and spatial parameters, we then adjust the parameterized momentum distribution to reproduce the fast rotation spectrum which matches the data. The six parameters which parameterize the momentum distribution are adjusted recursively. For each case, the fast rotation time spectrum is produced and the nominal average cyclotron period of the simulated time spectrum is also created. The χ^2 and DD value are calculated. After a series of recursions, the best match between the simulation spectrum and data spectrum is found. Fig. 6.15 (a, b, c, and d) show four snapshots of the best simulated fast rotation time spectrum and the data spectrum at different time ranges. The χ^2 is calculated from 20 μs to 60 μs on the spectra. Since the bin width on the fast rotation time spectra is 5.0 ns, there are 8000 bins in total. In the simulation, we have 6 parameters from the frequency distribution and 2 parameters for spatial bunch shape. The total number of degrees of freedom is 7992.

A Gaussian spatial shape is used for all these fits. Table 6.4 lists the spatial parameters of all data sets at the best simulation case. The beam bunch width steadily increases for the data sets in 2000 run, and it keeps similiar value in 2001 run. This width has been confirmed by the signals from T0 counter and the beam bunch width at the very early time in the peak fitting method. The time shift between the data and the simulated spectrum, t_0, is detector dependent. The listed numbers are for detector 17 in the 2000 run and detector 23 in the 2001 run.

Table 6.5 lists the parameters on the final cyclotron frequency distributions. It is straightforward to see that for those data sets with smaller muon losses, for example, P5 data set in 2000 and HB, HA data sets in 2001, the beam occupies smaller phase space

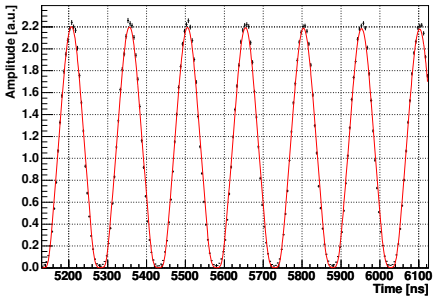

(a) At 5 μs

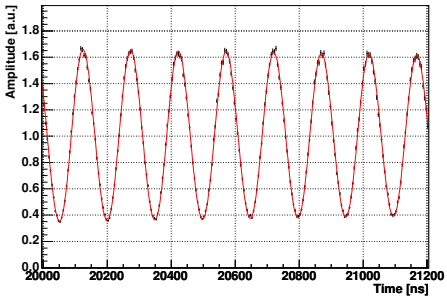

(b) At 20 μs

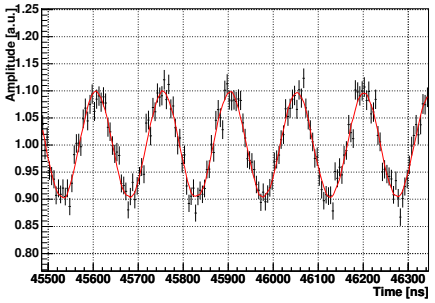

(c) At 46 μs

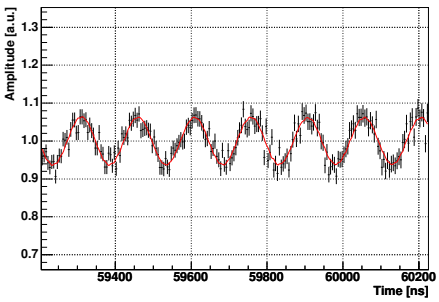

(d) At 60 μs

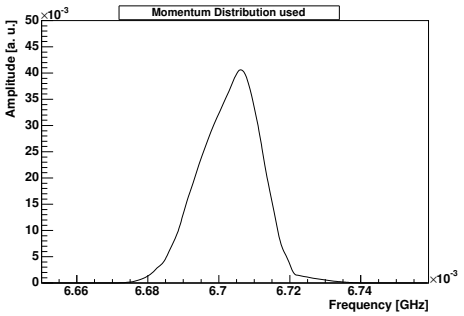

(e) Momentum Distribution

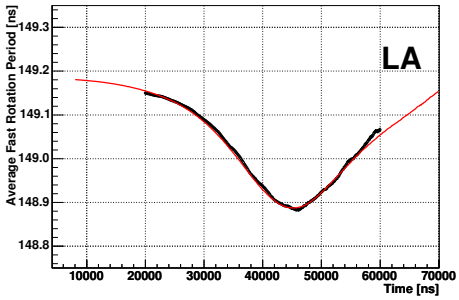

(f) Average Fast Rotation Period

Figure 6.15: The simulated fast rotation spectrum and data spectrum comparison. Four snapshots are shown, (a) the early time at 5 μs, (b) the middle time at 20 μs, (c) the late time at 46 μs, and (d) the very late time at 60 μs. The points with error bar are the data, and the red smooth curves are fit results. The best fitted momentum distribution is plotted in (e). The thin smooth line on (f) is the average fast rotation period from the simulated spectrum, and the bold line is from the data. The fast rotation time spectrum is from detector 23, LA data set in 2001 run.

Simulation					
Data Set		Gaussian 2σ [ns]	Expansion Factor d	Effective Width $W = 2\sigma d$ [ns]	Alignment t_0[ns]
2000	P1	36.0	1.60	57.6	50.00
	P2	43.3	1.60	69.3	51.50
	P3	49.3	1.60	78.9	55.00
	P4	54.5	1.75	95.4	57.50
	P5	56.3	1.80	101.3	55.00
2001	LB	58.5	1.85	108.2	20.00
	LA	58.5	1.80	105.3	14.05
	HB	53.8	2.00	107.6	17.00
	HA	53.8	2.00	107.6	12.00

Table 6.4: The spatial parameters of the injected bunches for different run chunks in 2000 and 2001 run. The effective width is calculated as $W = 2\sigma \cdot d$.

in the storage region (i.e. δ_L and δ_R are big). This is exactly what we expected because beam scraping at early time has removed those muons with either too small or too large equilibrium orbit radius. The precision on the parameters is equivalent to the half of the last decimal digit.

	Set	ϵ_L	ϵ_R	δ_L	δ_R	n_L	n_R
2000	P1	0.2385	0.2435	0.0250	0.0045	3	2
	P2	0.2242	0.2253	0.1650	0.0200	3	2
	P3	0.2185	0.2243	0.1352	0.0380	3	2
	P4	0.2200	0.2243	0.1342	0.0380	3	2
	P5	0.2167	0.2233	0.1202	0.0650	3	2
2001	LB	0.2450	0.2350	0.0574	0.0755	3	2
	LA	0.2400	0.2200	0.0800	0.0400	4	2
	HB	0.2550	0.2420	0.0920	0.0950	3	2
	HA	0.2500	0.2400	0.1280	0.0600	3	2

Table 6.5: The fitted frequency distribution parameters from fast rotation spectra for all data sets in the 2000 run and the 2001 run.

Table 6.6 gives the final average cyclotron frequency values from the simulation, the χ^2/ndf value between the simulation and the data for all data sets in the 2000 and 2001

run. The statistical uncertainties can be ignored since we have enough fast rotation cycles. Fig. 6.16 and Fig. 6.17 show the match of the debunch dip structures between the best simulation results and data for all data sets. Generally, they match each other very well. The second last column in Table 6.6 gives the differences on the debunch dip as calculated using Eq. 6.24.

Data Set		Fit to $F(t)$				Debunch Dip	
		Mean Freq. $\bar{f}_{rot}$[MHz]	χ^2/ndf	Ave. Period $\bar{\tau}_c = \frac{1}{\bar{f}_{rot}}$[ns]	RMS [kHz]	DD [ns^2]	Syst. [ppm]
2000 μ^+	P1	6.701 661	0.685	149.216 7	8.269	0.01172	6.15
	P2	6.702 546	0.747	149.197 0	8.670	0.02072	10.86
	P3	6.701 811	0.740	149.213 3	8.521	0.01841	7.05
	P4	6.702 108	0.794	149.206 8	8.619	0.01559	7.05
	P5	6.703 401	0.661	149.178 0	8.538	0.01135	5.59
2001 μ^-	LB	6.702 355	1.183	149.201 2	8.789	0.01070	5.61
	LA	6.702 215	1.179	149.204 4	8.646	0.01180	6.19
	HB	6.702 028	1.185	149.208 5	8.757	0.01505	7.89
	HA	6.702 332	0.551	149.201 8	8.354	0.03103	16.27

Table 6.6: Average fast rotation frequencies and the distance on the "debunch dip" between the data and simulation of all data sets in the 2000 and 2001 run. The minimization parameter DD is defined in Eq. 6.24. The systematic uncertainties are calculated based on the DD distance (see Sec. 6.5.1).

6.5 Systematic Error on Momentum Distribution

This model simulates relativistic particles moving in a magnetic field on their equilibrium orbits. The effects with slow frequency such as exponential decay, (g-2) oscillation, and coherent betatron oscillation, have been removed from the pure fast rotation spectrum. The fitting on the $F(t)$ spectrum is robust with respect to frequency distribution because of the over-estimated errors. Fortunately, the "debunch dip" structure is sensitive to the cyclotron frequency distribution. This sensitivity is the key in estimating the systematic uncertainty.

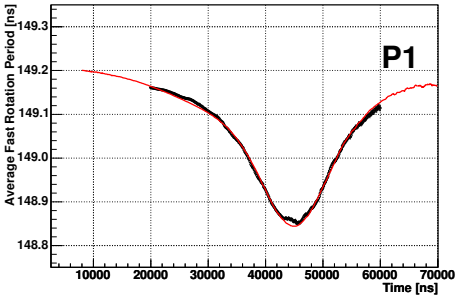

(a) P1

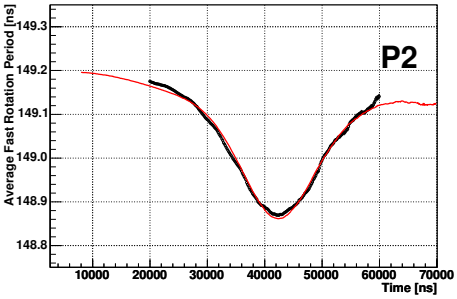

(b) P2

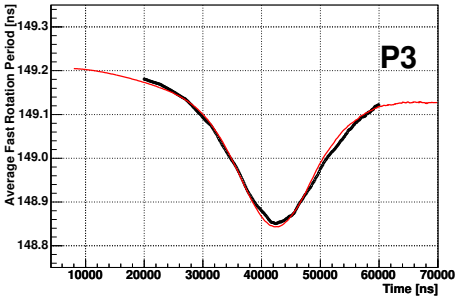

(c) P3

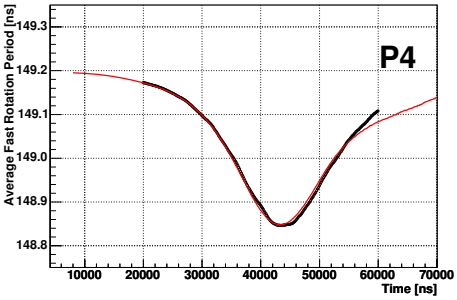

(d) P4

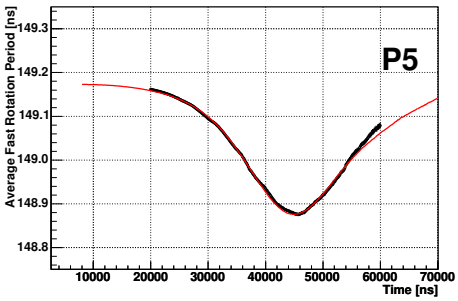

(e) P5

Figure 6.16: The best simulated results of average fast rotation period for the 2000 data. The open circles are "debunch dip" of the data, and the red lines are from the best simulated results.

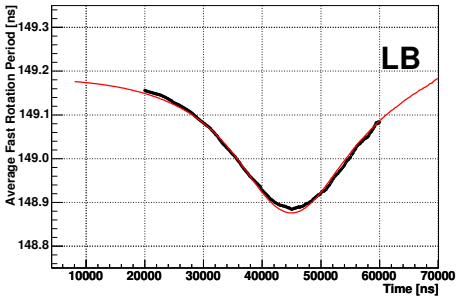

(a) LB

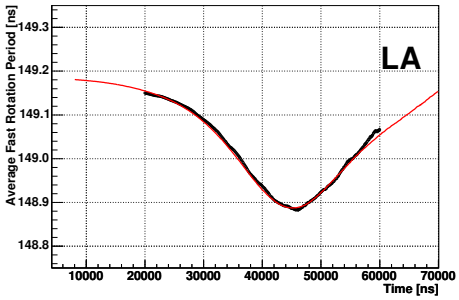

(b) LA

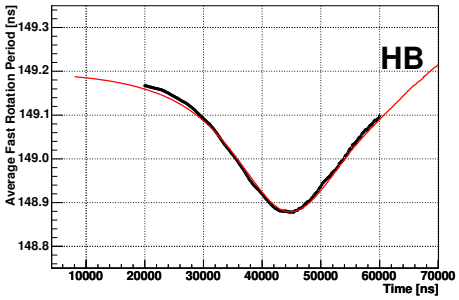

(c) HB

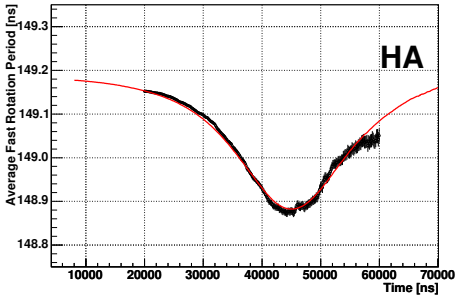

(d) HA

Figure 6.17: The best simulated results of average fast rotation period for the 2001 data. The open circles are "debunch dip" of the data, and the red lines are from the best simulated results.

6.5.1 Sensitivity of the Debunch Dip Structure

The debunch dip structure is very sensitive to the fast rotation frequency distribution. As an example, when we reach the best simulation for LA data set, the $\chi^2/ndf = 1.179 \pm 0.016$ between the data spectrum $F(t)$ and the simulated time spectrum. In this case, the DD value is 0.01180 ns^2. Let us shift the mean frequency on the best matched frequency distribution by $\delta\bar{f}/\bar{f} = 14$ ppm, and input the new distribution into simulation. We compare the two simulation spectra and find that $\chi^2/ndf = 1.011 \pm 0.016$ between the new simulation

and the best simulation spectrum[1], but the DD between the two simulated spectra become 0.0267 ns^2, as shown on Fig. 6.18. This means that the 0.0267 ns^2 integrated difference between the two debunch dip structures corresponds to the 14 ppm difference of the mean fast rotation frequency on the momentum distribution. Thus, the sensitivity of debunch dip structure can be written

$$s = \frac{14 \text{ ppm}}{0.0267 \text{ ns}^2} = 5.24 \text{ ppm}/10^{-2} \text{ ns}^2. \tag{6.25}$$

Using frequency distributions from other data sets gives the same sensitivity values.

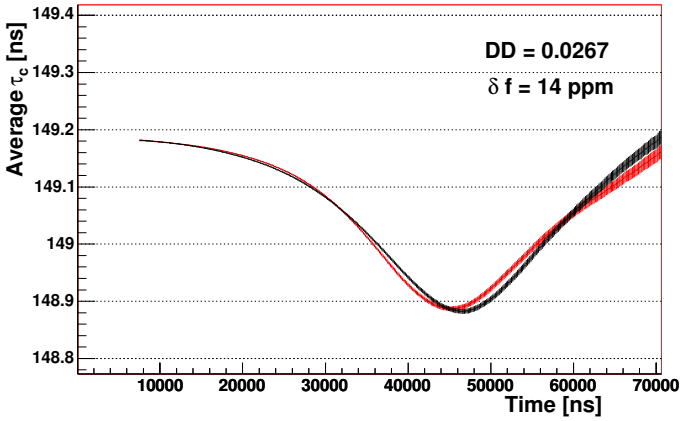

Figure 6.18: Sensitivity of debunch dip structure. The light (red) line is the "debunch dip" structure from the best simulated momentum distribution, and the dark line is the structure from the artificially modified momnetum distribution. The difference of the mean fast rotation frequency on these two momentum distribution is 14 ppm.

The systematic uncertainties corresponding to the DD values at the best simulation cases are calculated by multiplying the sensitivity to the DD values listed in Table 6.6. And the calculated systematic uncertainties $\delta f/f = DD \times s$ are listed in the last column on Table 6.6 for the 2000 and 2001 run data. The average uncertainties are from 5 to 16 ppm, which are much smaller than the uncertainty from dilated lifetime analysis for each data set.

[1] To calculate the χ^2/ndf, the error on the best simulated spectrum is quoted as that on the data spectrum

6.5.2 Detector Variation

The best momentum distribution is extracted by fitting the fast rotation time spectrum of the earliest gate-on detector. Detector 17 is used for the 2000 data and detector 23 for the 2001 data. Let us call them *reference detectors*. As shown in Sec. 6.2.2, the debunch structures match to each other between different detectors with a small deviation in the same data set. The DD distance between any detector to the reference detector is defined as $DD_i = \sum_{t_j=t_{min}}^{t_{max}} (\tau_i(t_j) - \tau_{ref}(t_j))^2$, where $i = 1, 2, \ldots, 24$ except the reference detector. These DD values are calculated for all detectors, and the distribution is shown on Fig. 6.19 for HB data set as an example. The mean difference for the HB data sets is 0.0043 ns^2,

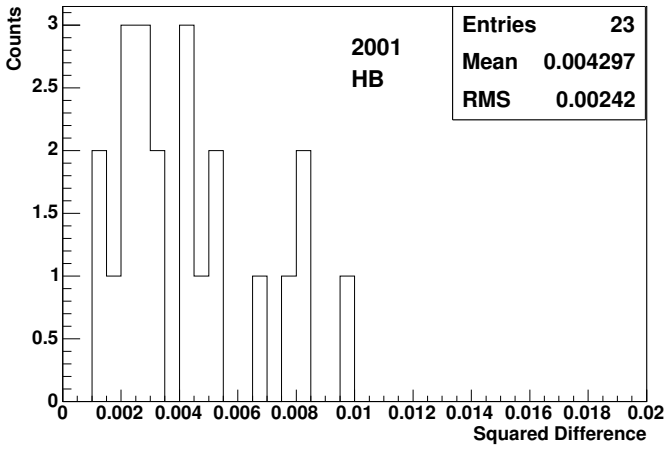

Figure 6.19: The distribution of the square distance DD of the "debunch dip" structure between the reference detector and other detectors.

which sets a minimum systematic 3 ppm on the detector selection, or detector consistency. Detector 8 is the furthest off. The squared distance to the reference detector is 0.02 ns^2, which sets the maximum systematic error of 11 ppm. This maximum value is quoted for all data sets on the systematic errors of the detector selection.

The systematic error from the simulation and the detector selection are combined in quadrature to give total systematic error for each data sets. They are included in the

calculation of the relativistic dilation factor (see Table 6.7).

6.6 Relativistic Dilation Factor

The average special relativistic dilation parameter $\bar{\gamma}$ is calculated from Eq. 6.9. Since the average magnetic field $\langle B \rangle$ value was obtained by NMR of the free proton resonance frequency,

$$2\pi \bar{f}_p = \frac{2\mu_p}{\hbar} \langle B \rangle \tag{6.26}$$

We can rewrite the average γ as

$$\bar{\gamma} = \frac{1}{2\pi \bar{f}_c} \frac{e\langle B \rangle}{m_\mu} = \frac{1}{2\pi \bar{f}_c} \frac{e}{m_\mu} \frac{2\pi \bar{f}_p \hbar}{2\mu_p} = \frac{2\lambda \bar{f}_p}{g \bar{f}_c} \tag{6.27}$$

where $\lambda = \mu_\mu/\mu_p$ is the ratio of the muon and proton magnetic moments; $\bar{f}_p$ is the mean proton magnetic resonance frequency (corrected to vacuum) over the muon orbits; and $\bar{f}_c = 1/\bar{\tau}_c$. The ratio λ is determined from the ground state hyperfine structure interval of muonium atom [2] in an external static magnetic field,λ=3.183 345 39(10) [76]. For the 2000 (2001) run, $a_\mu = 11\ 659\ 204(7)(5) \times 10^{-10}$ ($a_\mu = 11\ 659\ 214(8)(3) \times 10^{-10}$) from which the gyro-magnetic ratio g factor $g/2 = 1.0 + a_\mu$ can be obtained. Recall that $\bar{f}_p = 61.791\ 595(15)$ MHz in 2000 and $\bar{f}_p = 61.791\ 400(11)$ MHz in 2001. We can use one value for magnetic field in each year, since the uncertainty is small 0.24 (0.17) ppm compared to that of average cyclotron period. The maximum difference of the magnetic field between the sub data sets is less than 2 ppm in both 2000 and 2001 run.

The muons in the storage region were focused radially by both vertical dipole magnetic field $\vec{B}$ and the radial quadrupole electric field $\vec{E}_r$. After considering the radial electric field (see Eq. 6.10), an extra term E-field correction term was added to Eq. 6.27. With several steps of derivation, the final average γ value is calculated by Eq. 6.28,

$$\bar{\gamma} = \frac{2\lambda \bar{f}_p}{g \bar{f}_c} \Big[1 + n\big(1 - \frac{f_0 \bar{f}_c}{\bar{f}_c^2 + \sigma^2}\big) \Big] \tag{6.28}$$

[2] The λ value was measured for the positive muon particle.

where σ is the RMS of the fast rotation frequency distribution. The typical value of σ is 8.6 kHz as listed in Table 6.6. f_0 is the magic fast rotation frequency calculated based on ω_a value, n is the field index for the weak quadruple electric field, where $n \simeq 0.135$ for the 2000 run, and n=0.122 or 0.142 depending on data set for the 2001 run. Substituting in the fitted values of the average fast rotation frequency $\bar{f}_c$, RMS width σ of the distribution and magnetic field $\bar{f}_p$ yields individual average γ as shown in Table 6.7.

The statistical uncertainties for the fast rotation analysis are negilible since the sufficient data. The systematic uncertainty includes two parts: one comes from the DD distance of the debunch dip structures between the simulation and data (see Sec. 6.5.1), and another is from the detector selection (see Sec. 6.5.2). These two uncertainties were added in quadrature and entered into Table 6.7.

Data Set		$\bar{\gamma}$	Syst.[ppm]
2000 μ^+	P1	29.315 47	12.60
	P2	29.312 13	15.46
	P3	29.314 91	14.63
	P4	29.313 78	13.70
	P5	29.308 89	11.90
2001 μ^-	LB	29.312 91	12.34
	LA	29.313 44	12.62
	HB	29.313 92	13.54
	HA	29.312 77	19.63

Table 6.7: The final average gamma value with E-field correction included for all data sets in the 2000 and 2001 run.

Chapter 7

The Dilated Lifetime Analysis

The muon dilated lifetime analysis is a fitting procedure which reduces the fast time components, including the g-2 oscillation, by adding together time-shifted decay spectra from subsets of the data. The functional form of this "Inverse-Ratio" method includes corrections to the CBO modulation and the muon losses. The CBO term improves the χ^2 of the fit, but it does not affect the fitted lifetime value. The muon loss term dominates the systematic uncertainty of the fit. Other systematic studies have been done which include the pileup subtraction and the gain correction. By default, all fits use the sum of all available detectors in each data set.

7.1 Inverse Ratio Function

The *ratio method* [51], which concentrates on the g-2 frequency fit, was used in the 1999, 2000, and 2001 anomalous magnetic moment analysis. Systematic uncertainties from slow effects were minimized using this technique. The *inverse ratio method* takes the opposite approach, constructing a spectrum which highlights the muon exponential decay behavior, and minimizes the anomalous spin precession feature.

For a given detector, the time dependence of the observed electron number is determined by the exponential decay of the muon and the anomalous muon spin precession at frequency

ω_a. If we ignore any beam dynamic effects and backgrounds, integrating over electron energies above a certain threshold E_t gives the following form for the electron time spectrum

$$\dot{N}(t) = \frac{N_\circ(E_t)}{\gamma\tau} \cdot e^{-\frac{t}{\gamma\tau}} \cdot \Big[1 + A(E_t)\cos(\omega_a t + \phi(E_t))\Big] \tag{7.1}$$

This is called the *5-parameter* function. $\dot{N}(t) = \mathrm{d}N(t)/\mathrm{d}t$ is the decay electron rate at time t, where $N(t)$ is the muon number in the ring at time t. $N_\circ$ is the initial muon number at time $t = 0$. The electron time spectrum is usually fit with the 5-parameter function and the ω_a and $\gamma\tau$ parameters are extracted. $A(E_t)$ is the anomalous spin precession amplitude (called the "asymmetry"). Both $A(E_t)$ and the phase $\phi(E_t)$ depend on the electron energy since the electrons with low energy deflected more by the magnetic field and traverse a shorter path before striking the calorimeter. We have to keep the asymmetry term because the energy threshold could not be lowered to accept all decay electrons. The inverse ratio method is developed to minimize the effect of the anomalous spin precession term in Eq. 7.1 in the final fitting function.

In the inverse ratio method, electron data having time spectra of the form $\dot{N}(t)$ are randomly split into four subsets $n^+(t)$, $n^-(t)$, $n^0(t)$, and $n^0(t)$. Two of them, $n^+(t)$ and $n^-(t)$, are time shifted subsets, and other two $n^0(t)$ are normal subsets. Then, the four split data sets are summed to form the inverse ratio spectrum $n(t)$,

$$n^+(t) = \dot{N}(t + \frac{\tau_a}{2}) \tag{7.2}$$

$$n^-(t) = \dot{N}(t - \frac{\tau_a}{2}) \tag{7.3}$$

$$n^0(t) = \dot{N}(t) \tag{7.4}$$

$$n(t) = n^+ + n^- + n^0 + n^0 \tag{7.5}$$

in which $\tau_a = 2\pi/\omega_a$ is an estimation of the spin precession period. The uncertainty of the estimated τ_a is very small, since ω_a has been measured with 0.7 ppm accuracy. After the exponential terms in $n(t)$ with $e^{(t+\frac{\tau_a}{2})/\gamma\tau}$ and $e^{(t-\frac{\tau_a}{2})/\gamma\tau}$ are expanded to the second order $\mathcal{O}(\tau_a/\gamma\tau)^2$, and the higher orders are ignored (see Appendix A for a detailed derivation of

the function as well as the more complicated version of Eq. 7.10), the inverse ratio function $n(t)$ becomes

$$n(t) = \frac{N_\circ(E_t)}{\gamma\tau} \cdot e^{-\frac{t}{\gamma\tau}} \cdot \left[1 + \frac{1}{16}(\frac{\tau_a}{\gamma\tau})^2 + \frac{1}{16}(\frac{\tau_a}{\gamma\tau})^2 A(E_t)\ \cos(\omega_a t + \phi(E_t))\right] \tag{7.6}$$

In practice, the value of τ_a is set to be 4.3654 μs, which is 0.3 ppm off the final f_a = 229 074.11 Hz in 2000 run and 2 ppm off to f_a = 229 073.59 Hz in 2001 run. The dilated lifetime $\gamma\tau$ is about 64.4 μs, but its exact value will be determined in this analysis. Using these numbers, the term associated with spin anomalous precession has a constant factor of $\frac{1}{16}(\frac{\tau_a}{\gamma\tau})^2 = \frac{1}{16}\left(\frac{4.365}{64.4}\right)^2 = 0.000287$. Effectively, the inverse ratio function reduces the effect of the anomalous spin precession by 10^4. It will turn out that the asymmetry term can be ignored in the function. Fig. 7.1 (a) shows an example of the (g-2) wiggle spectrum and Fig. 7.1 (b) is the inverse ratio time spectrum with one data set in 2001 run.

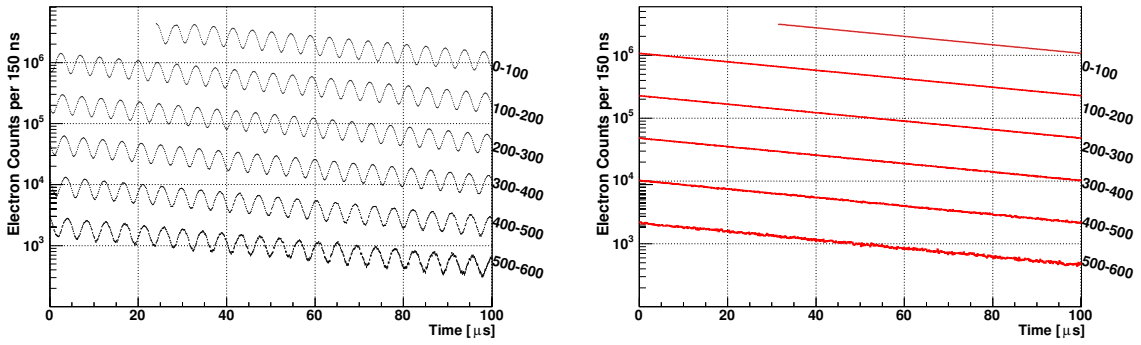

(a) (b)

Figure 7.1: (a) is the (g-2) ω_a spectrum or wiggle plot. (b) is the inverse ratio spectrum. The spectra from zero to 600 μs are plotted. The example spectra are from HB data set in 2001 data run.

The effects of beam dynamics and other backgrounds should also be included in the fitting function, specifically fast rotation $F(t)$ modulation, pileup events $P(t)$, background from the AGS $A(t)$, Coherent Betatron Oscillation $C(t)$, and slow effects $g_{slow}(t)$ which include muon losses $L(t)$. The detected electron spectrum can thus be described by the

general functional form

$$N_{full}(t) = [N(t) + P(t) + A(t)][1 + F(t)][1 + C(t)] \cdot g_{slow}(t) \tag{7.7}$$

The fast rotation modulation $F(t)$ is strong at early times after injection (see Chapter 6), and decreases with a time constant about 22 μs. In the dilated lifetime analysis, two methods are applied to remove the fast rotation modulation. One is the fill randomization during the histogram making stage prior to fitting, and another is to bin the histogram by the cyclotron period. The pileup events $P(t)$ are constructed based on the statistical method described in Sec. 5.4, and they are subtracted from the final spectrum. The coherent betatron oscillation $C(t)$ modulates the detector main acceptance $N(t)$, the asymmetry $A(E)$ and the spin precession phase $\phi(E)$. The remaining effect of significance is the muon loss term $L(t)$. Since the fitting for the lifetime starts late, after 45 μs, the AGS background $A(t)$ becomes negligible, especially in 2001 run.

The amplitude of the CBO modulation on the asymmetry $A(E_t)$ is almost an order smaller than that on the main acceptance. Therefore, this modulation is negligible in deriving the inverse ratio function, as is the CBO modulation on the (g-2) phase $\phi(E)$. The main acceptance is modulated by $A_N(t)$ which is given in Eq. 7.9. After the pre-processing of the histogram and simplification, the full physical function form used to describe the electron spectrum becomes

$$\dot{N}(t) = \frac{N_\circ(E_t)}{\gamma\tau} A_N(t) \cdot e^{-\frac{t}{\gamma\tau}} \cdot \Big[1 + A(E_t)\cos(\omega_a t + \phi(E_t))\Big] \cdot g_{slow}(t) \tag{7.8}$$

where $A_N(t)$ is the main acceptance modulation function,

$$A_N(t) = 1 + A_{CBO} \cdot g(t) \cdot \cos(2\pi f_{CBO} t + \phi_{CBO}). \tag{7.9}$$

The $g(t)$ is the CBO envelope form function. In this analysis, the CBO envelope form is given as an explicit exponential, $g(t) = e^{-t/\tau_{CBO}}$. The exponential form approximates the CBO envelope much better in the 2001 run than that in 2000 run. In both cases, the CBO term reduces the chi-square of the fitting, but does not change the fitted dilated

lifetime. The slow effect $g_{slow}(t)$ is mainly a muon loss function as in Eq. 7.12. The lost muons are re-constructed through the FSD triple coincidence as described in Sec. 5.6. The implementation of the muon loss into the fitting function is derived in Sec. 7.1.3 with more details in Appendix B.

After introducing the full physical function form into inverse ratio formula, expanding the exponential term, and keeping the leading orders of the small terms (see Appendix A for the step by step derivation), the expanded inverse ratio function becomes

$$\begin{aligned} n(t) &= \frac{N_\circ(E_t)}{\gamma\tau} e^{-\frac{t}{\gamma\tau}} \cdot \Big[1 + \frac{1}{16}(\frac{\tau_a}{\gamma\tau})^2 \\ &\quad + \frac{1}{16}(\frac{\tau_a}{\gamma\tau})^2 \; A(E_t) \; \cos(\omega_a t + \phi) \\ &\quad + A_{CBO} \cdot e^{-t/\tau_{CBO}} \; \cos(2\pi f_{CBO} t + \phi_{CBO}) \\ &\quad - A_{loss} \times IntLoss_{inv}(t) \Big] \end{aligned} \tag{7.10}$$

where $IntLoss_{inv}(t)$ is the inverse ratio version of integrated muon loss form, which is constructed from the integrated muon loss form $IntLoss(t)$ (see Eq. 7.15). Since the amplitude of A_{CBO} and A_{loss} are small, the cross terms with these parameters have been dropped in deriving Eq. 7.10. The muon loss functional form and the inverse ratio version of the muon loss form are described in Appendix B. The resulting function Eq. 7.10 is thus a mainly exponential decay function. For numerical stability, the phase parameters in the function are actually fitted using sine and cosine terms,

$$\begin{aligned} n(t) &= \frac{N_\circ(E_t)}{\gamma\tau} \; e^{-t/\gamma\tau} \cdot \Big[\; 1.0 + 2.87 \times 10^{-4} \\ &\quad + 2.87 \times 10^{-4} \; [N_{A_{cos}} \cos(\omega_a t) - N_{A_{sin}} \sin(\omega_a t)] \\ &\quad + e^{-t/\tau_{CBO}} \; [N_{A_{CBOsin}} \cos(2\pi f_{CBO} t) - N_{A_{CBOcos}} \sin(2\pi f_{CBO} t)] \\ &\quad - A_{loss} \cdot IntLoss_{inv}(t) \Big] \end{aligned} \tag{7.11}$$

7.1.1 Parameters and Minimization Procedure

There are total seven free parameters in the Eq. 7.11. They are listed as follows:

- $N_\circ(E_t)$: muon number in the ring
- $\gamma\tau$: muon dilated lifetime
- $N_{A_{sin}}$: sine amplitude from the anomalous spin precession
- $N_{A_{cos}}$: cosine amplitude from the anomalous spin precession
- $N_{A_{CBOsin}}$: sine amplitude of the acceptance modulation from CBO
- $N_{A_{CBOcos}}$: cosine amplitude of the acceptance modulation from CBO
- A_{loss}: muon loss normalization amplitude

The remaining parameters are fixed to their best known value. The g-2 frequency of $\omega_a = 2\pi/4365.4$ GHz is determined from the anomalous magnetic moment analysis. The CBO frequencies f_{CBO} are obtained from the Fourier transform of the residual spectrum (see Fig. 7.2 as an example), where the residue is the inverse ratio spectrum subtracted by an exponential decay function. The peak on the Fourier transform is fitted by a Gaussian function and the CBO frequency is taken as the mean of the Gaussian. This CBO frequency matches that from the 5-parameter fittings listed on Table 5.2 and is unique to each dataset. CBO also modulates the energy spectrum of the detected electrons. We can observe the CBO envelope by studying the energy spectrum as a function of time. In this analysis, the CBO envelope is approximated by an exponential decay function, and the decay constant τ_{CBO} is determined from the average electron energy spectrum which is modulated by the CBO effect. The actual τ_{CBO} value are listed in Table 5.2.

MINUIT [77] was used to perform the χ^2 minimization of the fitting. Fit start time could be chosen at an optimal value to balance the statistical uncertainty and the systematic error, but in this analysis, the statistical error on the fitted lifetime was inflated after including the muon losses in the function, so that we had to start the lifetime fitting as early as possible. The systematic error from the gain correction and pileup subtraction were tolerable at early times. The exact fitting start time will be discussed later. The fitting end time was chosen

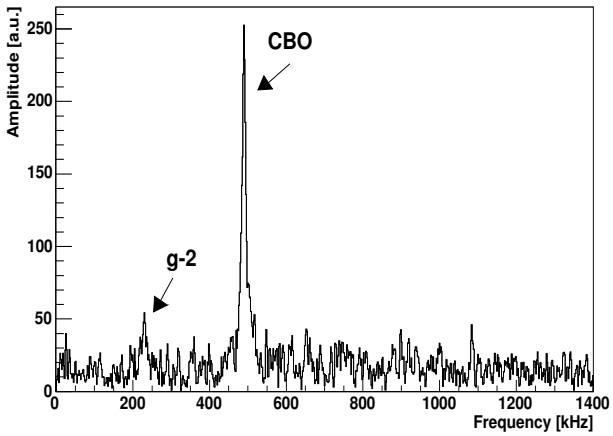

Figure 7.2: The Fourier transform of the residue of the inverse ratio spectrum after exponential function subtraction. CBO frequency peak is at 490 kHz for HB data set in 2001 run. The g-2 frequency component is reduced dramatically.

to be 600 μs, or the first time bin on the histogram whose electron counts were smaller than a critical number. This setting was chosen to ensure enough statistics in each bin of the histogram. The χ^2 minimization procedure requires that each bin in the fitting range have enough counts to approximate a Gaussian. The critical number was set to be 80, which was the same as that for ω_a analysis. This critical number condition was never reached because of sufficient data from the sum of all available detectors, therefore the fit end time was always 600 μs.

The fitting procedure calls "MIGRAD" in MINUIT to perform the minimization of the function. Migrad is the most efficient and complete single minimization method. The minimization produces the error matrix of the parameters as a by-product , which is usually reliable. After calling MIGRAD, a "MINOS" error analysis is performed which takes account of non-linearities in the parameters as well as parameter correlations. The error matrix is calculated by calling "HESSE" in MINUIT, which calculates the full matrix of second derivatives of the function with respect to the variable parameters. When minimization has converged, the "IMPROVE" procedure is called to start a search for any additional distinct

local minimum around the current local minimum of the function. Typically, three steps, including "MIGRAD", "HESSE", and "IMPROVE" are sufficient in a MINUIT fit. In some cases, a "MINIMIZE" procedure is called which uses MIGRAD to minimize the function, and switches to the "SIMPLEX" method if the MIGRAD fails to converge. Fortunately, the "MIGRAD" converges all the time for results shown in this analysis.

7.1.2 Fitting Results without Muon Losses

The exponential decay is the dominant term in the *inverse ratio* function which describes the muon decay. At later time after muon injection, this simple exponential function should be sufficient to be used to fit the detected electron time spectrum, except that the fitter returns the muon lifetime with a large statistical uncertainty. At early time after injection, we cannot ignore the CBO modulation and muon loss term in the fitting function, since without it, the fitter gives a unreasonable lifetime value with a large χ^2 on the fitting.

As shown on the left sides of Figs. 7.3 and 7.4, the lifetime fitted without including the muon loss do not shown stable behavior with respect to the fit start time in the 2000 run. For example, in the P1 data set, the fitted lifetime varies from 64225 ns to 64275 ns depending on the fit range, while the statistical uncertainty on the fit is less 5 ns. Even for the fit which starts as late as 100 μs, the fitted lifetime is 64275 ns, which is way off from the expected value based on other analysis, such as fast rotation. The fitted lifetimes without muon losses for all data sets are listed in Table 7.2 with the reduced χ^2 value. The fit starts at 47 μs after muon injection. The fitted lifetimes quoted at 100 μs are also inconsistent across the five different data sets without including muon losses.

The muon losses are smaller in general for the 2001 data. As a result, the fitted lifetime without muon loss is fairly stable over start time (see left side plots on Figs. 7.5 and 7.6). The fitted lifetimes without muon losses for the LB, LA, HB and HA are listed in Table 7.2 and the reduced χ^2. The lifetime results from four normal data sets are much closer to each other than those in 2000 run. The special data set SO under the scraping off condition

has large muon losses and the fitted lifetime (64171.9 $\pm$ 8.3 ns at 53 μs fit start time) is far away from the results of other data sets.

It is very clear that to fix these large discrepancies between the different data sets requires an extra physical term in the fitting function. Fortunately, the muon loss functional form can be approximated by the triple coincidences in the FSDs (see Sec. 5.6).

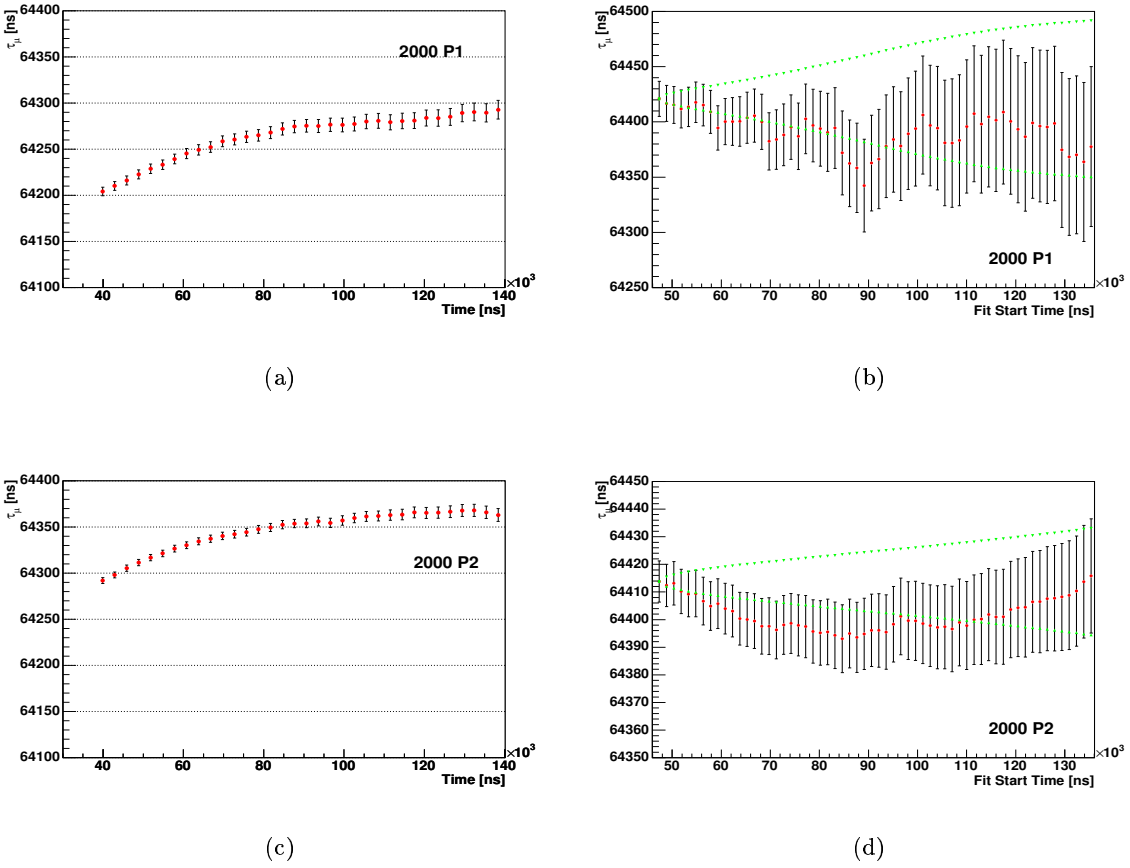

Figure 7.3: The start time scans of the lifetime fit without (left side) and with (right side) muon losses. The scans without muon loss term show poor stability of the fitted lifetime. Each point is a full fit, but starts the fit at the time given on the x-axis. Note that the lifetime scale is expanded on the right column of the figures.

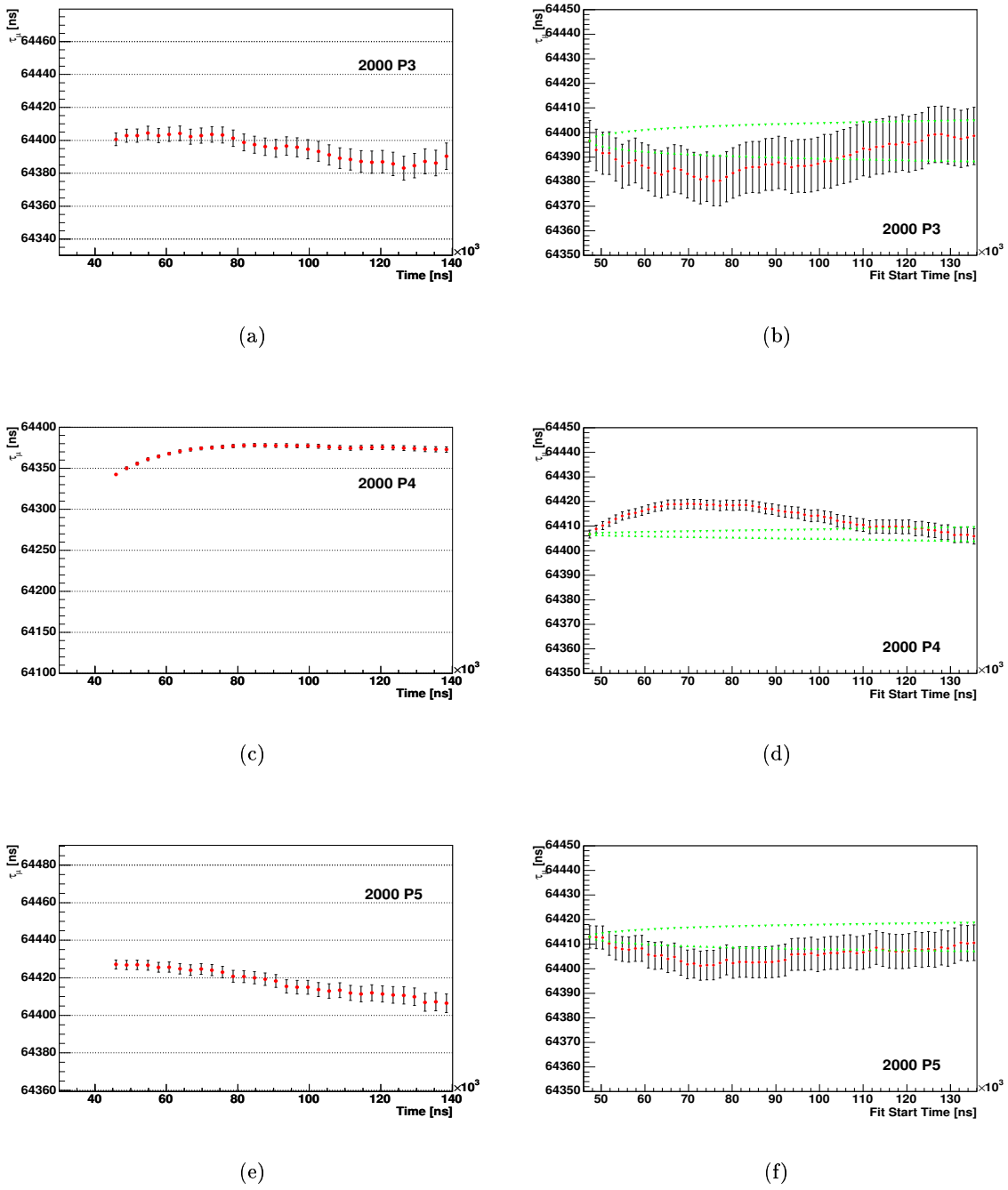

(a) (b)

(c) (d)

(e) (f)

Figure 7.4: The start time scans of the lifetime fit without (left side) and with (right side) muon losses. The scans without muon loss term show poor stability of the fitted lifetime. Each point is a full fit, but starts the fit at the time given on the x-axis. Note that the lifetime scale is expanded on the right column of the figures. (See Sec. 7.1.5 for the explanation on P4 data set)

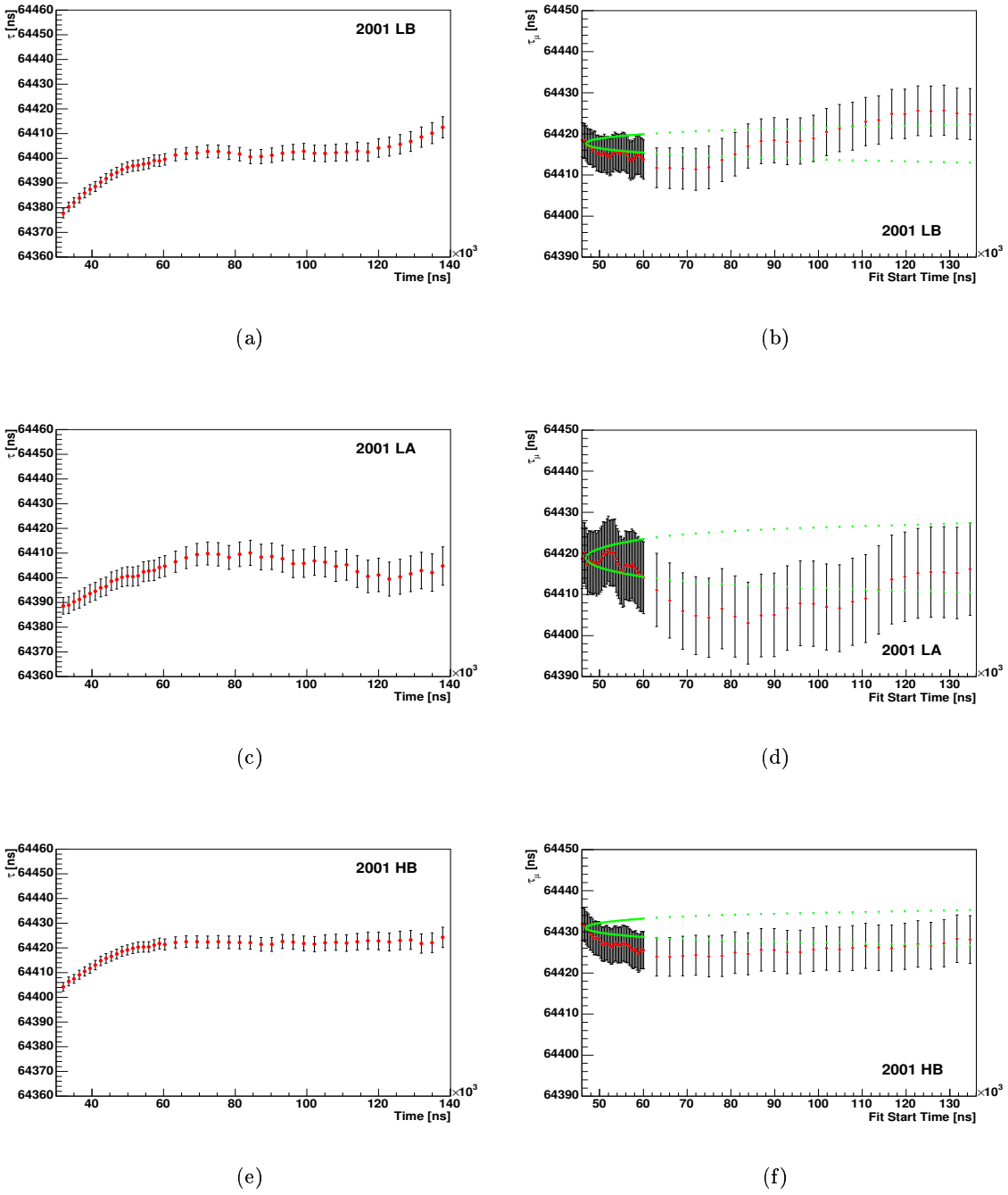

Figure 7.5: The start time scans of the lifetime fit without (left side) and with (right side) muon losses. The scans without muon loss term show poor stability of the fitted lifetime. Each point is a full fit, but starts the fit at the time given on the x-axis. Note that the lifetime scale is expanded on the right column of the figures.

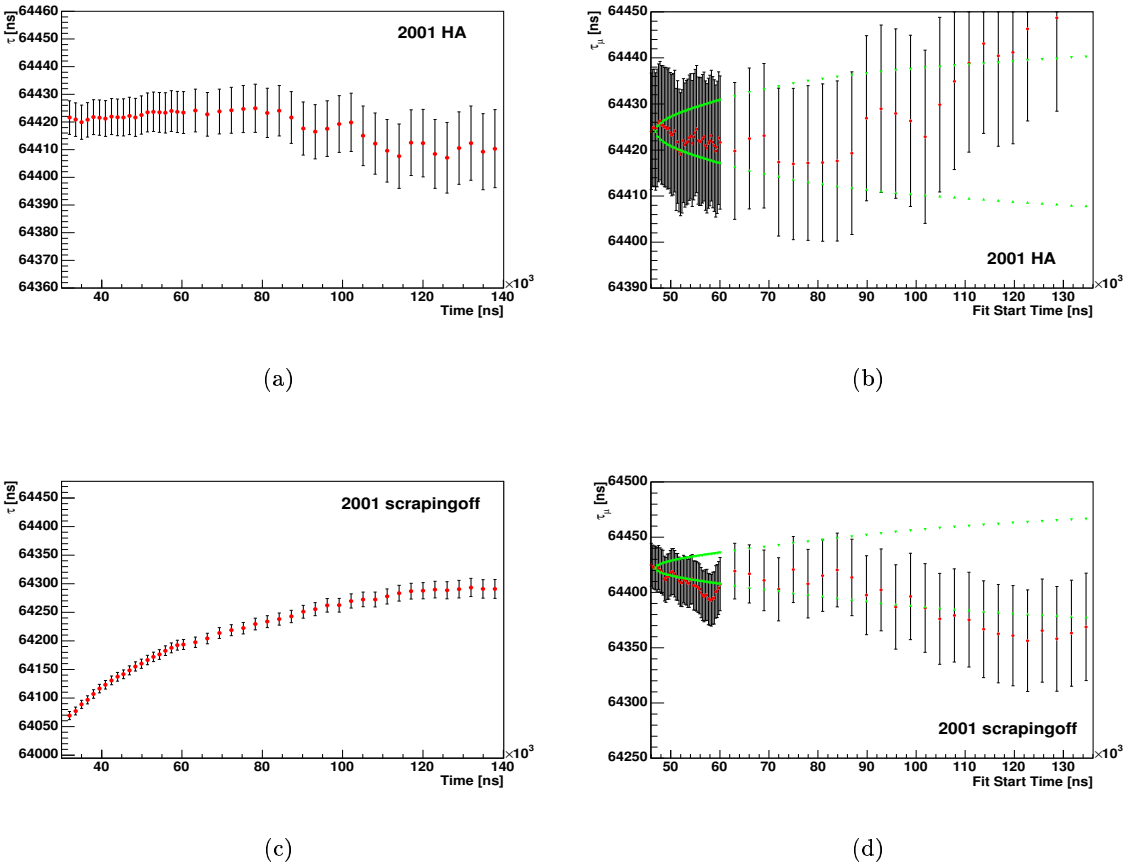

Figure 7.6: The start time scans of the lifetime fit without (left side) and with (right side) muon losses. The scans without muon loss term show poor stability of the fitted lifetime. Each point is a full fit, but starts the fit at the time given on the x-axis. SO data set has the most pronounced effect since it has the largest fraction by far of lost muons. Note that the lifetime scale is expanded on the right column of the figures.

7.1.3 Implementation of Muon Losses

The muon losses are so important that it is impossible to perform a muon lifetime measurement without having some reliable knowledge about it. As derived in Appendix B, the muon losses in the slow effect term are implemented in the integral form:

$$g_{slow}(t) = 1.0 - A_{loss} \times IntLoss(t) \tag{7.12}$$

$$IntLoss(t) = \int_{t_0}^{t} L(t')\, e^{t'/\gamma\tau}\, \mathrm{d}t' \tag{7.13}$$

where $L(t)$ is the reconstructed triple coincidence in FSDs, and t_0 is the earliest time when all FSDs are gated-on. $\gamma\tau = 1/\lambda_\mu$ is the nominal dilated lifetime, which has to be assumed beforehand in order to perform the integration. Its value is taken to be 64.400 μs. The integrated muon losses from time t_0 to time t is weighted by $e^{t/\gamma\tau}$. If $N_\mu(t_0)$ is the total muon number at time t_0, then the total injected muon number at $t = 0$ is $N_\circ = N_\mu(t_0)e^{t_0/\gamma\tau_\mu}$. Replacing the expression of $N_\circ$ in the exponential decay form gives

$$N_\mu(t) = N_\mu(t_0)e^{-(t-t_0)/\gamma\tau_\mu}\Big[1 - A_{loss} \times IntLoss(t)\Big] \tag{7.14}$$

In the analysis, t_0 was chosen to be 40 μs for the 2000 run, because the PMTs of FSDs were gated on later to avoid the flash. t_0 was 15 μs for the 2001 run. Multiplying the integrated loss functional shape at time t by the amount of loss, A_{1oss}, gives the total muon loss number. For the multi-parameter function, $IntLoss(t)$ is the loss form which enters into the fitting function. The integrated muon losses are plotted in Fig. 7.7 (a, b) for all 2000 and 2001 data sets.

To apply the integrated loss form into the *Inverse Ratio* fitting function, we have to construct an inverse ratio version of the loss term $IntLoss_{inv}(t)$ from the integrated loss $IntLoss(t)$. Inherited from the inverse ratio method, the $IntLoss_{inv}(t)$ (Eq. 7.15) consists of four sub sets at the first order approximation (see Appendix B for the derivation).

$$IntLoss_{inv}(t) = \int_{t_0}^{t} L(t')\, e^{\lambda_\mu t'}\, \mathrm{d}t' + \frac{1}{4}\int_{t}^{t+\tau/2} L(t')\, e^{\lambda_\mu t'}\, \mathrm{d}t' - \frac{1}{4}\int_{t-\tau/2}^{t} L(t')\, e^{\lambda_\mu t'}\, \mathrm{d}t' \tag{7.15}$$

The $IntLoss_{inv}(t)$ of all data sets in the 2000 and 2001 run are shown in Fig. 7.7 (c, d) with the value normalized to one at time 325 μs. The form of the function $IntLoss_{inv}(t)$ is input into the fitting function multiplied by a free parameter A_{loss}. This is because the FSD triple coincidence counter only captures a small portion of the muons which are lost. The re-constructed FSD triple coincidence is also station-dependent. More triples are detected near the kicker area (detector 8, 9, 10) than other azimuthal position. This

is one of the reason that this lifetime analysis uses the sum data from all FSD detectors. The measurement efficiency is very small and depends on the muon loss mechanism. An efficiency factor A_{loss} is the free fitting parameter in the function.

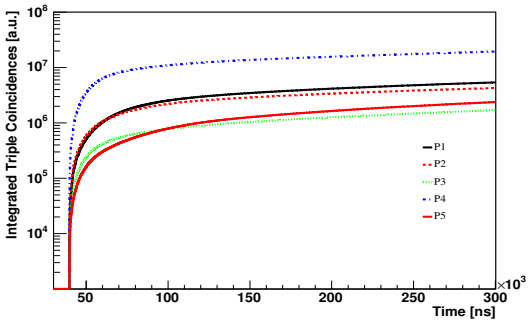

(a) 2000

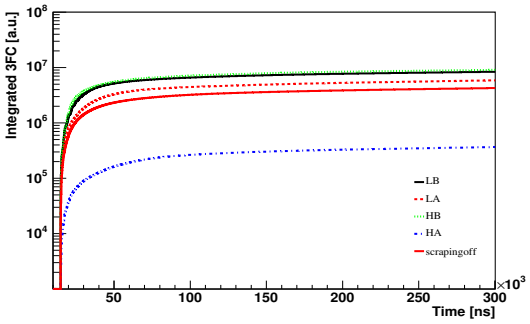

(b) 2001

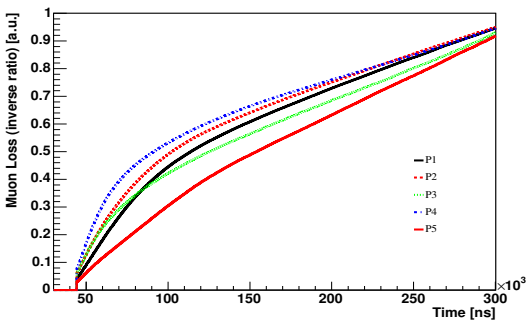

(c) 2000

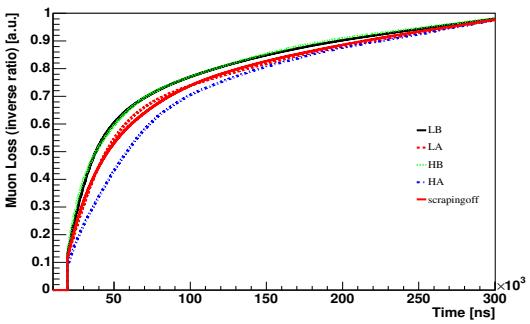

(d) 2001

Figure 7.7: The top plots are the integrated triple coincidences recorded by FSDs ($IntLoss(t)$) for five data sets in 2000 run (a) and five data sets in 2001 run (b). The bottom plots represent muon loss function forms in the Inverse Ratio method ($IntLoss_{inv}(t)$) for all data sets in the 2000 (c) and 2001 (d). For comparison purpose, the loss function is normalized to the value at 325 μs.

We know that the beam scraping at early times after muon injection reduces the muon losses at later time (see Sec. 3.3.4). For all the normal data sets, the scraping procedure was applied. In 2001, a set of special systematic study runs were performed to study the muon loss in the low quadrupole voltage setting after radial magnetic field change. Scraping off

runs (labeled as SO) have much higher differential muon loss rate than normal data sets. From Fig. 5.12, it is clear that at early time after injection (about 50 μs), the ratio of the lost muon to electron number is about 0.4%, and dropping off to $\sim$ 0.04% at 200 μs, whereas SO has more than seven time larger losses than those normal data sets at 50 μs.

The muon loss form works very well in the fitting to compensate the huge losses. It stabilizes the start time scan even for the scraping off data as seen by comparing Fig. 7.6 (c) and (d). The muon loss on the other four normal data sets are small comparing to the scraping off data.

7.1.4 Fitting Results

The final results are based on the sum data from all available detectors in order to apply the muon loss form which is combined from all triple coincidence sets. Table 7.1 shows the correlation matrix of all fitting parameters in the inverse ratio function. It is very clear that the muon loss normalization term A_{loss} is correlated with the muon number N (98.7%) and the lifetime $\gamma\tau$ (90.2%) at the quoted time. This strong correlation between the muon loss form and the electron spectrum introduces a big statistical uncertainty on the muon lifetime $\gamma\tau$. By allowing the muon loss normalization factor to float, the statistical uncertainty inflates by a factor of 2 or more compared to fixing muon loss or indeed to a fit which does not include muon loss at all. Fig. 7.8 shows the dilated lifetime of five data sets in the 2000 run for the sum of all available detectors. A fit start time of 47.4 μs is chosen since it is the earliest time at which all detectors are gated on and the χ^2/ndf of fit are consistent with one in the 2000 run. Fig. 7.9 shows the dilated lifetime of four normal data sets and one scraping off data set in the 2001 run. The chosen fit start time is 53 μs for 2001, when the χ^2/ndf on the start time scan are consistent with one for all data sets (see Sec. 7.1.5). Table 7.2 lists the final lifetime values which are plotted in Figs. 7.8 and 7.9. The χ^2/ndf values of the inverse ratio fit are consistent with 1 and the actual values

Parameter	N	$\gamma\tau$	$N_{A_{sin}}$	$N_{A_{cos}}$	$N_{A_{CBOsin}}$	$N_{A_{CBOcos}}$	A_{loss}
N	1.000	0.861	0.021	0.022	0.016	0.015	0.987
$\gamma\tau$	0.861	1.000	0.012	0.014	0.008	0.010	0.902
$N_{A_{sin}}$	0.021	0.012	1.000	0.000	0.012	0.017	0.020
$N_{A_{cos}}$	0.022	0.014	0.000	1.000	-0.021	0.002	0.020
$N_{A_{CBOsin}}$	0.016	0.008	0.012	-0.021	1.000	-0.005	0.015
$N_{A_{CBOcos}}$	0.015	0.010	0.017	0.002	-0.005	1.000	0.014
A_{loss}	0.987	0.902	0.020	0.020	0.015	0.014	1.000

Table 7.1: Correlation matrix from the fit to the sum of detectors in LB data set starting at 53 μs with all parameters being free. The muon loss normalization term is 98.7% correlated with the total muon N, and 90.2% correlated with $\gamma\tau$.

are listed on the table. The dilated lifetime averaged over all data sets for positive muon is

$$\tau_{\mu^+} = 64408.4 \pm 2.3 \text{ ns} \tag{7.16}$$

For negative muons, we get an average dilated life of

$$\tau_{\mu^-} = 64421.0 \pm 2.8 \text{ ns} \tag{7.17}$$

Year	Data Set	W/O Losses [ns]	χ^2/ndf	W/ Losses [ns]	χ^2/ndf
2000 μ^+	P1	64 219.4 ± 4.9	1.076±0.023	64 420.92 ± 15.88	1.031 ± 0.023
	P2	64 308.4 ± 3.3	1.099±0.023	64 413.77 ± 7.46	1.038 ± 0.023
	P3	64 401.7 ± 3.9	1.033±0.023	64 396.61 ± 8.27	1.033 ± 0.023
	P4	64 346.3 ± 1.6	1.308±0.023	64 406.71 ± 3.01	1.115 ± 0.023
	P5	64 427.0 ± 2.4	1.033±0.023	64 412.94 ± 4.52	1.031 ± 0.023
2001 μ^-	LB	64 397.2 ± 2.2	1.023±0.023	64 415.32 ± 4.49	1.018 ± 0.023
	LA	64 400.8 ± 4.0	1.025±0.023	64 420.20 ± 8.05	1.023 ± 0.023
	HB	64 420.3 ± 2.1	1.006±0.023	64 426.47 ± 4.27	1.005 ± 0.023
	HA	64 423.7 ± 7.1	1.003±0.023	64 421.08 ± 13.49	1.003 ± 0.023
	SO	64 171.9 ± 8.3	1.061±0.023	64 411.05 ± 21.65	1.015 ± 0.023

Table 7.2: Fitted lifetime without/with muon losses for five data sets in the 2000 run, four normal data sets and one scraping off data set in the 2001 run. The average dilated lifetime is 64408.4 ± 2.3 ns for the 2000 data, and it is 64421.0 ± 2.8 ns for the four normal data sets in the 2001 run.

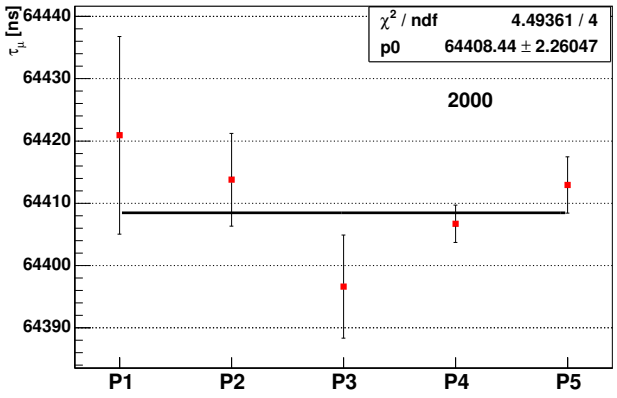

Figure 7.8: The dilated lifetime of positive charged muons in 2000 run. Five data sets are separated according to the experimental running condition. The results are for the fitting start time of 47.4 μs.

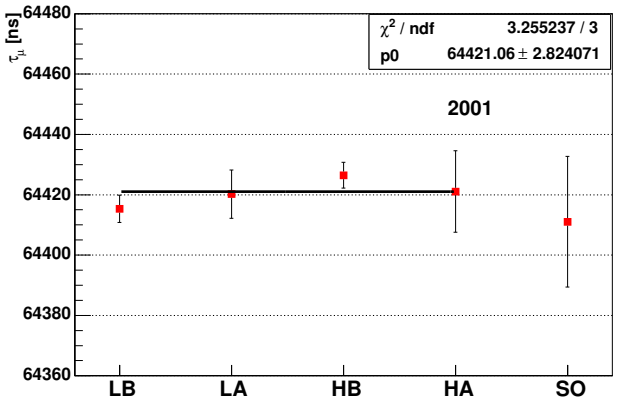

Figure 7.9: The dilated lifetime of negative charged muons in the 2001 run. Four normal data sets are used to make an average value. Scraping off data set is shown for comparison. The results are for the fitting start time 53 μs.

7.1.5 Start Time Variations

The final values are quoted from the earliest possible fitting start time, which gives the smallest statistical uncertainty on the dilated lifetime. When the fitting function correctly describes the data, we expect to see that all the fitting parameters are consistent with respect to the fit start time. This correlation band corresponding to the τ_μ parameter is shown as a sidewrap parabola in the right column of Figs. 7.3, 7.4, 7.5 and 7.6. The full set of fitting parameters (τ_μ, N, A_{loss}, A_{cbo} and A_{g-2}) are shown in Appendix D. They are plotted as a function of fit start time. The reduced χ^2 from the fit is also plotted with respect to the fit start time. The plots are for the sum of all available detectors in each data set. On each plot, the allowed one σ error bands are drawn.

All parameters behave as expected in the full physical function fitting. From the first fit start time up to 140 μs after injection, the τ_μ parameters are in the one σ error bands for most of data sets, except for the P4 data set in 2000 data which will be discussed later. For example, Fig. 7.4 (b) shows the fit start time scan of the dilated lifetime for P1 dataset. The τ_μ parameter of P1 data set is in the allowed one σ error bands. P1, P2, P3 and P5 data sets in 2000 and all data sets in 2001 are stable across start times.

The P4 data set behaves differently from other data sets. When the muon loss normalization factor A_{loss} is allowed to float in the fitting, the fitted dilated lifetime from the P4 data sets is not stable as shown in Fig. 7.10 (a). The fitted τ_μ value is $\sim$ 64406 ns at 47 μs with the $A_{loss} = (5.2711 \pm 0.1940) \times 10^{-3}$, and the fitted dilated lifetime decreases gradually as fit start time increases. At the same time, A_{loss} also decreases, getting close to zero at late times (see Fig. 7.10 (b)). To understand this problem, the P4 data were split into two equal sub parts, but the fitted results resembled those on Fig. 7.10. The loss form of data set P3 was used to replace the loss form of P4 itself, but the lifetime scan results remained unstable. The only way to stablize the parameters was to fix A_{loss} to one value, here chosen to be at 47 μs (see Fig. 7.11).

The muon loss normalization factor A_{loss} indicates what fraction of muons are lost from

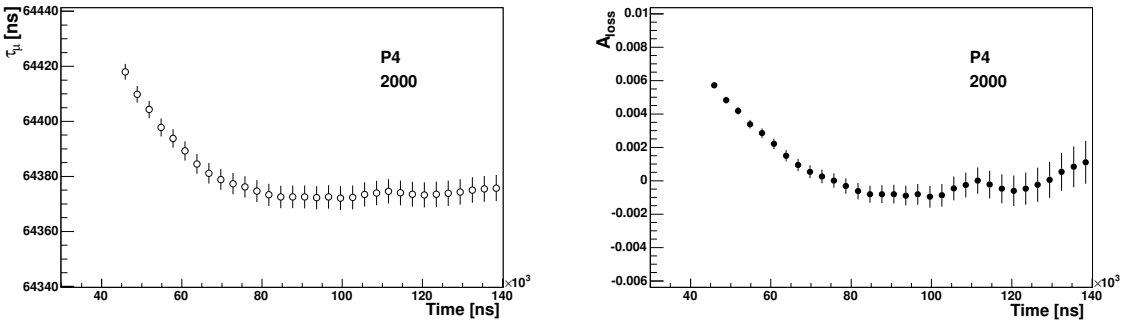

(a) (b)

Figure 7.10: The lifetime dependence (a) of the start time scan for P4 data set in the 2000 run is correlated with the A_{loss} parameter (b). The muon loss normalization parameter has been left free in the fitting.

the ring. It must be a positive number in principle. But, as seen in Fig. D.5, A_{loss} from the P5 data set has a negative value. It does not mean that muons entered the storage ring nonphysically. During the experiment in 2000, the FSD profiles were studied and the muon beam center was determined to be 2 mm high in the storage region, which caused large muon losses. The P5 data set was after the radial magnetic field adjustment to lower the beam height. This adjustment reduced the muon losses by a factor of ten (see Fig. 5.11). In the smaller muon loss situation, other residual slow effects compete with the muon loss in the fitting and cause a negative A_{loss}. In the case of large muon loss, although the same competition exists, the loss form function is significant and takes a dominant role in the fitting.

The reduced χ^2 of the fit is about 1.03 ± 0.02 for most data sets, except for P4, in the 2000 run, and 1.01 ± 0.02 in the 2001 run at the quoted fitting time with the full physical function. Without the muon loss form in the fitting function, the χ^2 is 1.05 ± 0.02 or higher in the same fitting range. It is 1.08 ± 0.02 for the anomalous P4 data set.

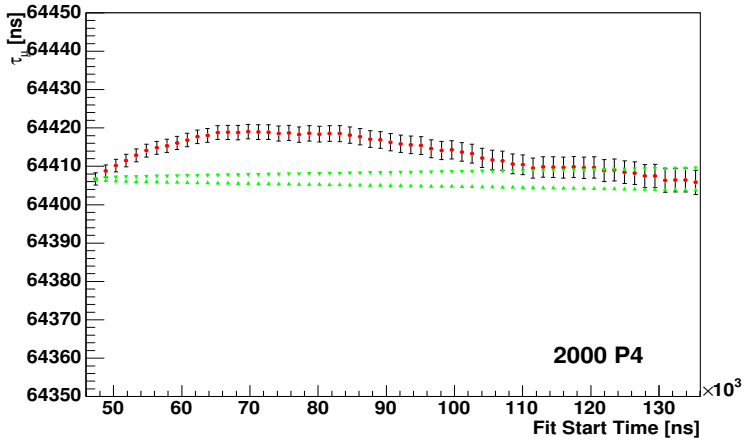

Figure 7.11: Start time scans of τ_μ in the dilated lifetime fit for P4 data set in 2000 run by fixing the A_{loss} with value at 47 μs.

7.2 Systematic Uncertainties on the dilated Lifetime

Muon losses are the most significant source of systematic uncertainty when they are not included in the fitting function. Fortunately, the triple coincidences from FSDs give a good approximation to the form of the muon loss, and the constructed muon loss form is known very well after applying the random coincidence subtraction and the FSD dead-time correction. The remaining systematic uncertainty come from the sources: (1) the muon acceptance, i.e. the proper normalization between the triple coincidence and the muon losses, (2) any muon loss shape variations, (3) lost protons in the 2000 run, and (4) the arbitrary time constant used to construct the integrated losses, such as nominal dilated lifetime. The other systematic uncertainties come from the imperfect gain correction, pileup subtraction and CBO amplitude and CBO frequency. The CBO related systematic uncertainties are very small.

7.2.1 Systematic Uncertainty from Muon Acceptance

The muon acceptance accounts for the largest systematic uncertainty from the muon losses in the dilated lifetime analysis. The FSD triple coincidences represent the correct muon loss shape, but we are lack of knowledge about the detector acceptance of the lost muons, which can also depend on upstream scattering from azimuthally-specific sources, such as the kicker or quadrupoles. The acceptance factor is contained within both the fitted muon loss normalization factor A_{loss} and the differential muon loss rate (see Fig. 5.11 and Fig. 5.12 for the differential muon loss).

In order to determine whether or not the fit to A_{loss} did a job of modeling the differential loss determined from the FSD triple coincidence to calorimeter electron ratio, Fig. 7.12 shows the correlation between A_{loss} and differential loss rate (see Table 7.3 for the value of each point). We define parameter r^2 as in Eq. 7.18, which represents the correlation between the fitted A_{loss} and the differential muon loss rate from the FSD triples.

$$r^2 = \sum_{i=1}^{N} \frac{\left(D_i - (A_i - \bar{A} + \bar{D})\right)^2}{\sigma^2} \tag{7.18}$$

where $\bar{A}$ is the average of the individual fitted loss factor A_{loss} over all data sets, and $\bar{D}$ is the average of the differential loss rate D_i. N is the total data set number, N=5 for 2000 run and N=4 for 2001 run. The scraping off data set was excluded from the calculation for 2001 data. By considering the statistical uncertainty on the differential loss rate D_i and the loss normalization factor A_{loss} from fit, the σ was calculated as $\sigma^2 = \sigma_A^2 + \sigma_D^2 + \sigma_{sys}^2$. The extra systematic uncertainty σ_{sys} is introduecd to the A_{loss} such that the correlation between the fitted A_{loss} and the differential loss is complete. When $\sigma_{sys} = 0.0008$, then r^2/N is close to one for all data sets (N=9) including 2000 and 2001 run. We form the parameter separately for the two year data sets, then we have $\sigma_{sys} = 0.008$ for 2000 data (N=5), where $\bar{A} = 0.0011$ and $\bar{D} = 0.0017$, and $\sigma_{sys} = 0.0006$ for 2001 data (N=4) where $\bar{A} = 0.00076$ and $\bar{D} = 0.0012$.

DataSet	Loss rate	Integrated Loss Rate	A_{loss}
P1	0.0069 ± 0.0005	0.0029	0.0168 ± 0.0012
P2	0.0060 ± 0.0002	0.0024	0.0075 ± 0.0005
P3	0.0036 ± 0.0003	0.0012	-0.0004± 0.0005
P4	0.0071 ± 0.0001	0.0026	0.0053 ± 0.0005
P5	0.0005 ± 0.0001	0.0005	-0.0011± 0.0003
LB	0.0042 ± 0.0001	0.0013	0.0034 ± 0.0007
LA	0.0039 ± 0.0001	0.0011	0.0034 ± 0.0012
HB	0.0023 ± 0.0001	0.0009	0.0011 ± 0.0007
HA	0.0019 ± 0.0002	0.0009	-0.0003± 0.0015
SO	0.0148 ± 0.0004	0.0069	0.0345 ± 0.0028

Table 7.3: The quoted differential loss rate is the ratio of FSD triples to electrons numbers at 50 μs, and the integrated loss rate is the ratio of FSD triples for electrons number integrated between 50 μs and 600 μs. The A_{loss} is the fit result.

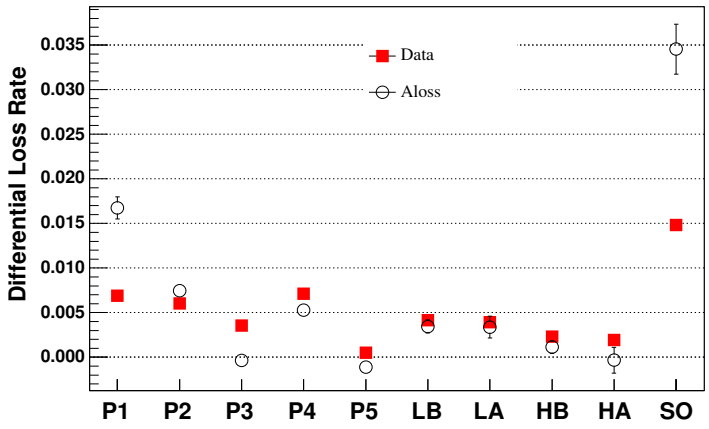

Figure 7.12: The differential loss rate D_i (closed square) and the fitted A_{loss} parameter A_i (open circle) are strongly correlated across the data sets. In order to achieve better correlation between D_i and A_i, an extra systematic uncertainty $\sigma_{sys} = 0.0008$ on A_{loss} is expected for 2000 data, and $\sigma_{sys} = 0.0006$ for 2001 data.

The estimation of the σ_{sys} is based on the differential muon loss rate at the actual fit start time. An estimation based on the integrated muon loss rate from 47 μs to 600 μs shows the exact same results for σ_{sys} except that the $\bar{D}$ values are 0.0019 for 2000 and 0.0010 for the 2001 run.

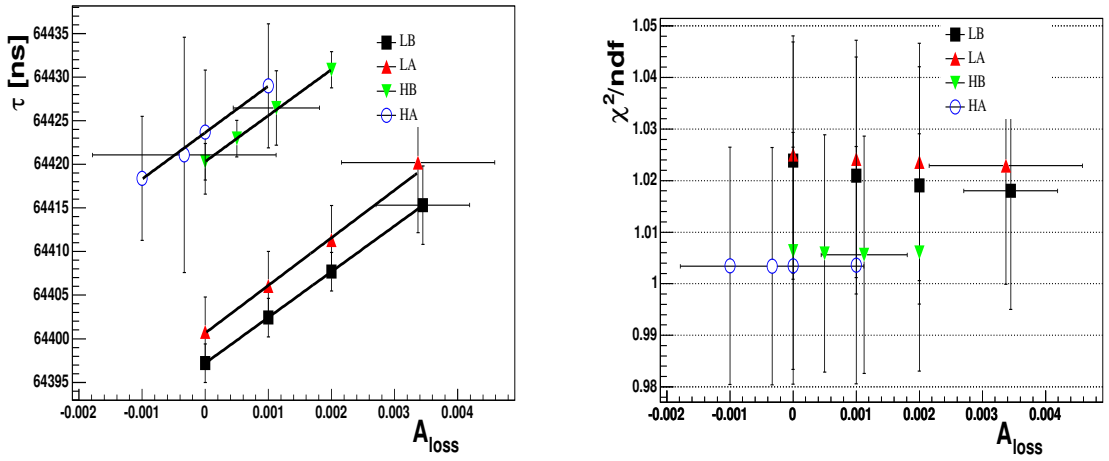

(a) (b)

Figure 7.13: The fitted dilated lifetime increases linearly as a function of the muon loss normalization factor, while χ^2 generally stays the same, making it impossible to use a χ^2 minimization procedure to fine-tune A_{loss}.

The amplitude of the muon loss normalization factor A_{loss} affected the fitted dilated lifetime value linearly. Fig. 7.13 (a) shows that the dilated lifetime increases linearly as a function of the muon loss fraction A_{loss}, where the A_{loss} was fixed to a set of values in the fit (A_{loss} was fixed only in the systematic study). χ^2 did not vary significantly as shown in Fig. 7.13 (b), making it impossible to use a χ^2 minimization procedure to fine-tune A_{loss}. The slopes for different data sets on Fig. 7.13 (a) were almost same at 5.27 ns $\times 10^3$/(unit A_{loss}) for the 2001 data, (slightly larger for the 2000 data). The uncertainty on the dilated lifetime was thus estimated to be $\delta\tau = \sigma_{sys} \times 5.27$ ns $\times 10^3$, giving $\delta\tau = 3.16$ ns for 2001 data, ($\delta\tau = 4.21$ ns, for 2000 data). This gave an upper limit to the systematic uncertainty

from muon loss.

7.2.2 Systematic Uncertainty from Muon Loss Shape

The systematic uncertainty from the muon loss shape is relatively small compared to that from the muon acceptance. The shape of the muon loss is similar enough to be summed together from the available FSD triple coincidences in the ring. In 2001, there were ten FSD triple combinations from 14 FSD stations, and seven triple combinations from 11 FSD stations in 2000. Each individual FSD triple combination (muon monitor) reconstructs its own lost muons. The muon monitors near the kicker region reconstruct more lost muons than do the monitors at the quiet side of the ring. For example, monitor 9-10-11 (from consecutive FSD stations 9, 10 and 11) reconstructs about five times more lost muon than monitor 23-24-1 to 300 μs. At late time (after 300 μs), the reconstructed triples in each individual monitor are very few. In Fig. 7.14 (a), the integrated lost muons from all available

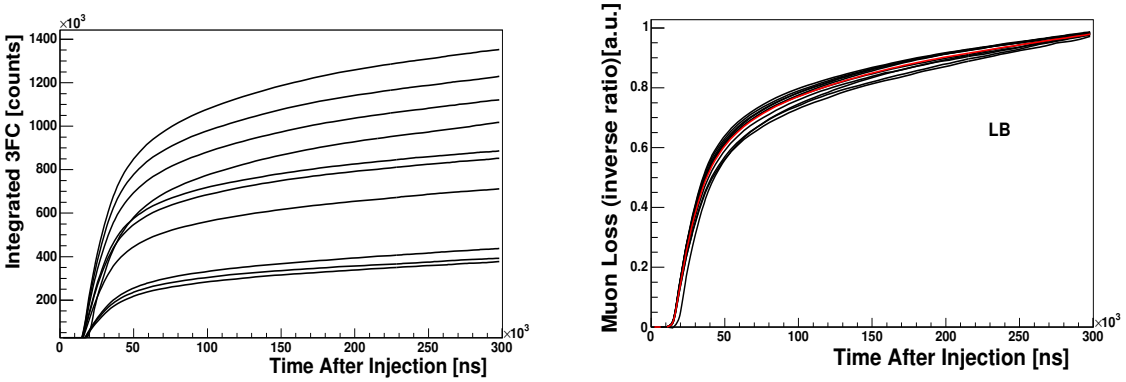

(a) (b)

Figure 7.14: An example from the LB data set in 2001 shows that the integrated triple coincidences depends on the azimuthal position of the muon monitor. From top to bottom on (a) are the integrated triples from the consecutive FSDs, which start at the station listed as 9, 11, 10, 8, 13, 12, 14, 22, 21 and 23. The top to bottom sequence on (b) is 13, 12, 11, 10, 9, 14, 21, 8, 22 and 23 and represents the integrated loss shape used in the inverse ratio method fit ($IntLoss_{inv}(t)$) normalized to the value at 325 μs.

monitors are shown for LB data in the 2001 run. The muon losses from the 9-10-11 monitor is at the top and the 23-24-1 is at the bottom. For comparison, the inverse ratio version of the integrated muon loss shape is shown in Fig. 7.14 (b) (the curves are normalized to the value at 325 μs).

The muon loss form used to do the fitting is the sum of all the individual FSD shapes. To understand what systematic uncertainty is introduced by the shape differences in the muon monitors, we replace the sum by an individual shape and see how much the fitted lifetime changes. Fig. 7.14 (a) shows the integrated FSD triple coincidences for all available muon monitors from a typical data set LB in the 2001 run. The large spreading on the integrated triple events indicates the azimuthal dependence of the lost muon. While Fig. 7.14 (b) shows the range of possible muon loss shapes. The top curve on Fig. 7.14 (b) is from FSD 13-14-15, and the bottom is from FSD 23-24-1. When the top curve replaces the sum muon loss form, the dilated lifetime becomes $\tau_{13} = 64415.10 \pm 4.44$ ns, whereas the bottom curve gives a dilated lifetime of $\tau_{23} = 64415.50 \pm 4.54$ ns. The difference between the upper and lower bounds is $\delta\tau = 0.4$ ns, which is quoted as the maximum systematic uncertainty for LB data set from the shape variation of the muon loss form. The same study was done to other data sets, and the results of this systematic uncertainty are same.

7.2.3 Systematic Uncertainty from Lost Protons

The triple coincidences from the consecutive FSDs in 2000 are more complicated than those in 2001. In 2000, the beam injected into the muon storage ring contained 10% protons. These protons were stored in the ring with the muons. The amount of protons was equivalent to one third of the muons stored in the ring at the beginning. Since protons do not decay, their portion in population of the particles remaining in the ring increased with time after injection. The way for the protons to leave the stored particle population was to hit an objects in the ring and got lost. Since the energy cut was only enforced on the first of three consecutive detector stations, the lost protons were included in the lost muon

time spectrum. The lost proton spectrum was made during the construction of the muon losses (see Sec. 5.6). The proton spectrum thus became a correction to the muon loss form. Since the inverse ratio fitting to the data was sensitive to the shape of the muon losses, we had to apply the correction in the fitting, which meant the muon loss shapes were allowed to adjust within an error band. The error band was determined from the uncertainty in the proton correction. As in reference [71], the loss shape was actually allowed to vary by a multiple of this error band,

$$L_\mu(t) = L_{FSD}(t) + \alpha L_p(t) \tag{7.19}$$

where $L_\mu(t)$ is the actual lost muon shape, $L_{FSD}(t)$ is the constructed triple coincidences, L_p is the constructed proton spectrum, and α is the correction factor. Since the corrections are additive, the inverse ratio version of muon loss form $IntLoss_{inv}(t)$ becomes

$$IntLoss_{\mu-inv}(t) = IntLoss_{inv}(t) - \alpha\ IntLoss_{p-inv}(t) \tag{7.20}$$

The inverse ratio version of the lost proton form $IntLoss_{p-inv}(t)$ was constructed as that of lost muon $IntLoss_{inv}(t)$ in Eq. 7.15. Fig. 7.15 shows the dilated lifetime and χ^2/ndf

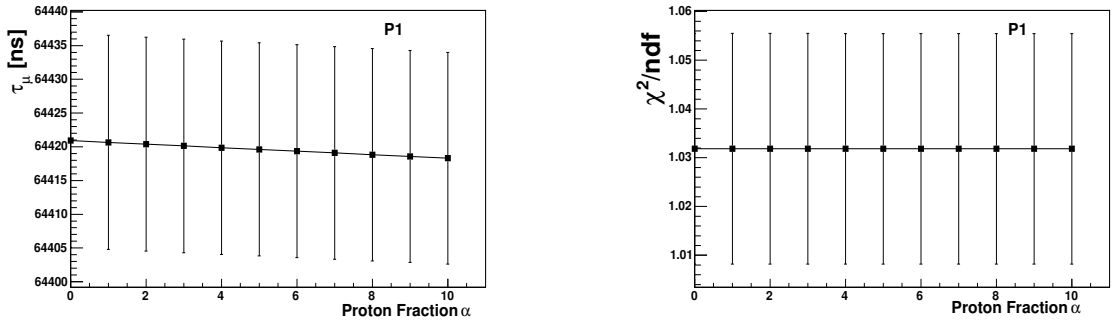

(a) (b)

Figure 7.15: (a) is the dilated lifetime versus the proton correction factor for P1 data set as an example. (b) is the χ^2/ndf for the fit.

changing with the proton fraction α for the P1 data set. We set the α from 0 to 10 and

let A_{loss} parameter be free in the fitting. The dilated lifetime changes linearly with α, while the χ^2/ndf does not vary much. Since the estimated proton number was about one twentieth of lost muons at early time (see Fig. 5.9), the maximum difference between $\alpha = 0$ and $\alpha = 10$ is quoted as the maximum possible systematic uncertainty[1]. Other data sets have the similar results, but with smaller changes. The values are 2.60 ns, 0.70, 0.05 ns, 0.03 ns, and 0.01 ns for five data sets in the 2000 run. The weighted average uncertainty $\delta\tau_{proton} = \sum_{i=1}^{5} \delta\tau_i \times N_i / \sum_{i=1}^{5} N_i$, where N_i is the electron number in i^{th} data set, from the lost proton correction is $\delta\tau_{proton} = 0.7$ ns for the 2000 data.

7.2.4 Uncertainty from Nominal Dilated Lifetime

The other source which effects the loss form in the fitting function is the nominal dilated lifetime in constructing the integrated muon loss form. When calculating the weighted muon loss at time t, we assumed the nominal dilated lifetime to be 64400 ns in the weight factor $e^{-t/\gamma\tau}$. This value differs to the fitted lifetime from each data set. To estimate the uncertainty, the fitted value from each data set is applied to the make the new integrated muon loss form. The dilated lifetime difference from the fitting using these two versions of the integrated loss form is assigned to be the systematic error. Among all data sets in both 2000 and 2001 run, the HB data set shows the biggest difference between the fitted lifetime 64426 ns and the nominal lifetime. Using the newly constructed muon loss form for HB, the fitted lifetime and χ^2 remain the same value, but the normalized muon loss factor A_{loss} moves from 1.12696 to 1.127218. Consequently, the systematic uncertainty from the nominal lifetime can be ignored.

Combining all the sources of systematic uncertainty related the muon loss in Sec. 7.2.1, Sec. 7.2.2, Sec. 7.2.3 and Sec. 7.2.4, the final uncertainties from the muon loss are $\delta\tau_{loss} =$ 4.25 ns for 2000 run, and $\delta\tau_{loss} = 3.16$ ns for 2001 run, which are listed in Table 7.6.

[1] The optimized value is $\alpha = 2.53$ from F. Gray [71].

7.2.5 Systematic Uncertainty from Pileup Subtraction

The average inefficiency of the pileup subtraction is 3.4 percent [71]. This inefficiency should be the upper limit for the muon lifetime analysis for a fitting start time of 53 μs. This figure is used to quantify the systematic error. Normally, the decay electron histograms are subtracted by the constructed pileup spectrum. To find the sensitivity of muon lifetime to the pileup subtraction, the electron spectra with and without pileup subtraction are fitted. The change of the lifetime versus the pileup subtraction factor is defined as the sensitivity. An example is shown on Fig. 7.16 with all slopes listed in Table 7.4.

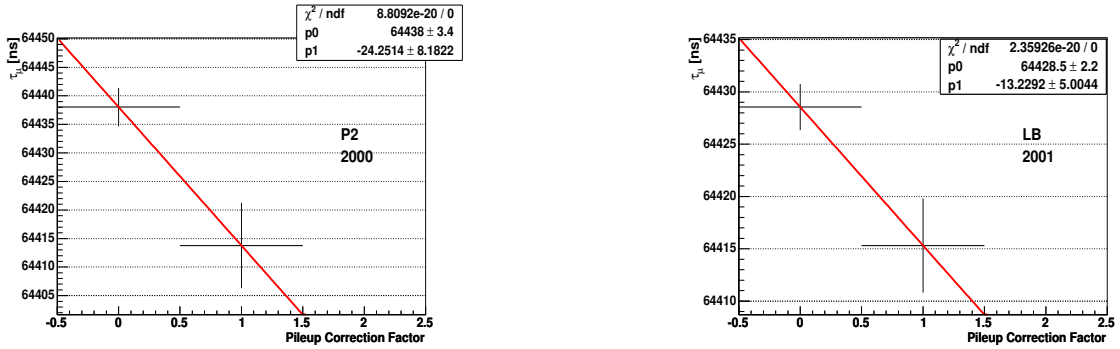

(a) (b)

Figure 7.16: Lifetime τ_μ for fits with and without pileup subtraction. 0 means no-pileup-subtraction applied, and 1 means normal pileup subtraction. The slope is the sensitivity factor. The slopes of all data sets are listed in Table 7.4.

The average sensitivity of lifetime to the pileup subtraction is 28.55 ns per unit pileup subtraction. Multiplying the pileup subtraction inefficiency 3.4%, the systematic error from pileup subtraction for 2000 data becomes $\delta\tau = 22.38 \times 3.4\% = 0.76$ ns. The average sensitivity of lifetime to the pileup subtraction is 14.27 ns/(unit of pileup). Multiplying the pileup subtraction inefficiency 3.4%, the systematic error of the pileup inefficiency for the 2001 run is $\delta\tau = 14.27$ ns $\times\ 3.4\% = 0.49$ ns.

Year	Run Period	slope (ns/unit pileup)
2000	P1	6.97
	P2	24.25
	P3	14.35
	P4	28.55
	P5	14.05
	Average	22.38
2001	LB	13.23
	LA	13.84
	HB	15.04
	HA	14.96
	Average	14.27

Table 7.4: Sensitivity of the lifetime to pileup subtraction factor in the 2000 and 2001 run. The value is quoted at the normal fit start time.

7.2.6 Gain Correction

The stability of the energy and time measurements recovered from the calorimeter are key to the precision of the muon lifetime measurement. Although the gain correction was applied during the histogram filling stage (see Sec. 5.3), a systematic bias could occur if the gain was not fully correct.

The average energy for the sum of all detectors was uniform with respect to time after injection after the gain correction was applied to each individual detector. The uncertainty in the uniformity was shown in Fig. 7.18 (b) for the 2001 data. The linear fit from 50 μs to 300 μs shows that the slope $(-7.46 \pm 4.74) \times 10^{-8}/\mu$s was consistent with zero. We estimated the uncertainty of the flatness to be $\delta E = 4.74 \times 10^{-8}/\mu s \times 250\ \mu\text{s} = 1.2 \times 10^{-5}$. The normalized average energy on the sum of detectors before the gain correction was $E = 0.9998$, which was 2.0×10^{-4} away from 1.0 at 50 μs (See Fig. 5.5 black dots). Since the gain was converted from the average energy, the gain correction uncertainty was

$$\frac{\delta G}{G} = \frac{\delta E}{1 - E} = \frac{1.2 \times 10^{-5}}{2.0 \times 10^{-4}} = 0.06 = 6\% \tag{7.21}$$

To find the figure of merit of the gain correction, the fitted lifetimes at 53 μs were

extracted for the data with different amounts of gain correction applied. There were three different cases. No gain correction, one time gain correction, and five times gain correction were applied to the data. The slope of the linear fits on the fitted lifetime versus gain correction factor (0, 1, and 5) were listed in Table 7.5 and shown in Fig. 7.17 for two examples. The $\delta G/G = 6\%$ is the level of confidence of the gain correction after 53 μs. The

Year	Run Period	slope (ns/unit gain)
2000	P1	18.12
	P2	16.80
	P3	16.53
	P4	16.76
	P5	16.47
	Average	16.94
2001	LB	5.40
	LA	5.12
	HB	5.65
	HA	5.23
	Average	5.39

Table 7.5: Sensitivity of the lifetime to gain correction factor in the 2000 and 2001 run. The value is quoted at the normal fit start time.

systematic uncertainty from this gain correction is $\delta\tau = 5.39$ ns $\times$ 0.06 = 0.33 ns for the 2001 data.

The average energy could also shift by a fraction because of the pileup subtraction inefficiency. For an energy range of 1.8-3.2 GeV, the fractional change was about 0.002 [51]. This value was multiplied by the pileup subtraction inefficiency of 3.4%. Since the fit started at 53 μs, the final fraction value was $0.002 \times 3.4\% \times e^{-53/64.4} = 3.07 \times 10^{-5}$. This fraction will introduce $\delta\tau = 5.39$ ns $\times \frac{3.07\times10^{-5}}{2.0\times10^{-4}} = 0.83$ ns systematic uncertainty on the dilated lifetime. Since these two parts of the systematic errors from the gain correction were not completely correlated, they were added in quadrature to give a total uncertainty for 2001 data of $\delta\tau = \sqrt{0.33^2 + 0.83^2} = 0.89$ ns. This uncertainty from gain correction entered into Table 7.6.

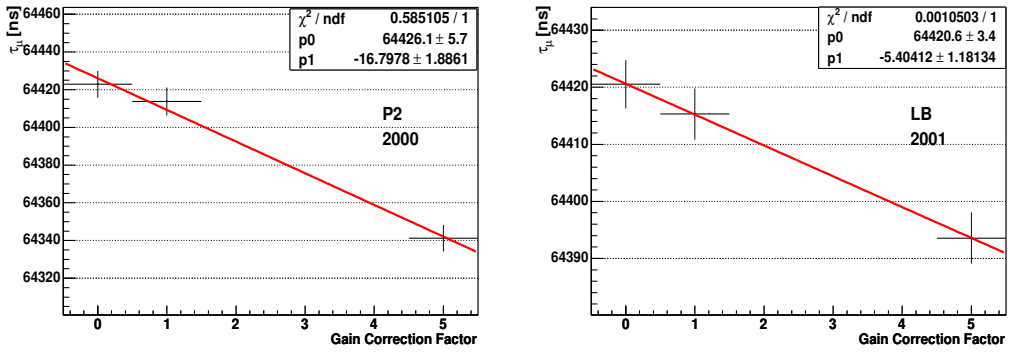

(a) (b)

Figure 7.17: Example of the fitted lifetime τ_μ with different gain factor applied on electron energy correction. 0, 1, and 5 times gain correction were applied. Zero means no-gain-correction applied. The slopes of all data sets are listed in Table 7.5.

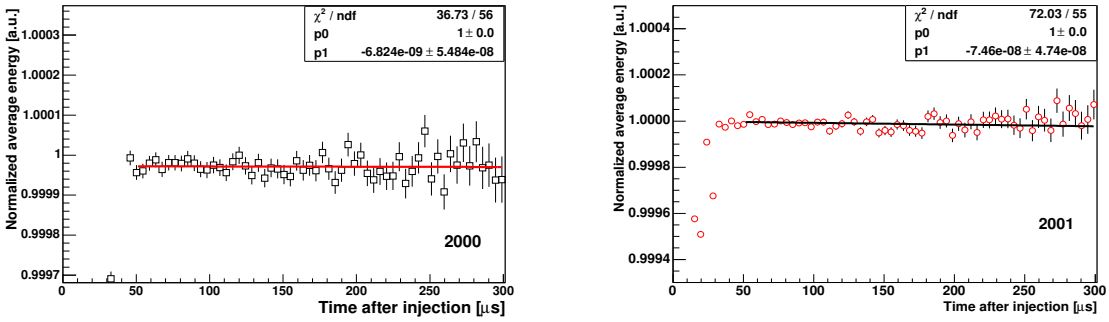

(a) (b)

Figure 7.18: The uncertainty on the gain correction. The average energy is supposed to be flat after the gain correction is applied. The linear fit shows that the slope is consistent with zero for both 2000 run (a) and 2001 run (b).

The average energy before the gain correction for the sum of detectors in the 2000 data is shown in Fig. 7.18 (a). The average energy after the gain correction in the 2000 data shows a slope of $(-0.68 \pm 5.48) \times 10^{-8}$. Then the $\frac{\delta G}{G} = 7\%$ for the 2000 run. Following the same procedure detailed above for 2001, the gain correction uncertainty is 16.98 ns $\times$ 0.07 = 1.19 ns. Thus the uncertainty of gain correction by the pileup subtraction inefficiency is 16.98 ns $\times \frac{3.07\times10^{-5}}{2.0\times10^{-4}} = 2.61$ ns. The total uncertainty for 2000 data is $\delta\tau = \sqrt{1.19^2 + 2.61^2} =$ 2.87 ns. This uncertainty from gain correction entered into Table 7.6.

7.2.7 Coherent Betatron Oscillations (CBO)

Recall that the Coherent Betatron Oscillation frequency and decay constants for each data sets were fixed in the fitting function. The resulting systematic error could be quantified as follows.

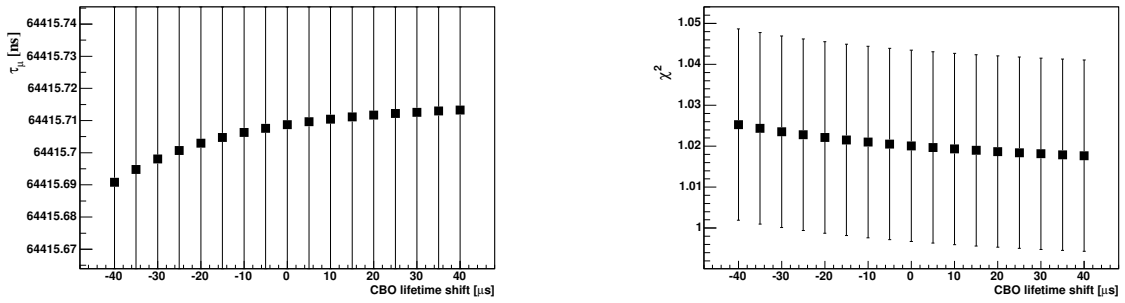

(a) (b)

Figure 7.19: Lifetime τ_μ changes as a function of the CBO envelope decay constant. The LB data set in 2001 run is used as example.

First, let us compare the lifetime results by fixing the different CBO lifetimes. If we fix the CBO frequency to its actual value and change CBO time constant by 5 μs per step from 40 μs to 40 μs, the change of the dilated lifetime was very small. See Fig. 7.19 for an example. The biggest possible change was less than 0.05 ns. All data sets in 2001 run had the same results.

The second systematic uncertainty from the CBO parameters came from the fixed CBO frequency. The CBO frequency was known from the Fourier transform of the residue spectrum of the basic (5-parameter) fitting function. The CBO frequency peak on the Fourier transform had an RMS width of ~ 0.20 kHz, whereas in the inverse ratio fitting function, the CBO frequency was fixed at its peak mean value. An example of the fitted dilated lifetime and its reduced χ^2 were shown in Fig. 7.20 for a set of CBO frequencies. The maximum difference was 0.10 ns when the CBO frequency was set to 1.0 kHz off from its mean value. All data sets in 2001 run had the same results.

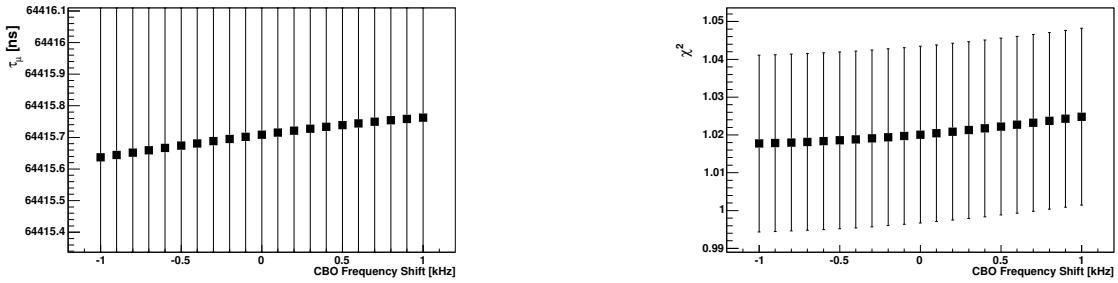

(a) (b)

Figure 7.20: Lifetime τ_μ change is small as a function of the fixed CBO frequency. The LB data set in the 2001 run is used as example.

The systematic uncertainty from the CBO parameters are small. Combining the uncertainty from CBO frequency and CBO lifetime linearly, we have the total uncertainty $\delta\tau = 0.05 + 0.10 = 0.15$ ns for the 2001 data. This uncertainty entered into Table 7.6.

The 2000 data sets behaved differently with respect to the CBO frequency and CBO envelope decay constants. The P1 data set was very sensitive to changes in the CBO envelope decay constant as shown in Fig. 7.21 (a-c). The variation of the dilated lifetime was about 1.36 ns for the P1 data set. For other data sets in the 2000 run, the variation was less than 0.20 ns for the CBO lifetime change (see Fig. 7.21 (d) for an example). An average systematic error from the CBO envelope lifetime was set to 0.4 ns. The systematic

uncertainty from the change of the CBO frequency for 2000 data was 0.4 ns. The total

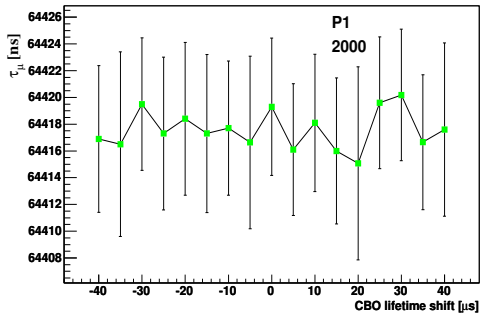

(a) τ_μ of P1

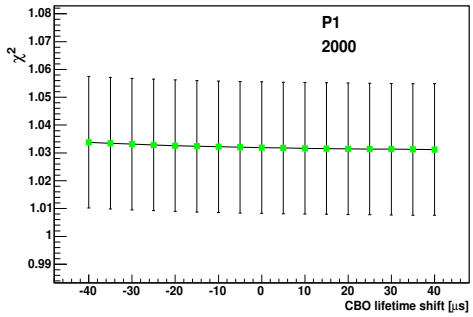

(b) χ^2/ndf of P1

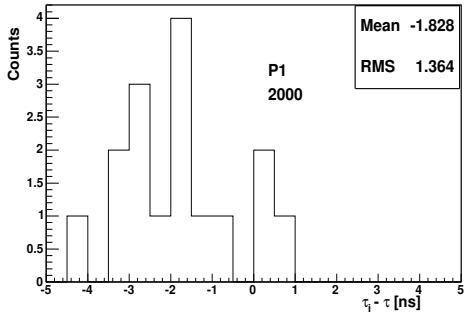

(c) τ_μ of P1

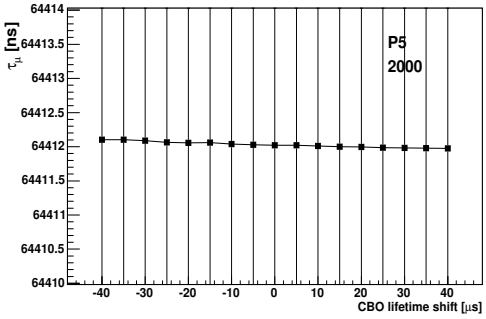

(d) τ_μ of P3

Figure 7.21: Lifetime τ_μ change as a function of the fixed CBO decay constant. The dilated lifetime has a much large variation with respect to CBO envelope decay constant only for P1 data set. The remaining data sets behaves similarly as P5 data set (d), which has small variation to the CBO lifetime change.

systematic uncertainty from CBO parameters was $\delta\tau = 0.4 + 0.4 = 0.8$ ns. This uncertainty entered into Table 7.6.

7.3 Summary of Systematic Uncertainties

Table 7.6 gives a summary of the systematic fitting uncertainties for the 2000 and 2001 data using the *Inverse Ratio* method. All errors correspond to the fits to the sum of the available

detectors. The uncertainty is averaged over all data sets in each year. Other systematic uncertainties, such as fitting uncertainty, histogram bin width, and fill randomization effects, are much smaller compared to the major effects listed in the table.

Source of Uncertainty	2000 Data Set [ns]	2001 Data Set [ns]
Muon losses	4.25	3.16
Gain stability	2.87	0.89
Pileup subtraction	0.76	0.49
Coherent betatron oscillations	0.80	0.15
Total Uncertainty	5.2	3.3

Table 7.6: Table of systematic uncertainties for the dilated lifetime fitting from both 2000 and 2001 data run.

Although we could achieve the statistical precision of 18 ppm in the lifetime for both μ^+ and μ^- without considering the muon losses (see Table 7.2 for the results without muon losses), the systematic uncertainties from the muon losses were the biggest concern in the experiment. After including the extra muon loss term in the fitting function, the statistical uncertainty on the fitted lifetime parameter was increased in a factor of two because of correlations between the muon loss shape and the exponential decay form of the stored muons. Since the lack of the absolute calibration for the lost muons forced us to fit for this correlated parameter (A_{loss}), this resulted in a substantially large systematic uncertainty on the final results. Any muon lifetime experiment associated with a future (g-2) experiment should have a dedicated muon counter to reduce the the systematic uncertainty.

Chapter 8

Conclusion

8.1 The Muon Lifetime At Rest

The final dilated lifetime τ_μ results, along with the special relativity gamma $\bar{\gamma}$ values, are listed in Table 8.1. Their ratio $\tau_0 = \frac{\tau_\mu}{\bar{\gamma}}$ gives the muon lifetime at rest for each sub data set, which is listed in the last column of the table. The statistical uncertainty on the dilated lifetime is quoted directly from the fit for each individual data set, while the systematic uncertainty is studied across the entire data in each year as summarized in Table 7.6. The systematic uncertainty on the dilated lifetime is 5.2 ns (81 ppm) for 2000 run, and 3.3 ns (51 ppm) for 2001 run. The statistical uncertainty of the gamma value $\bar{\gamma}$ is very small and can be ignored, since we have used sufficient fast rotation cycles in our analysis. The systematic uncertainty of the gamma value is evaluated for each data set (see Table 6.7), and the E-field correction has been included in the listed $\bar{\gamma}$ values. The systematic uncertainty of the gamma value for each data set is weighted by $\sigma_{stat,i}(\tau)$ to give the average uncertainty, which gives $\sigma_{syst}(\gamma) = 14$ ppm for the 2000 run, and $\sigma_{syst}(\gamma) = 13$ ppm for the 2001 run, respectively.

The statistical uncertainty on the lifetime at rest is dominated by the statistical uncertainty of the dilated lifetime. The weighted average of the lifetime at rest is calculated as

Year	Data	τ_μ [ns]	$\sigma_{stat}(\tau_\mu)$ [ppm]	$\bar{\gamma}$	τ_0 [ns]
2000 μ^+	P1	64 420.92	246	29.315 47	2 197.505
	P2	64 413.77	116	29.312 13	2 197.512
	P3	64 396.61	128	29.314 91	2 196.718
	P4	64 406.71	47	29.313 78	2 197.147
	P5	64 412.94	70	29.308 89	2 197.726
2001 μ^-	LB	64 415.32	70	29.312 91	2 197.507
	LA	64 420.20	125	29.313 44	2 197.633
	HB	64 426.47	66	29.313 92	2 197.811
	HA	64 421.08	209	29.312 77	2 197.713

Table 8.1: The dilated lifetime with the statistical uncertainty, the special relativity gamma values and the lifetime at rest in the 2000 and 2001 run are listed. The systematic uncertainty on the dilated lifetime is 5.2 ns (2000) and 3.3 ns (2001). The weighted average dilated lifetime is $\bar{\tau}_{\mu^+} = 64408.4 \pm 2.3$ ns for the 2000 data and $\bar{\tau}_{\mu^-} = 64421.0 \pm 2.8$ ns for the 2001 data. The systematic uncertainty on the gamma value $\sigma_{syst}(\gamma) = 14$ ppm and 13 ppm for 2000 and 2001 run, respectively.

$\bar{\tau}_0 = (\sum_{i=1}^{N} \tau_{0,i}/\sigma^2_{stat,i}(\tau))/\sum_{i=1}^{N} 1/\sigma^2_{stat,i}(\tau)$, where $\sigma_{stat,i}(\tau)$ is the statistical uncertainty on i^{th} data set (see Table 8.1) in unit of ppm. The estimated statistical uncertainty of the mean lifetime over the data sets is calculated with $\sigma^2(\tau_0) = 1.0/(\sum_{i=1}^{N} 1/\sigma^2_{stat,i}(\tau))$,

$$\tau_0^+ = 2\ 197.301 \pm (35 \text{ ppm statistical}) \pm (82 \text{ ppm systematic})$$

$$\tau_0^- = 2\ 197.665 \pm (44 \text{ ppm statistical}) \pm (53 \text{ ppm systematic})$$

where the systematic uncertainty from the dilated lifetime analysis and fast rotation analysis in quadrature $\sigma_{syst} = \sqrt{\sigma^2_{syst}(\tau_\mu) + \sigma^2_{syst}(\gamma)}$.

Combining the statistical and systematic uncertainty gives the final results for the positive and negative muon lifetime at rest measured in the BNL (g-2) experiment:

$$\tau_0^+ = 2\ 197.301 \pm 0.200 \text{ ns } (89 \text{ ppm})$$

$$\tau_0^- = 2\ 197.665 \pm 0.152 \text{ ns } (69 \text{ ppm})$$

Comparing to the previous CERN value, $\tau^+ = 2196.6 \pm 2.0$ ns and $\tau^- = 2194.8 \pm 1.0$ ns, this new measurements represent a factor of 9 improvement over previous CERN experiment results for μ^+ and a factor of 5 for μ^-.

The muon lifetime at rest from BNL (g-2) experiments are shown on Fig. 8.1 with previous experimental results. The new measurements are consistent with those from the muon stopping experiments, although the central value of τ_0^- is 2.8 sigma higher than the existing world average.

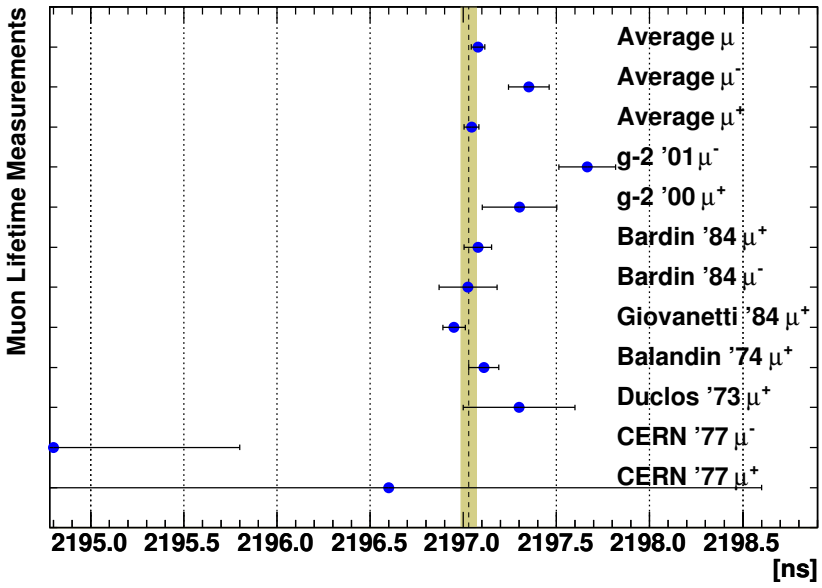

Figure 8.1: Muon lifetime measurements with the new values from BNL (g-2) experiment. The shadow area marks the one sigma error band around the existing world average with value $\tau_0 = 2197.03 \pm 0.04$ ns. The new world average values are not affected by the lifetime from previous CERN experiments because of their large uncertainty.

A new world average for the positive muon lifetime at rest with all the measurements since 1974 gives $\bar{\tau}^+_{0,world} = 2\ 197.044 \pm 0.039$ ns (18 ppm) which is still dominated by Giovanetti [9] and Bardin [8]. The new world average for the negative muon lifetime at rest is calculated by combining the results from Bardin [8] and this measurement, $\bar{\tau}^-_{0,world} = 2\ 197.351 \pm 0.109$ ns (49 ppm) Combining positive and negative muon lifetime results gives a new world average for the muon lifetime at rest $\bar{\tau}_{0,world} = 2\ 197.079 \pm 0.037$ ns (17 ppm) All these new world average values are plotted on Fig. 8.1 as well.

Based on the new muon lifetime value, we calculate the Fermi Coupling constant

$$G_F = (1.166\ 32 \pm 0.000\ 01) \times 10^{-5}\ \mathrm{GeV}^{-2}$$

where the 9 ppm uncertainty comes from the muon lifetime experimental uncertainty only, and central value is lowered by four sigma comparing to the current existing value.

The next generation of dedicated muon lifetime measurement is expected to reduce the uncertainty by at least a factor of ten [78]. The on-going experiment μLan at PSI led by researchers from (g-2) collaboration is aiming to measure the positive muon lifetime using a pulsed muon beam to a precision of 1 part in 10^6, which in the absolute scale is on the level of 2 picoseconds. This advance will reduce the Fermi Coupling Constant value to 0.5 ppm uncertainty level.

8.2 A Test of the Special Relativity

A test of special relativity is made by comparing the μ^+ lifetime in flight as measured by this experiment to that measured at rest. The best limit is obtained by using the μ^+, since its lifetime at rest is better determined experimentally. The positive muon lifetime measured at the rest is averaged over four experiments listed in Particle Data Book (DUCLOS 1973, BALANDIN 1974, GIOVANETTI 1984, BARDIN 1984) with $\tau_{\mu^+} = 2197.029 \pm 0.040$ ns,

$$\frac{\tau_{\mu^+} - \tau_0^+}{\tau_0^+} = (12.4 \pm 9.3) \times 10^{-5}$$

representing muons traveling at the speed of 0.999418c with $\bar{\gamma} = 29.31453$. For a 95% confidence level, the range is (-6.2 to 31.0)$\times 10^{-5}$.

By using the lifetime of negative muons from this analysis and lifetime at rest from Ref. [3] $\tau_{\mu^-} = 2197.025 \pm 0.155$ ns, we have

$$\frac{\tau_{\mu^-} - \tau_0^-}{\tau_0^-} = (29.1 \pm 11.0) \times 10^{-5}$$

Taking the mean of these two differences, the relativistic time transformation is shown to

be valid to $(20.0 \pm 10.1) \times 10^{-5}$. For a 95% confidence level, the range is (-0.2 to 40.2)$\times 10^{-5}$. These tests are 10 times better than those reported in CERN III experiment [17].

8.3 A Test of CPT Invariance

The CPT theorem states that, under very general conditions, a Lorentz invariant quantum field theory is invariant under the combined operations of charge conjugation, space inversion, and time reversal. The theorem was proposed by Pauli in 1955. For the Standard Model, the CPT theorem implies that, since CP is not a symmetry of the Model, then neither is time reversal T.

General principles of relativistic field theory require invariance under the combined transformation CPT. The equality of the lifetime of positive muon and its anti-particle, the negative muon, provides the simplest test of CPT invariance.

The lifetime ratio of positive and negative muons at rest is a basic test of CPT invariance. Using the lifetime from the BNL (g-2) experiments gives

$$\tau_{\mu^-}/\tau_{\mu^+} = 1.000165 \pm 0.000114$$

Combining the positive and negative muon lifetime in this analysis gives the average muon lifetime for this measurement $\tau_{average} = 2197.531 \pm 0.121$ ns. The ratio of the lifetime difference between the two particles to the mean lifetime is therefore

$$(\tau_{\mu^+} - \tau_{\mu^-})/\tau_{average} = (16 \pm 12) \times 10^{-5}$$

At 95% confidence level, the range is (-8 to 40)$\times 10^{-5}$.

Although the current mean life ratio value on the Particle Data Book [3] is $\tau_{\mu^+}/\tau_{\mu^-} = 1.000024 \pm 0.0078$, and $(\tau_{\mu^+} - \tau_{\mu^-})/\tau_{average} = (2 \pm 8) \times 10^{-5}$, these values were calculated by assuming CPT invariance in the first place [14] (see Sec. 1.2.2). Because of the difficulty in measuring the lifetime at rest for the negative muons, using the muon lifetime from the storage ring experiments is more appropriate to test the CPT invariance. Comparing to

the value from previous CERN III experiment, $\frac{\tau_{\mu^+}-\tau_{\mu^-}}{\tau_{\mu^+}} = (0.8 \pm 1.0) \times 10^{-3}$, our result is five time better than CERN III result.

Appendix A

Derivation of Inverse-Ratio Function

For a given detector, the time dependence of the number of observed electrons is determined by both the exponential decay of the muon and the anomalous muon spin precession at frequency ω_a. If we do not consider any beam dynamic effects and background, integrating over all energies above a certain threshold E_t gives the following form for the electron time spectrum

$$\dot{N}(t) = \frac{N_\circ}{\gamma\tau}(E_t) \cdot e^{-\frac{t}{\gamma\tau}} \cdot [1 + A(E_t)\cos(\omega_a t + \phi_a(E_t))] \tag{A.1}$$

This is so called Five-parameter function. Since the energy threshold E_t is greater than zero by the nature of the experiment, the asymmetry $A(E_t)$ will never be zero. The inverse ratio method is to minimize or even eliminate the effect of the anomalous spine precession term in Eq. A.1 in the final fitting function.

In the inverse ratio method, decay electrons having time spectra of the form $N(t)$ given in Eq. A.1 are randomly split into four subsets $n^+(t), n^-(t), n^0(t)$, and $n^0(t)$, then summed to form the inverse ratio spectrum $n(t)$

$$n^+(t) \quad = \quad \dot{N}(t + \frac{\tau_a}{2}) \tag{A.2}$$

$$n^-(t) = \dot{N}(t - \frac{\tau_a}{2}) \quad (A.3)$$

$$n^0(t) = \dot{N}(t) \quad (A.4)$$

$$n(t) = n^+ + n^- + n^0 + n^0 \quad (A.5)$$

in which $\tau_a = 2\pi/\omega_a$ is an estimation of the spin precession period. The uncertainty of the estimated τ_a is very small. The relative error on the τ_a is about 0.7 ppm [22] and [23].

After expanding the exponential term to the second order, and ignoring the higher orders, the inverse ratio function $n(t)$ becomes

$$n(t) = \frac{N_\circ(E_t)}{\gamma\tau} \cdot e^{-\frac{t}{\gamma\tau}} \cdot [1 + \frac{1}{16}(\frac{\tau_a}{\gamma\tau})^2 + \frac{1}{16}(\frac{\tau_a}{\gamma\tau})^2 A(E_t)\ \cos(\omega_a t + \phi_a(E_t))] \quad (A.6)$$

The value of τ_a is set to be 4.3654 μs, and the dilated lifetime $\gamma\tau$ is about 64.4 μs. Therefore, in this inverse ratio function, the effect of the anomalous spin precession has been reduced by 10,000 times.

In reality, we have to include the beam dynamics and other background effects in the fitting function. The full physical function has the following form,

$$\dot{N}(t) = \frac{N_\circ(E_t)}{\gamma\tau} A_N(t) \cdot e^{-\frac{t}{\gamma\tau}} \cdot \Big[1 + A(E_t)\cos(\omega_a t + \phi_a(E_t))\Big] \cdot g_{slow}(t) \quad (A.7)$$

where the functional forms are explained in the following,

- $A_N(t)$ is the main acceptance modulation function, which is dominated by the beam horizontal Coherent Betatron Oscillation (CBO) motion. A_{CBO} is the initial amplitude of the modulation. The amplitude decays as a function of time.

  $$A_N(t) = 1 + A_{CBO} g_{CBO}(t)\cos(2\pi f_{CBO} t + \phi_{CBO}) \quad (A.8)$$

  $g_{CBO}(t)$ is the CBO modulation time envelope function. Study shows that an exponential function is a good approximation for the CBO time envelope. $g_{CBO}(t) = e^{-t/\tau_{CBO}}$. The decay constant τ_{CBO} depends on the the electric quadurople high voltage setting.

- $g_{slow}(t)$ is the slow effects on the time spectrum. It should include the muon loss effect, detector gain correction and pileup subtraction. Since the gain correction and

pileup subtraction have been treated in the histogram building stage, the muon loss becomes the dominant part in this term.

$$g_{slow}(t) = 1 - A_{loss} \cdot IntLoss(t) \tag{A.9}$$

$$IntLoss(t) = \int_{t_0}^{t} L(t')\, e^{\lambda_\mu t'}\, \mathrm{d}t' \tag{A.10}$$

where $IntLoss(t)$ is the integrated muon loss spectrum $L(t)$. The $L(t)$ is the triple coincident muon events from muon counters. The implementation of the muon losses will be discussed in Sec. B.

- The asymmetry $A(E_t)$ also has a modulation effect from the CBO. As study shows that the applitude of the modulation is five time smaller than that on the A_N. Besides, $A(E_t)$ itself is small term. Therefore, this modulation is not considered. The some reason applies to the modulation of the g-2 phase term $\phi_a(E_t)$. The asymmetry $A(E_t)$ and phase $\phi_a(E_t)$ depend on the energy threshold E_t.

Now, let us derive the inverse ratio fitting function with these effects. For simplication, the energy dependence variable (E_t) in $N_\circ(E_t)$, $A(E_t)$, and $\phi_a(E_t)$ is omitted.

$$\begin{aligned}
n(t) &= n^0 + n^0 + n^+ + n^- \\
&= \frac{N_\circ}{\gamma\tau} A_N(t) \cdot e^{-\frac{t}{\gamma\tau}} \cdot \Big[1 + A\cos(\omega_a t + \phi_a)\Big] \cdot g_{slow}(t) \\
&\quad + \frac{N_\circ}{\gamma\tau} A_N(t) \cdot e^{-\frac{t}{\gamma\tau}} \cdot \Big[1 + A\cos(\omega_a t + \phi_a)\Big] \cdot g_{slow}(t) \\
&\quad + \frac{N_\circ}{\gamma\tau} A_N(t + \frac{\tau_a}{2}) \cdot e^{-\frac{t+\frac{\tau_a}{2}}{\gamma\tau}} \cdot \Big[1 + A\cos(\omega_a(t + \frac{\tau_a}{2}) + \phi_a)\Big] \cdot g_{slow}(t + \frac{\tau_a}{2}) \\
&\quad + \frac{N_\circ}{\gamma\tau} A_N(t - \frac{\tau_a}{2}) \cdot e^{-\frac{t-\frac{\tau_a}{2}}{\gamma\tau}} \cdot \Big[1 + A\cos(\omega_a(t - \frac{\tau_a}{2}) + \phi_a)\Big] \cdot g_{slow}(t - \frac{\tau_a}{2}) \\
&= \frac{N_\circ}{\gamma\tau} \cdot e^{-\frac{t}{\gamma\tau}} \Big[\Big[A_N(t) + A_N(t) A\cos(\omega_a t + \phi_a)\Big] \cdot g_{slow}(t) \\
&\quad + \Big[A_N(t) + A_N(t) A\cos(\omega_a t + \phi_a)\Big] \cdot g_{slow}(t) \\
&\quad + \Big[A_N(t + \frac{\tau_a}{2}) e^{-\frac{\tau_a}{2\gamma\tau}} + A_N(t + \frac{\tau_a}{2}) e^{-\frac{\tau_a}{2\gamma\tau}} A\cos(\omega_a t + \pi + \phi_a))\Big] \cdot g_{slow}(t + \frac{\tau_a}{2}) \\
&\quad + \Big[A_N(t - \frac{\tau_a}{2}) e^{\frac{\tau_a}{2\gamma\tau}} + A_N(t - \frac{\tau_a}{2}) e^{\frac{\tau_a}{2\gamma\tau}} A\cos(\omega_a t - \pi + \phi_a)\Big] \cdot g_{slow}(t - \frac{\tau_a}{2})\Big]
\end{aligned}$$

the next step is to expand the $e^{\frac{\tau_a}{2\gamma\tau}}$ term,

Again, by expanding the exponential term, and just keeping the leading orders in the small terms, the final inverse ratio function for the full physical function is given as

$$\begin{aligned} n(t) &= \frac{N_\circ(E_t)}{\gamma\tau} e^{-\frac{t}{\gamma\tau}} \cdot \Big[1 + \frac{1}{16}(\frac{\tau_a}{\gamma\tau})^2 + \\ &+ \frac{1}{16}(\frac{\tau_a}{\gamma\tau})^2 A(E_t)\ \cos(\omega_a t + \phi) + \\ &+ A_{CBO} \cdot e^{-t/\tau_{CBO}}\ \cos(2\pi f_{CBO} t + \phi_{CBO}) + \\ &- A_{loss} \times IntLoss_{inv}(t) \Big] \end{aligned} \tag{A.11}$$

where $IntLoss_{inv}(t)$ is the inverse ratio version of integrated muon loss function form, which is constructed from the $IntLoss(t)$.

$$IntLoss_{inv}(t) = \int_{t_0}^{t} L(t')\, e^{\lambda_\mu t'}\, \mathrm{d}t' + \frac{1}{4}\int_{t}^{t+\tau/2} L(t')\, e^{\lambda_\mu t'}\, \mathrm{d}t' - \frac{1}{4}\int_{t-\tau/2}^{t} L(t')\, e^{\lambda_\mu t'}\, \mathrm{d}t' \tag{A.12}$$

Noting that the amplitude of A_{CBO} and A_{loss} are small, the crossing terms with these parameters have been dropped in deriving the above function. The $IntLoss_{inv}(t)$ is the inverse ratio version of muon loss function. The muon loss function form and the inverse ratio version of muon loss form will be described in Sec. 7.1.3.

The resulting function Eq. A.13 is thus a mainly exponential function. The anomalous spin precession term is reduced by a factor of $\frac{1}{16}(\frac{\tau_a}{\tau_\mu})^2 = \frac{1}{16}\left(\frac{4.365}{64.4}\right)^2 = 0.000287$.

For numerical stability purpose, the phase parameters in the fitting function are fitted by the sine and cosine terms. The final function is defined as

$$\begin{aligned} n(t) &= \frac{N_\circ(E_t)}{\gamma\tau} e^{-t/\gamma\tau} \cdot \{\ (1.0 + 2.87 \times 10^{-4} \\ &+ 2.87 \times 10^{-4}\ (N_{A_{cos}} \cos(\omega_a t) - N_{A_{sin}} \sin(\omega_a t)) \\ &+ e^{-t/\tau_{CBO}}\ [N_{A_{CBOsin}} \cos(2\pi f_{CBO} t) - N_{A_{CBOcos}} \sin(2\pi f_{CBO} t)] \\ &- A_{loss} \times IntLoss_{inv}(t))\} \end{aligned} \tag{A.13}$$

Appendix B

Implementation of the Muon Loss in the Inverse-Ratio

As discussed in Appendix A, the slow effect $g_{slow}(t)$ includes the muon loss function, $g_{slow}(t) = 1 - A_{loss} \cdot IntLoss(t)$. The $IntLoss(t)$ is related to the observed muon loss time spectrum $L(t)$. In this section, I will rederive the implementation of the function form. This derivation is also in reference [70].

For the total $N_\mu(t)$ muons stored in the storage ring at time t, the $\mathrm{d}N_\mu(t)$ muons will decay into electrons in $\mathrm{d}t$ time interval.

$$\frac{\mathrm{d}N_\mu(t)}{\mathrm{d}t} = -\lambda N_\mu(t) \tag{B.1}$$

Here, we ignore the muon precession at this moment. The $\mathrm{d}N_\mu(t)$ is equal to the detected electron number in $\mathrm{d}t$ interval. The decay constant $\lambda = \frac{1}{\tau_\mu}$. This is for the perfect experimental condition. The solution gives

$$N_\mu(t) = N_0 e^{-(t-t0)/\tau_\mu} \tag{B.2}$$

In reality, there are some muons lost from the storage ring without decay. Let us assume that $\mathcal{L}(t)$ muons being lost at time t. Therefore, the muons which disappear from the storage

ring includes the decayed muons and lost muons,

$$\frac{\mathrm{d}N_\mu(t)}{\mathrm{d}t} = -\lambda N_\mu(t) - \mathcal{L}(t) \tag{B.3}$$

where $\mathcal{L}(t)$ is assumed to be proportional to the observed three-fold coincidence $L(t)$ in the FSDs. $\mathcal{L}(t) = aL(t)$. The constant a is to account for the acceptance coefficience of the three-fold coincidence.

The general solution to the ordinary differential equation $\frac{\mathrm{d}N_\mu(t)}{\mathrm{d}t} = -\lambda N_\mu(t) - aL(t)$ is

$$N_\mu(t) = e^{-\lambda(t-t_0)}[\int_{t_0}^{t} e^{\lambda t'}(-aL(t'))\mathrm{d}t' + b] \tag{B.4}$$

The initial condition is that at $t = t_0$, there are $N_\mu t_0$ muons. So, $b = N_\mu(t_0)$.

$$N_\mu(t) = N_\mu(t_0)e^{-\lambda(t-t_0)}[1 - a\int_{t_0}^{t} e^{\lambda t'}L(t')\mathrm{d}t'] \tag{B.5}$$

$$g_{loss}(t) = 1.0 - A_l' \frac{\int_{t_0}^{t} L(t')\, e^{\lambda_\mu t'}\, \mathrm{d}t'}{\int_{t_0}^{t_{max}} L(t')\, e^{\lambda_\mu t'}\, \mathrm{d}t'} \tag{B.6}$$

where t_{max} is set to be the time such that after time t_{max}, the measured losses $L(t)$ does a little to change the integral form. The value of t_{max} is chosen to 325 μs, in most of cases.

In the inverse ratio formula, the loss form becomes

$$IntLoss_{inv}(t) = \int_{t_0}^{t} L(t')\, e^{\lambda_\mu t'}\, \mathrm{d}t' + \frac{1}{4}\int_{t}^{t+\tau/2} L(t')\, e^{\lambda_\mu t'}\, \mathrm{d}t' - \frac{1}{4}\int_{t-\tau/2}^{t} L(t')\, e^{\lambda_\mu t'}\, \mathrm{d}t' \tag{B.7}$$

where $IntLoss_{inv}(t)$ is the inverse ratio version of integrated muon loss function form, which is constructed from the $IntLoss(t)$.

Appendix C

The Statistical Error in the Inverse Ratio Fit

This section discusses the statistical uncertainty of the lifetime in the *Inverse Ratio* fit.

Let us assume the electron events follow exactly the *Inverse Ratio* distribution,

$$n_i(t) = N_\circ \cdot e^{-\frac{t_i}{\tau_\circ}} \cdot [1 + 2.87 \times 10^{-4} A \cos(\omega_a t_i + \phi_a)] \tag{C.1}$$

where t_i is the center of i^{th} bin on the electron time histogram, $t_i = (i - \frac{1}{2})t_{bw}$, t_{bw} is the time bin width of the histogram. A fit will return the optimal values of each parameter: $N_\circ$ and $\tau_\circ$.

Let us first derive the uncertainty in the simplest case by assuming that the histogram starts at $T = 0$, and ignoring the correlation between τ and N. The small term in the function is also ignored at this moment.

When the fitted lifetime differs from the expected value $\tau_\circ$ by one sigma: $\tau_\circ \to \tau_\circ + \delta\tau$. The difference between the function with $\tau_\circ + \delta\tau$ and the histogram is

$$\Delta_{\tau i} = N_\circ \, e^{-\frac{t_i}{\tau_\circ + \delta\tau}} - N_\circ \, e^{-\frac{t_i}{\tau_\circ}} = N_\circ \, \frac{\delta\tau \; t_i}{\tau_\circ^2} e^{-\frac{t_i}{\tau_\circ}} \tag{C.2}$$

The chi-square function $\chi^2(\tau)$ is:

$$\begin{aligned}\chi^2(\delta\tau) &= \sum_i \frac{\Delta_{\tau i}^2}{\sigma_i^2} = \sum_i \frac{\Delta_{\tau i}^2}{n_i} = \sum_i \frac{[N_\circ \frac{\delta\tau\, t_i}{\tau_\circ^2} e^{-\frac{t_i}{\tau_\circ}}]^2}{N_\circ\, e^{-\frac{t_i}{\tau_\circ}}} \\ &= \sum_i N_\circ \frac{(\delta\tau)^2}{\tau_\circ^4} t_i^2\, e^{-\frac{t_i}{\tau_\circ}} = \frac{1}{t_{bw}} \int_0^\infty N_\circ \frac{(\delta\tau)^2}{\tau_\circ^4} t^2\, e^{-\frac{t}{\tau_\circ}}\, \mathrm{d}t \\ &= \frac{1}{t_{bw}} N_\circ \frac{(\delta\tau)^2}{\tau_\circ^4} [2\tau_\circ^3] = \frac{2}{t_{bw}} N_\circ \tau_\circ \frac{(\delta\tau)^2}{\tau_\circ^2} \end{aligned} \tag{C.3}$$

where the distribution of $n_i(t)$ is Poisson with variance $\sigma_i^2 = n_i(t)$. The sum $\sum_i$ is replaced by the integral $\frac{1}{t_{bw}} \int_0^\infty \mathrm{d}t$. Recall that total muon number N_{total} equals to the sum of all decay electrons,

$$N_{total} = \sum_i n_i = \frac{1}{t_{bw}} \int_0^\infty N_\circ e^{-\frac{t}{\tau_\circ}}\, \mathrm{d}t = \frac{N_\circ \tau_\circ}{t_{bw}} \tag{C.4}$$

The fitting uncertainty is found at $\chi^2(\tau) = 1$. To get the error of τ, we substitute N_{total} into the last step in Eq. C.3, and set the equation to be 1,

$$1 = 2 N_{total} \frac{(\sigma_\tau)^2}{\tau_\circ^2} \tag{C.5}$$

This gives the statistical uncertainty for the lifetime

$$\sigma_\tau = \frac{\tau_\circ}{\sqrt{2\ N_{total}}} \tag{C.6}$$

Since we have ignored the correlation between the τ and N, the calculated statistical error on the lifetime is smaller by a factor of $\sqrt{2}$ than it should be. Next, we will consider the correlation, and also let the start time to be arbitrary time T other than $T = 0$.

The parameter τ and N are correlated. Therefore in the chi-square function $\chi^2(\delta\tau, \delta N)$, we need to include both parameters.

$$\Delta(\delta\tau, \delta N) = \delta\tau\ N_\circ\ \frac{t_i}{\tau_\circ^2} e^{-\frac{t_i}{\tau_\circ}} + \delta N e^{-\frac{t_i}{\tau_\circ}} \tag{C.7}$$

On the histogram, the $T = 0$ time is set to be the time of the injection. But the fitting start time does not necessary be at $T = 0$. In most of cases, the start time T has to be late because of the physical limitation. The total muon number used to do the fit is N_{total},

$$N_{total} = \sum_i n_i = \frac{1}{t_{bw}} \int_T^\infty N_\circ e^{-\frac{t}{\tau_\circ}}\, \mathrm{d}t = \frac{N_\circ \tau_\circ}{t_{bw}}\, e^{-\frac{T}{\tau_\circ}} \tag{C.8}$$

The chi-square function is,

$$\begin{aligned}
\chi^2(\delta\tau,\delta N) &= \sum_i \frac{\Delta^2(\delta\tau,\delta N)}{\sigma_i^2} = \sum_i \frac{\Delta_{\tau i}^2}{n_i} = \sum_i \frac{[\delta\tau\ N_\circ\ \frac{t_i}{\tau_\circ^2} e^{-\frac{t_i}{\tau_\circ}} + \delta N e^{-\frac{t_i}{\tau_\circ}}]^2}{N_\circ\ e^{-\frac{t_i}{\tau_\circ}}} \\
&= (\delta\tau)^2 \frac{N_\circ}{\tau_\circ^4} \sum_i t_i^2\ e^{-\frac{t_i}{\tau_\circ}} + (\delta\tau\delta N)\frac{2}{\tau_\circ^2}\sum_i t_i\ e^{-\frac{t_i}{\tau_\circ}} + (\delta N)^2 \frac{1}{N_\circ}\ \sum_i e^{-\frac{t_i}{\tau_\circ}} \\
&= (\delta\tau)^2 \frac{N_\circ}{\tau_\circ^4}\frac{1}{t_{bw}} \int_T^\infty t^2\ e^{-\frac{t}{\tau_\circ}}\mathrm{d}t + (\delta\tau\delta N)\frac{2}{\tau_\circ^2}\frac{1}{t_{bw}}\int_T^\infty t\ e^{-\frac{t}{\tau_\circ}}\mathrm{d}t + \\
&\quad (\delta N)^2 \frac{1}{N_\circ}\ \frac{1}{t_{bw}} \int_T^\infty e^{-\frac{t}{\tau_\circ}}\mathrm{d}t \\
&= (\delta\tau)^2 \frac{N_\circ}{\tau_\circ^4}\frac{1}{t_{bw}}\tau_\circ(T^2 + 2T\tau_\circ + 2\tau_\circ^2)\ e^{-\frac{T}{\tau_\circ}} + \\
&\quad (\delta\tau\delta N)\frac{2}{\tau_\circ^2}\frac{1}{t_{bw}}\tau_\circ(T+\tau_\circ)\ e^{-\frac{T}{\tau_\circ}} + \\
&\quad (\delta N)^2 \frac{1}{N_\circ}\ \frac{1}{t_{bw}}\tau_\circ e^{-\frac{T}{\tau_\circ}} \\
&= (\delta\tau)^2 \frac{N_{total}}{\tau_\circ^4}(T^2 + 2T\tau_\circ + 2\tau_\circ^2) + \\
&\quad (\delta\tau\delta N)\frac{2N_{total}}{N_\circ\tau_\circ^2}(T+\tau_\circ) + \\
&\quad (\delta N)^2 \frac{N_{total}}{N_\circ^2}
\end{aligned} \tag{C.9}$$

As being derived in reference [79], the solution to the Eq. C.9 when $\chi^2 = 1$ at its extreme point will give

$$\begin{aligned}
\sigma_\tau^{-2} &= \frac{1}{2}\frac{\partial^2\chi^2}{\partial\tau^2} - \Big[\frac{\partial^2\chi^2}{\partial\tau\ \partial N}\Big]^2\Big[4\frac{1}{2}\frac{\partial^2\chi^2}{\partial N^2}\Big]^{-1} \\
&= \frac{N_{total}}{\tau_\circ^4}(T^2 + 2T\tau_\circ + 2\tau_\circ^2) - \Big[\frac{2N_{total}}{N_\circ\tau_\circ^2}(T+\tau_\circ)\Big]^2\Big[4\frac{N_{total}}{N_\circ^2}\Big]^{-1} \\
&= \frac{N_{total}}{\tau_\circ^2}
\end{aligned} \tag{C.10}$$

the statistical uncertainty for the lifetime σ_τ at any start time T is

$$\sigma_\tau = \frac{\tau_\circ}{\sqrt{N_{total}}} \tag{C.11}$$

it is independent to the fit start time explicitly. But the total muon number depends on the start time.

$$\sigma_N^{-2} = \frac{1}{2}\frac{\partial^2\chi^2}{\partial N^2} - \Big[\frac{\partial^2\chi^2}{\partial\tau\ \partial N}\Big]^2\Big[4\frac{1}{2}\frac{\partial^2\chi^2}{\partial\tau^2}\Big]^{-1}$$

$$= \frac{N_{total}}{N_\circ^2} - \Big[\frac{2N_{total}}{N_\circ \tau_\circ^2}(T+\tau_\circ)\Big]^2 \Big[4\frac{N_{total}}{\tau_\circ^4}(T^2+2T\tau_\circ+2\tau_\circ^2)\Big]^{-1}$$

$$= \frac{N_{total}}{N_\circ^2}\frac{1}{T^2/\tau_\circ^2+2T/\tau_\circ+2} \tag{C.12}$$

that is

$$\sigma_N = \frac{N_\circ}{\sqrt{N_{total}}}\sqrt{T^2/\tau_\circ^2+2T/\tau_\circ+2} \tag{C.13}$$

while σ_N depends on the choice of the fitting start time explicitly.

Appendix D

Fit Start Time Scanning

The start time scan plots with muon loss in the fit are shown for the 2000 and 2001 data. All parameters are free in the fitting except for muon loss A_{loss} in data set P4 in the 2000 run. The up and down triangle dots on the plots form the allowed one sigma error band for the correlated data used in the fitting.

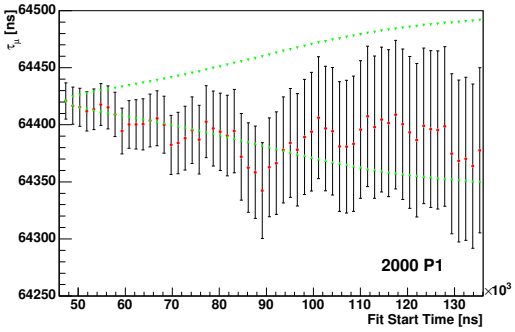

(a) τ_μ

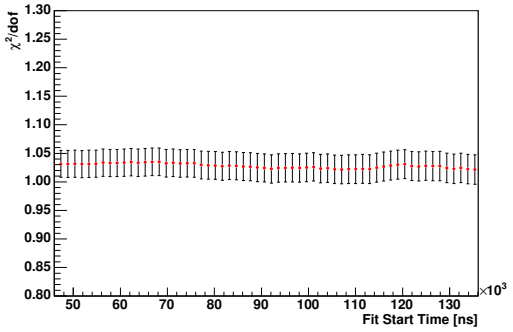

(b) Reduced χ^2

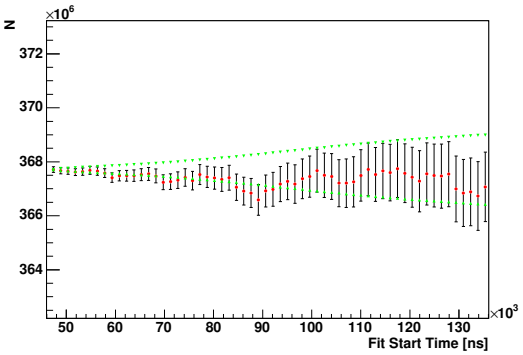

(c) N

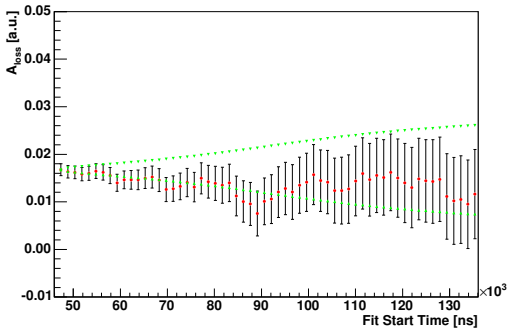

(d) Muon Loss Norm

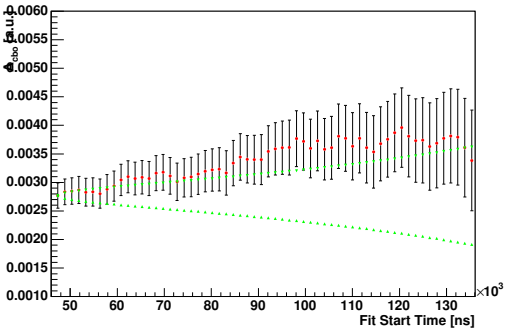

(e) CBO Amplitude

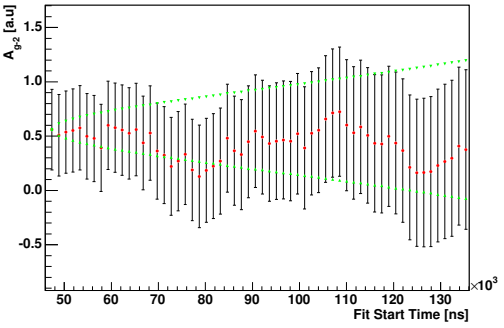

(f) g-2 Asymmetry

Figure D.1: Start time scans of important parameters used in the dilated lifetime fit P1 data set in 2000 run.

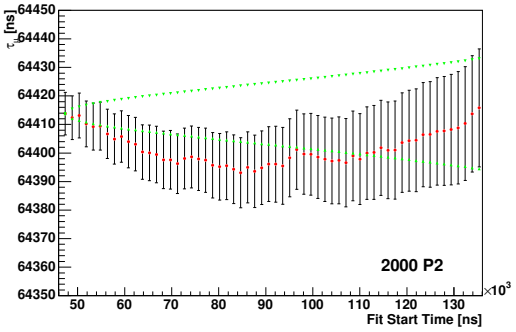

(a) τ_μ

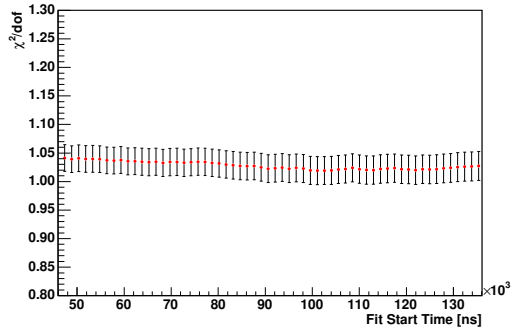

(b) Reduced χ^2

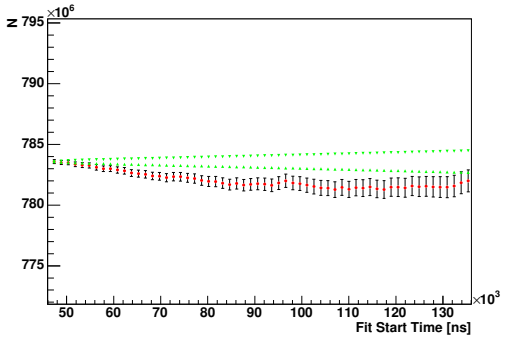

(c) N

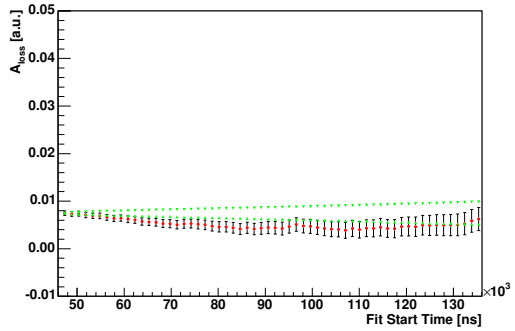

(d) Muon Loss Norm

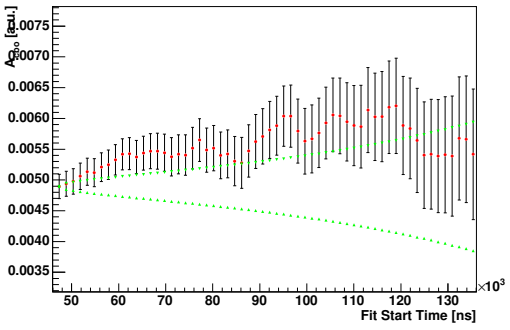

(e) CBO Amplitude

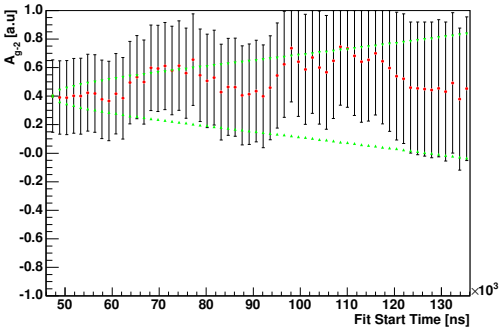

(f) g-2 Asymmetry

Figure D.2: Start time scans of important parameters used in the dilated lifetime fit P2 data set in 2000 run.

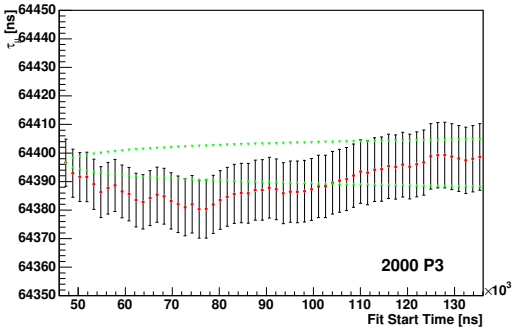

(a) τ_μ

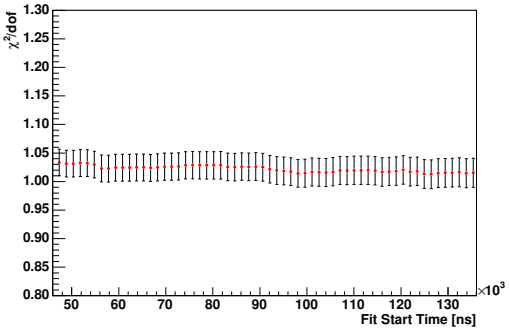

(b) Reduced χ^2

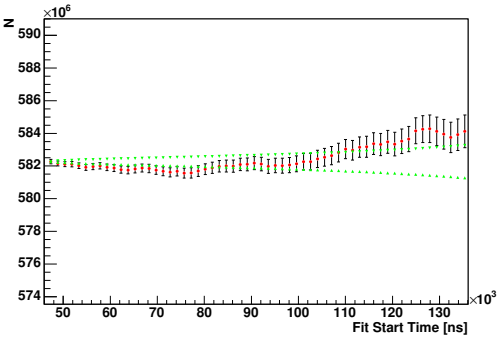

(c) N

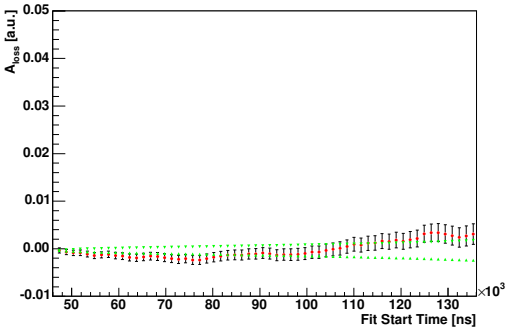

(d) Muon Loss Norm

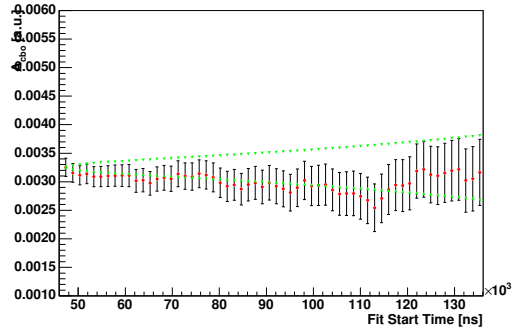

(e) CBO Amplitude

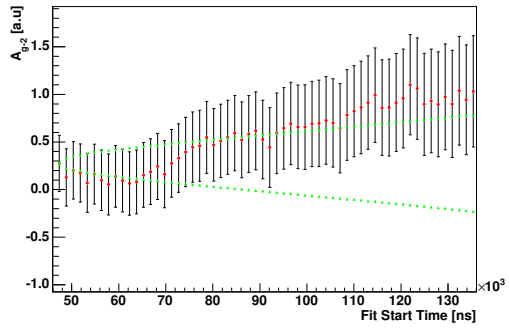

(f) g-2 Asymmetry

Figure D.3: Start time scans of important parameters used in the dilated lifetime fit P3 data set in 2000 run.

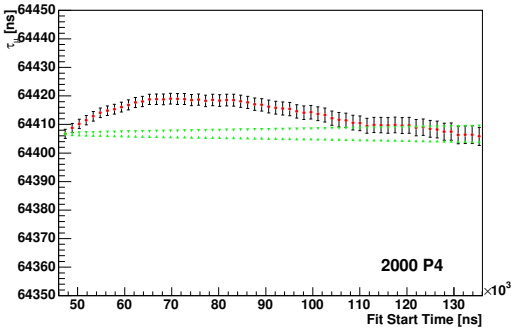

(a) τ_μ

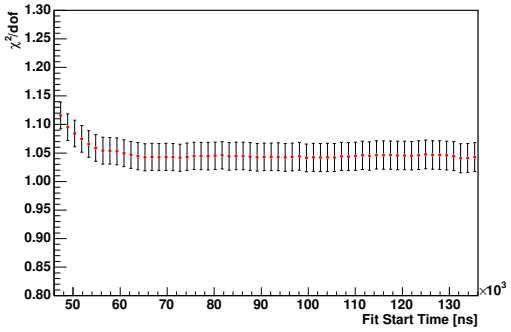

(b) Reduced χ^2

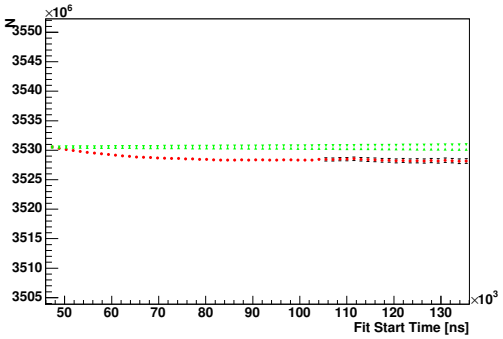

(c) N

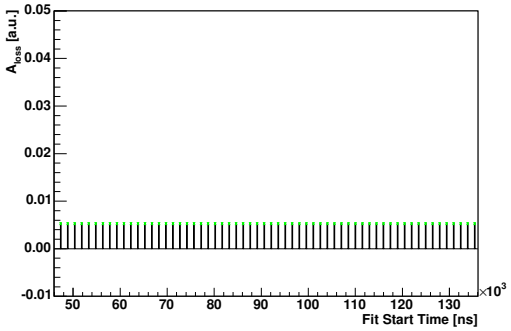

(d) Muon Loss Norm

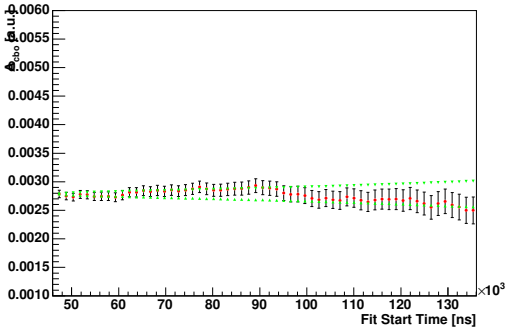

(e) CBO Amplitude

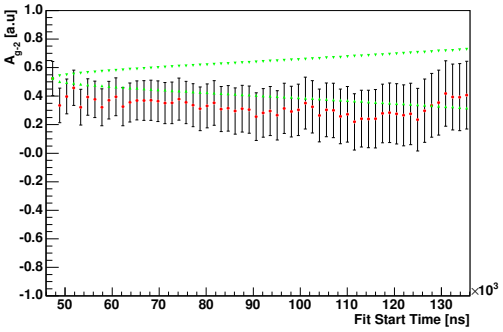

(f) g-2 Asymmetry

Figure D.4: Start time scans of important parameters used in the dilated lifetime fit P4 data set in 2000 run.

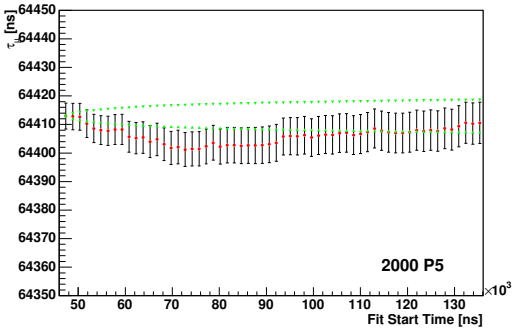

(a) τ_μ

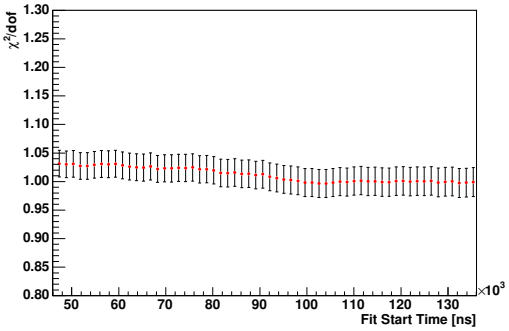

(b) Reduced χ^2

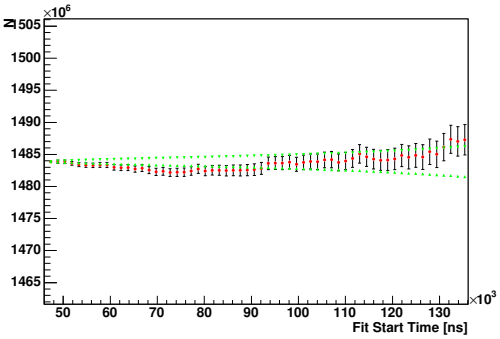

(c) N

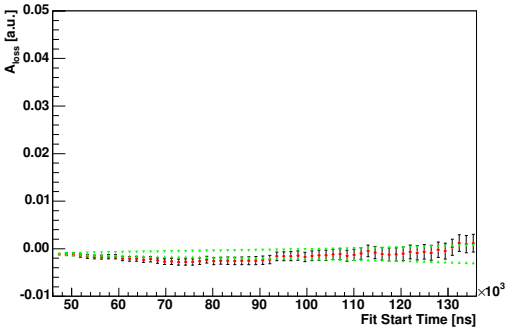

(d) Muon Loss Norm

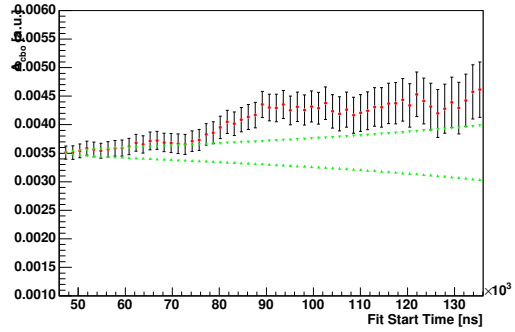

(e) CBO Amplitude

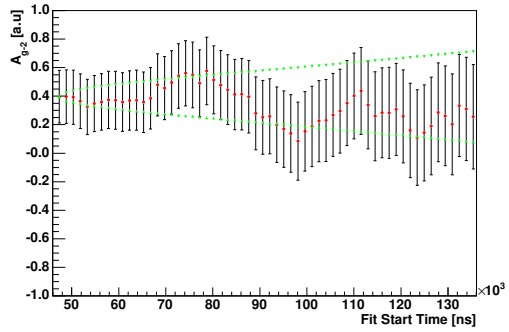

(f) g-2 Asymmetry

Figure D.5: Start time scans of important parameters used in the dilated lifetime fit P5 data set in 2000 run.

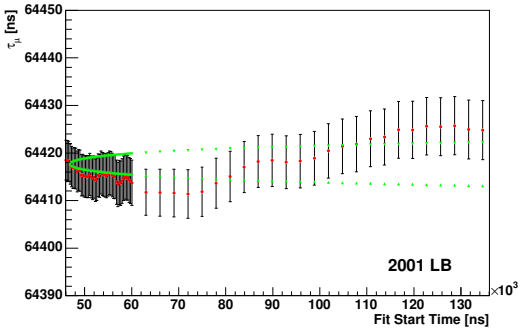

(a) τ_μ

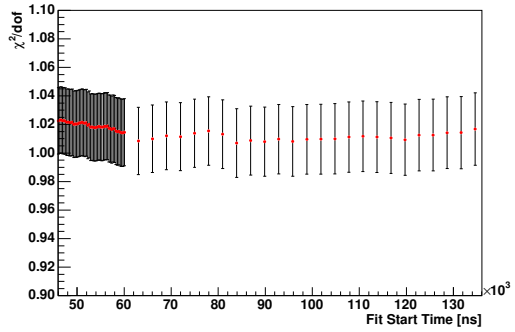

(b) Reduced χ^2

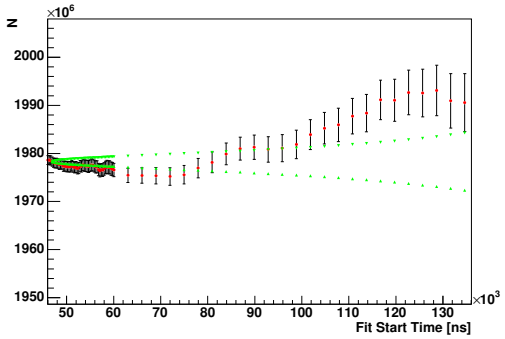

(c) N

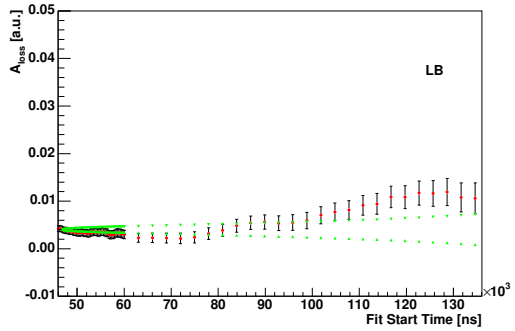

(d) Muon Loss Norm

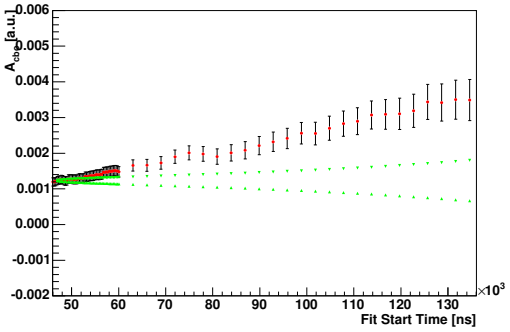

(e) CBO Amplitude

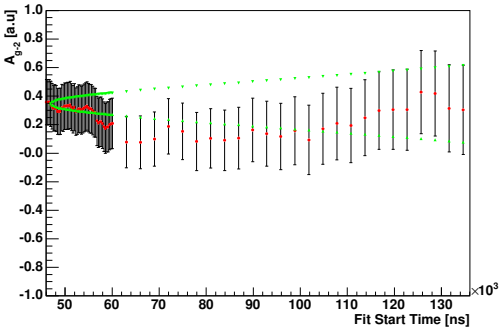

(f) g-2 Asymmetry

Figure D.6: Start time scans of important parameters used in the dilated lifetime fit LB data set in 2001 run.

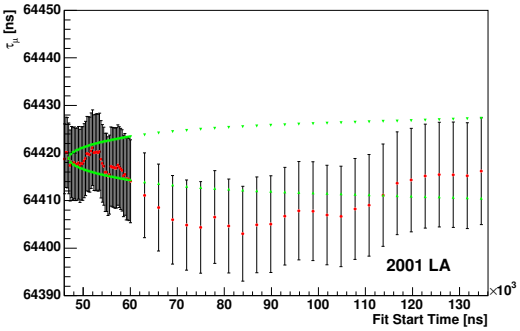

(a) τ_μ

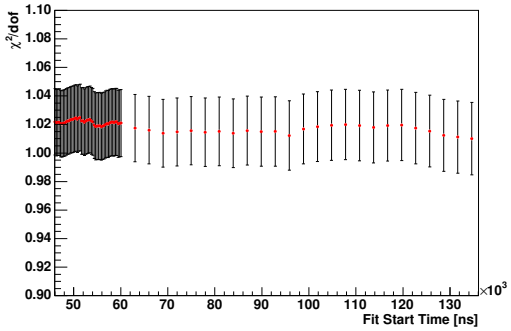

(b) Reduced χ^2

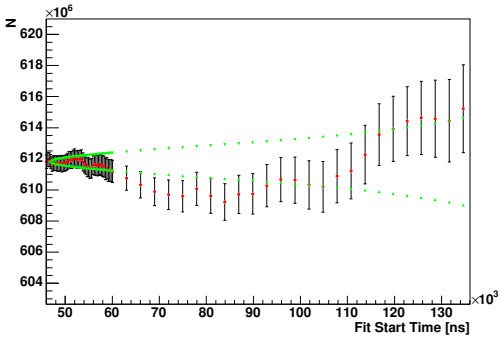

(c) N

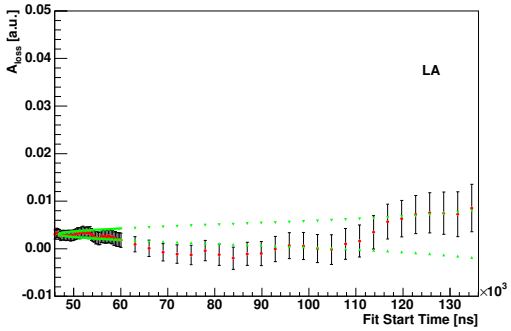

(d) Muon Loss Norm

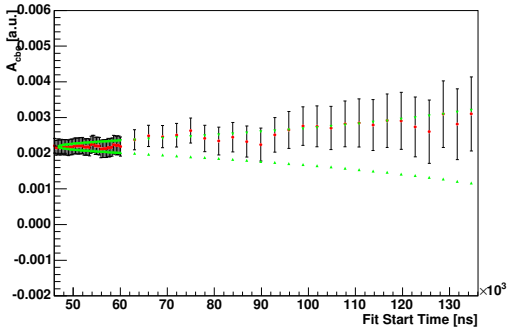

(e) CBO Amplitude

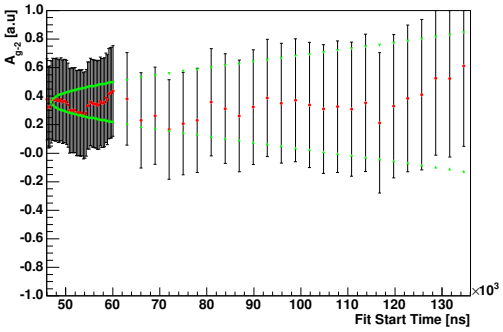

(f) g-2 Asymmetry

Figure D.7: Start time scans of important parameters used in the dilated lifetime fit LA data set in 2001 run.

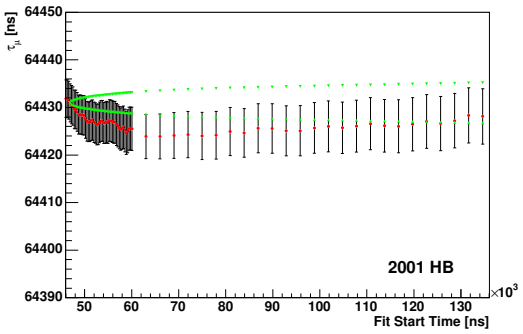

(a) τ_μ

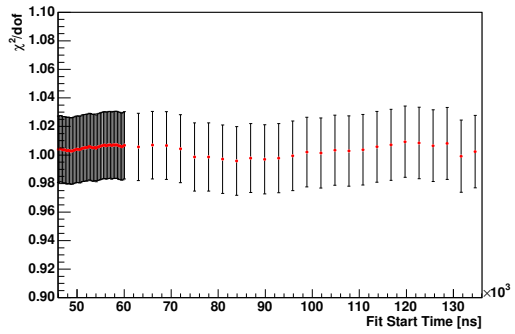

(b) Reduced χ^2

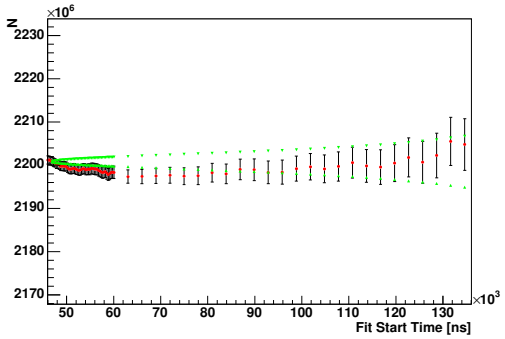

(c) N

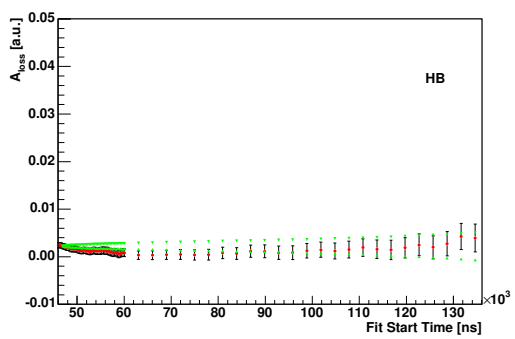

(d) Muon Loss Norm

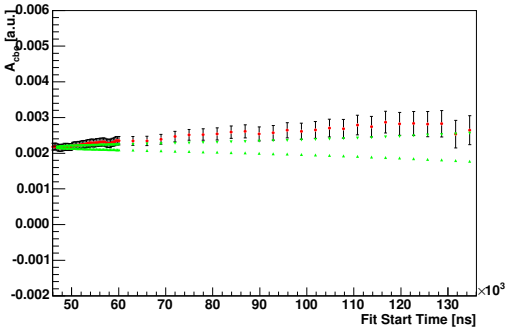

(e) CBO Amplitude

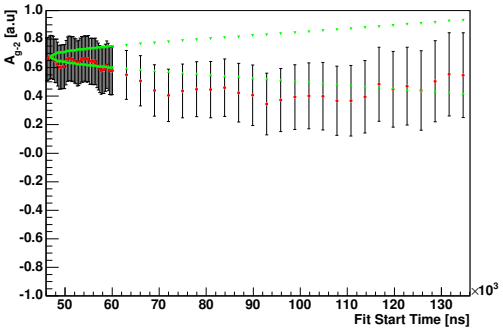

(f) g-2 Asymmetry

Figure D.8: Start time scans of important parameters used in the dilated lifetime fit HB data set in 2001 run.

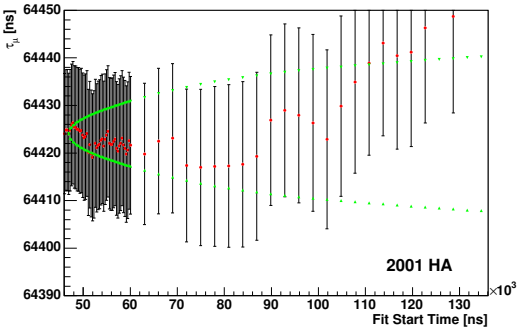

(a) τ_μ

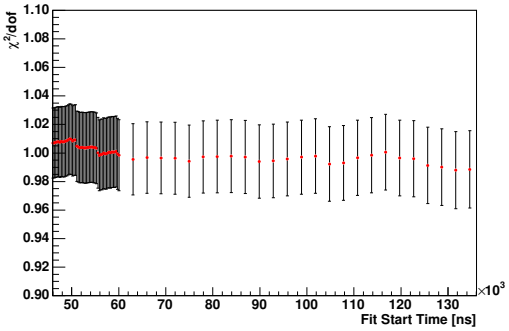

(b) Reduced χ^2

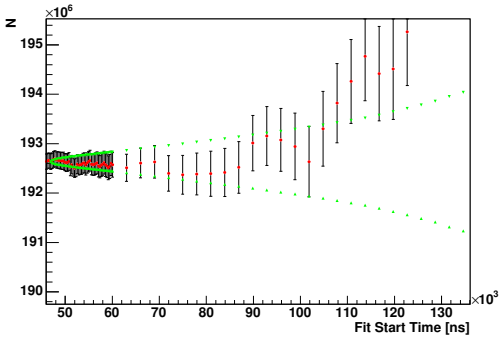

(c) N

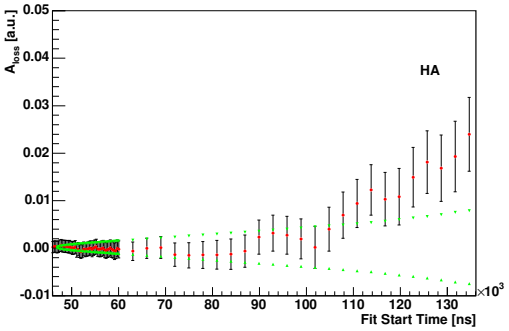

(d) Muon Loss Norm

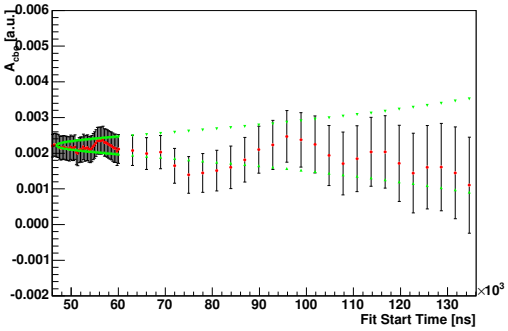

(e) CBO Amplitude

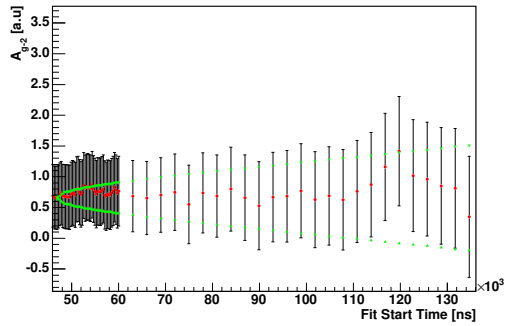

(f) g-2 Asymmetry

Figure D.9: Start time scans of important parameters used in the dilated lifetime fit HA data set in 2001 run.

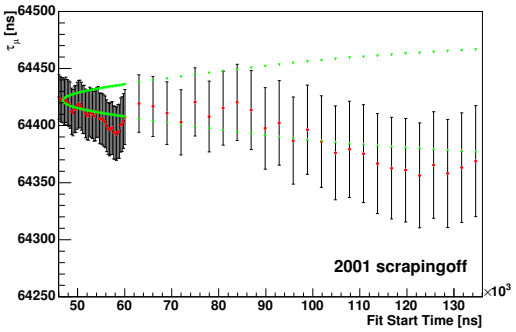

(a) τ_μ

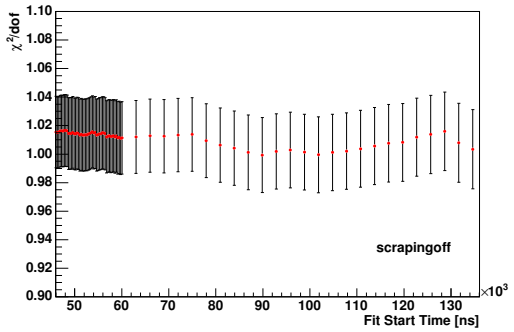

(b) Reduced χ^2

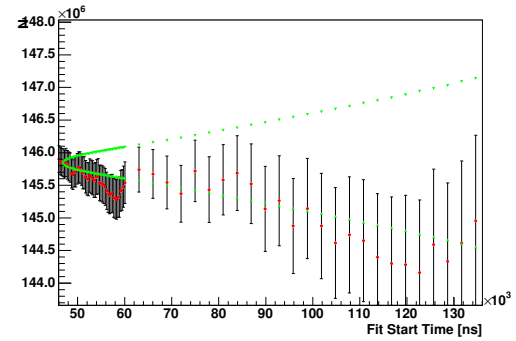

(c) N

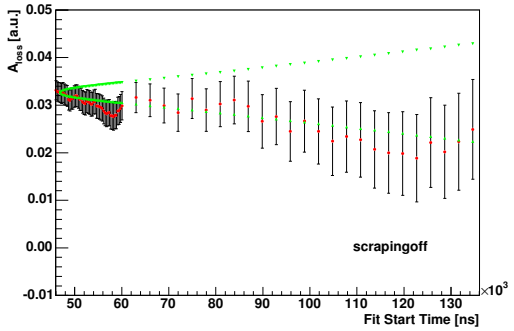

(d) Muon Loss Norm

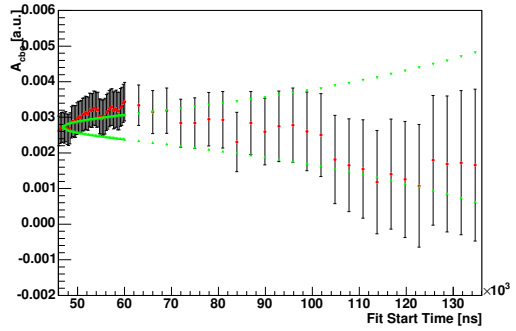

(e) CBO Amplitude

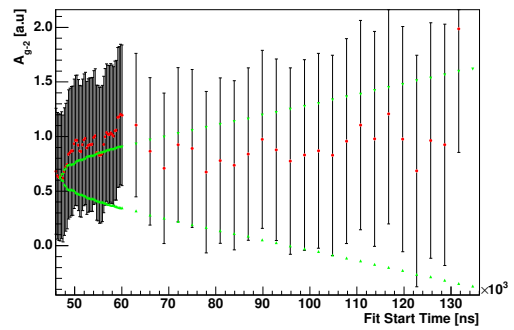

(f) g-2 Asymmetry

Figure D.10: Start time scans of important parameters used in the dilated lifetime fit Scraping off data set in 2001 run.

References

[1] P.J. Mohr and B.N. Taylor, Rev. Mod. Phys. **77**, 1-107 (2005)

[2] S.H. Neddermeyer and C.D. Anderson, Phys. Rev. **51**, 884 (1937).

[3] S. Eidelman *et. al.*, Phys. Lett. **B 592**, 1 (2004).

[4] LEPEWG, SLD Electroweak and Heavy Flavour Groups, [hep-ex/0509008] (2005)

[5] T. Van Ritbergen and R.G. Stuart, Phys. Rev. Lett. **82**, 488 (1999).

[6] W.J. Marciano, "Fermi Constants and new Physics", [hep-ph/9903451] (1999).

[7] G. Bardin *et. al.*, Phys. Lett. **79B**, 52 (1978).

[8] G. Bardin *et. al.*, Phys. Lett. **137B**, 135 (1984).

[9] K.L. Giovanetti *et. al.*, Phys. Rev. D **29**, 343 (1984).

[10] P. Kammel, "Muon Capture and Muon Lifetime", [nucl-ex/0304019] (2003)

[11] E.J. Bleser *et. al.*, Phys. Rev. Lett. **8** 288 (1962).

[12] J. E. Rothberg *et. al.*, Phys. Rev. **132** 2664, (1963).

[13] A. Alberigi Quaranta *et. al.*, Phys. Rev. **117** 2118 (1969).

[14] G. Bardin *et. al.*, Nucl. Phys. **A352**, 365 (1981).

[15] G. Charpak *et. al.*, Nuovo Cimento Soc. Ital. Fis. **37**, 1241 (1965).

[16] J. Bailey *et. al.*, Nuovo Cimento Soc. Ital. Fis. **A9**, 369 (1972).

[17] J. Bailey *et. al.*, CERN Muon Storage Ring Collaboration, Phys. Lett. **B67**, 225 (1977).

[18] J. Bailey *et. al.*, Nature, Vol.**268**, 301 (1977).

[19] R. M. Carey *et. al.*, Phys. Rev. Lett. **82**, 1632 (1999).

[20] H. N. Brown *et. al.*, Muon (g-2) Collaboration, Phys. Rev. **D62**, 091101 (2000)

[21] H. N. Brown *et. al.*, Muon (g-2) Collaboration, Phys. Rev. Lett. **86**, 2227 (2001)

[22] G.W. Bennett *et. al.*, Muon (g-2) Collaboration, "Measurement of the Positive Muon Anomalous Magnetic Moment to 0.7 ppm", Phys. Rev. Lett. **89**, 101804 (2002)

[23] G.W. Bennett *et. al.*, Muon (g-2) Collaboration, "Measurement of the Negative Muon Anomalous Magnetic Moment to 0.7 ppm", Phys. Rev. Lett. **92**, 161802 (2004)

[24] D. Newman *et. al.*, Phys. Rev. Lett. **40**, 1355 (1978).

[25] F. Combley *et. al.*, Phys. Rev. Lett. Vol. **42**, 1383 (1979).

[26] G. Saathoff *et. al.*, Phys. Rev. Lett. Vol. **91**, 190403-1, (2003)

[27] J.F. Donoghue *et. al.*, "Dynamics of the Standard Model", Cambridge University Press (1992)

[28] D. Bardin and G. Passarino, "The Standard Model in the Making", Oxford University Press (1999)

[29] S.M. Berman, Phys. Rev. **112**, 267 (1958).

[30] T. Kinoshita and A. Sirlin, Phys. Rev.**113**, 1652 (1959).

[31] T. Van Ritbergen and R.G. Stuart, [hep-ph/9904240] (1999).

[32] T. Van Ritbergen and R.G. Stuart, Phys. Lett. **B437**, 201 (1998).

[33] W. J. Marciano and A. Sirlin, Phys. Rev. Lett. **61**, 1815 (1988).

[34] W. Bertl *et. al.*, Nucl. Phys. B **260**, 1 (1985).

[35] J. Miller, (g-2) Technical Note 69, (1991).

[36] E821 Collaboration, *BNL AGS E821 Design Report*, 3rd ed., (1995).

[37] A. Trofimov, Ph.D. dissertation, Boston University, (2002).

[38] W.M. Morse, (g-2) Technical Note 317, (1998).

[39] A. Yamamoto *et. al.*, Nucl Instrum. Meth. **A491**, 23 (2002).

[40] F. Krienen, D. Loomba and W. Meng, Nucl. Instr. and Meth. **A283**, 5 (1989).

[41] G.T. Danby *et. al.*, Nucl. Instr. and Meth. **A457**, 151 (2001).

[42] S.I. Redin, Ph.D. dissertation, Yale University (1999).

[43] A.P. Grossman, Ph.D. dissertation, Heidelberg University (1998).

[44] W. Morse, Muon (g-2) Technical Note 316, (1998); W. Morse, Muon (g-2) Technical Note 332, (1998).

[45] E. Efstathiadis *et. al.*, Nucl. Instr. and Meth. **A496**, 8 (2003).

[46] Y. K. Semertzidis *et. al.*, Nucl. Instr. and Meth. **A503**, 458 (2003).

[47] E. Benedict *et. al.*,"Beam Dynamics in the Muon (g-2) Ring". Nucl. Instr. and Meth. summitted for publishing (2004).

[48] M. Sossong *et. al.*, "Traceback Wire Chamber System for the Muon (g-2) Experiment", sumitted to Nucl. Instr. and Meth. (2005).

[49] M. Sossong, Ph.D. dissertation, University of Illinois at Urbana-Champaign, (2005).

[50] S. A. Sedykh *et. al.*, Nucl. Instr. and Meth. **A455**, 346 (2000).

[51] L. Duong, Ph.D. dissertation, University of Minnesota, (2001).

[52] R. McNabb, Ph. D Dissertation, University of Minnesota, (2004).

[53] P. Cushman *et. al.*, Nucl. Instr. and Meth. **A378**, 116 (1996).

[54] P. Cushman *et. al.*, Nucl. Instr. and Meth. **A418**, 300 (1998).

[55] S. Giron *et. al.*, Ph. D. Dissertation, University of Minnesota, (2004).

[56] W.D. Peterson, *The VMEbus Handbook*, 4th ed. (VMEbus International Trade Association, 1997).

[57] W. Earle, E. Hazen, B. Safford and G. Varner, (g-2) Technical Note 207, (1994).

[58] See for example the short introduction in *Lecroy Research Instrumentation Catalog.*

[59] I. Kronkvist, P. Cushman, L. Duong and C. Timmermans, prepared for Computing in High-energy Physics (CHEP98), Chicago, IL, August 31-Sept. 4, 1998; R. Ball, Y. Takeuchi, M. Nomachi and C. Timmermans, UNIDAQ version 2.3, (1995).

[60] M. Nomachi *et. al.*, prepared for Computing in High-energy Physics (CHEP94), San Francisco, CA, Apr. 21-27, (1994).

[61] R. Prigl *et. al.*, Nucl. Instr. and Meth. A **374**, 118 (1996).

[62] X. Fei *et. al.*, Nucl. Instr. and Meth. A **394**, 349 (1997).

[63] H. Deng, Ph.D. dissertation, Yale University (2002).

[64] C. P. Slichter, "Principles of Magnetic Resonance, 2^{nd} ed.", Springer-Verlag, Berlin, 1978

[65] J. H. Simpson and H. Y. Carr, Phys. Rev. **111**, 1201 (1958)

[66] F. Gray, "Pulse Fitting in G2Too", (g-2) Technical Note 417, (2002).

[67] I. Logashenko,(g-2) Technical Note 369, (2000); I. Logashenko, (g-2) Technical Note 378, (2000).

[68] R. Brun and F. Rademakers, Nucl. Instr. and Meth **A389**, 81 (1997).

[69] CERN Program Library, Physics Analysis Workstation (PAW), library entry Q121 (1994).

[70] C. Polly, Ph.D. dissertation, University of Illinois at Urbana-Champaign, (2005).

[71] F. Gray, Ph.D. dissertation, University of Illinois at Urbana-Champaign, (2003).

[72] C.S. Ozben and Y.K. Semertzidis, (g-2) Technical Note 397, (2001).

[73] Y. Orlov, *et. al.*, Nucl. Instr. and Meth. **A482**, 767 (2002)

[74] J. Bailey, *et. al.*, Nucl. Phys. **B150**, 1 (1979)

[75] R. Carey, M. Hare, "CERN III style Fast Rotation Analysis", g-2 Technical Note 357, (2000)

[76] W. Liu, *et. al.*, Phys. Rev. Lett.**82**, 711 (1999)

[77] F. James and M. Roos, Comput. Phys. Commun. **10**, 343 (1975).

[78] R. Carey, D. Hertzog, *et. al.*, Mulan Proposal, (1999)

[79] S. Redin, *et. al.*, "Statistical Errors of 5 Parameter Fit", submitted to Nucl. Instr. and Meth. **A, (2005)**